Journal of Materials Chemistry A

REVIEW

View Article Online
View Journal | View Issue

Cite this: J. Mater. Chem. A, 2019, 7, 11613

Electrospun nanostructures for conversion type cathode (S, Se) based lithium and sodium batteries

Arvinder Singh and Vibha Kalra *

Sulfur and selenium based rechargeable batteries have attracted great attention due to their high gravimetric/volumetric energy densities owing to multielectron conversion reactions. Over the last few years, rationally designed nanomaterials have played a crucial role in the continuous growth of these battery systems. In this context, electrospun nanostructures are of paramount interest for the development of these rechargeable secondary batteries due to their high surface area to volume ratio and good mechanical stability. Here, a systematic and comprehensive review of the recent advances in the development of electrospun nanostructures as novel materials for next generation sulfur and selenium based lithium and sodium batteries is presented. In this review, we highlight the recent progress made in Li–S, RT Na–S, Li–S_xSe_y, RT Na–S_xSe_y, Li–Se and RT Na–Se batteries using electrospun carbon, polymers or heterostructures with tailored textural properties, compositions and surface functionalities (polysulfide trapping capability and catalytic activity) in cathodes, interlayers, separator coatings, and electrolyte membranes. The emphasis is placed on various synthesis strategies to design advanced electrospun nanostructures with tunable structural properties and the impact of these features on capacity, rate capability and long-term cycling. Moreover, we have introduced the 'fraction of (electrochemically) active cathode (FAC)' as a parameter to highlight the advantages of free-standing

Received 10th January 2019
Accepted 28th March 2019

DOI: 10.1039/c9ta00327d

rsc.li/materials-a

Chemical and Biological Engineering, Drexel University, Philadelphia, PA-19104, USA. E-mail: vk99@drexel.edu

Dr Arvinder Singh received his Ph.D. from the Department of Physics at the Indian Institute of Technology (IIT) Kharagpur, India in 2016. Currently, he is a postdoctoral researcher in the Chemical and Biological Engineering Department, Drexel University, USA. His research interests focus on the development and characterization of advanced nanostructures and their applications in supercapacitors, and various intercalation and conversion type rechargeable secondary batteries. He has published 14 articles in peer-reviewed journals and received 2 young scientist awards for his work on energy storage devices.

Dr Vibha Kalra is an associate professor in the Department of Chemical and Biological Engineering at Drexel University. Kalra received her BS from the Indian Institute of Technology (IIT), Delhi, India in 2004 and PhD from Cornell University in 2009, both in Chemical Engineering. Prior to joining Drexel in the Fall of 2010, Kalra worked in the electronic packaging research division at Intel Corporation. Her research group at Drexel combines material assembly & characterization, study of fundamental electrochemical behavior, in situ spectroelectrochemistry, and device assembly & testing to develop nanofiber-based energy storage devices including batteries and supercapacitors. She has published over 40 peer-reviewed journal articles and has six pending patents in the field of nanofibers for energy storage. Kalra is a recipient of several awards including the NSF CAREER award (2012), ONR summer faculty fellowship award (2013), AICHE DVS Outstanding Faculty of the Year Award (2015) and Outstanding Research Award, COE, Drexel University (2015).

electrospun nanostructures compared to their non-electrospun or slurry-cast electrospun counterparts. Furthermore, current challenges and prospects in the use of electrospun nanostructures in each battery system are also discussed. We believe that this review will provide new opportunities in the field of advanced sulfur and selenium based rechargeable batteries using electrospun nanostructures.

1. Introduction

With rapidly depleting fossil fuel reservoirs (crude oil, coal, and natural gases), increasing environmental pollution, and human civilization, there is an urgent call for cheaper and environmentally benign renewable energy sources.[1] The primary key to decreasing the dependence on fossil fuels is harvesting and converting clean energy from sources such as solar, geothermal, wind, and mechanical vibration.[2] At the same time, it is crucial to develop highly efficient energy storage systems owing to the intermittent nature of renewable sources and ever-increasing dependency of our modern life on advanced technologies.[3–5] Several energy storage technologies are potentially available, which either store electricity directly in an electrical field (potential difference; electric charges) or in another form of energy such as chemical, kinetic, or potential energy.[1,6,7] Conventional dielectric capacitors and supercapacitors are examples of the former case mainly used for power management (*e.g.*, frequency regulation) due to their high coulombic efficiency (~100%) and rapid charge–discharge capability.[8,9] Typical examples of the latter case involve flywheels (FWs; kinetic energy), compressed air energy storage (CAES; potential energy) or pumped hydro (PHS; potential energy) and electrochemical energy storage or batteries (chemical energy). Like other direct energy storage technologies, FWs are also useful for power management due to their low energy density.[10] PHS can be a potential candidate for bulk energy storage, but it is a site-dependent technology, which involves an extended construction period (7–8 years), reaction time (10 minutes), and massive initial investment.[11] Similarly, CAES demands suitable geographic locations with salt domes, caverns, depleted aquifers or rock formation for air storage.[12] In contrast, electrochemical energy storage technologies or batteries can chemically store electricity and release it on demand.[13] Advances in rechargeable secondary batteries based on alkali lithium metal anodes came about later in the 1960s.[14,15] Over the last two decades, rechargeable Li-ion batteries (LIBs), with an energy density between 150 and 240 W h kg^{-1} and no memory effect, have established themselves globally in a wide range of electronic and communication devices.[16,17] Currently, these rechargeable batteries are among the most prominent electrochemical energy storage technologies due to their long cycle life (~5000 cycles) and efficiency (>90%).[14,18] However, for their use in stationary grids and hybrid/electric vehicles (EVs), we need sizeable LIB packs due to their limited state-of-the-art energy density.[19] Fig. 1(a and b) presents the battery pack size, vehicle range and cell chemistry of various available LIB packs in the market for hybrid and electric plug-in vehicles, respectively. It is evident that only the Tesla Model S can cope with the energy demand for the vehicle range (~500 km) targeted by automobile industries in a single charge/discharge. However, in this scenario, the size and cost of the large-sized LIB packs (*e.g.*, 85 kW h battery pack, 7104 cells, 1200 lb/540 kg, ~$150 per kW h – Tesla Model S) impose the most crucial and insurmountable challenge. The limited energy density of LIBs is mainly due to intercalation type transition metal based heavy compound electrode materials (*e.g.*, $LiCoO_2$).[20,21] Several other alternatives to $LiCoO_2$ such as $LiFePO_4$ and $LiNi_{1-y-z}Mn_yCo_zO_2$ have also penetrated the market with enhanced performance.[20,21] Nonetheless, all these materials exhibit intrinsically limited capacity (<200–300 mA h g^{-1}) due to the number of electron transfer involved in the intercalation chemistry and crystal structure aspects during accommodation of Li^+ cations.[20–22] The energy density values of LIBs based on these intercalation type materials are gradually reaching the theoretical limits and can be increased further at most by 30% of current values with future technical optimization.[20] Therefore, LIBs may not ever reach the targeted device level of 500 W h kg^{-1} energy density and size–cost aspects for applications in hybrid/electric vehicles.[20,23] Thus, there is a worldwide consensus that a revolution in rechargeable secondary batteries is needed by employing lightweight materials with multi-electron chemistry in order to use them in hybrid vehicles and large stationary grids.[24] Various rechargeable batteries of different chemistries based on conversion type electrodes such as metal–sulfur (*e.g.*, Li–S and Na–S) and metal–selenium (*e.g.*, Li–Se and Na–Se) are appealing due to their astonishing gravimetric/volumetric energy.[24–28] As mentioned earlier, for stationary grid storage and hybrid/electric vehicles, large-sized LIB packs are available. However, these alternative rechargeable secondary batteries will be more practical due to their projected much higher gravimetric/volumetric energy at a relatively low cost and a small size.

The cell structure of these rechargeable batteries generally comprises of a metal M (Li or Na) anode, suitable electrolyte (aqueous/non-aqueous), and X (S, Se) cathode. Lithium (Li) is the most suitable candidate among all the metal (M) anodes with a profoundly negative reduction potential of −3.04 V *vs.* the standard hydrogen electrode (SHE) and a high gravimetric capacity of ~3861 mA h g^{-1}. In contrast, sodium (Na) exhibits a relatively low gravimetric capacity of ~1166 mA h g^{-1} and a lower reduction potentials of −2.7 V *vs.* SHE.[2,27,29–32] However, Na is far more abundant than lithium (crustal content – Li (20 ppm), Na (23 000 ppm)), and cheaper, which thus has prompted researchers to explore new chemistries by integrating Na with conversion-based cathodes.[2,33,34]

Among the high energy density conversion-based cathodes (X) from group 16, S is one of the most compelling candidates. In 1962, Herbert and Ulam reported for the first time the use of elemental sulfur (S_8) as a high capacity cathode (1675 mA h g^{-1}) in rechargeable batteries.[35,36] Despite their high energy density compared to conventional Li-ion batteries, metal–S batteries

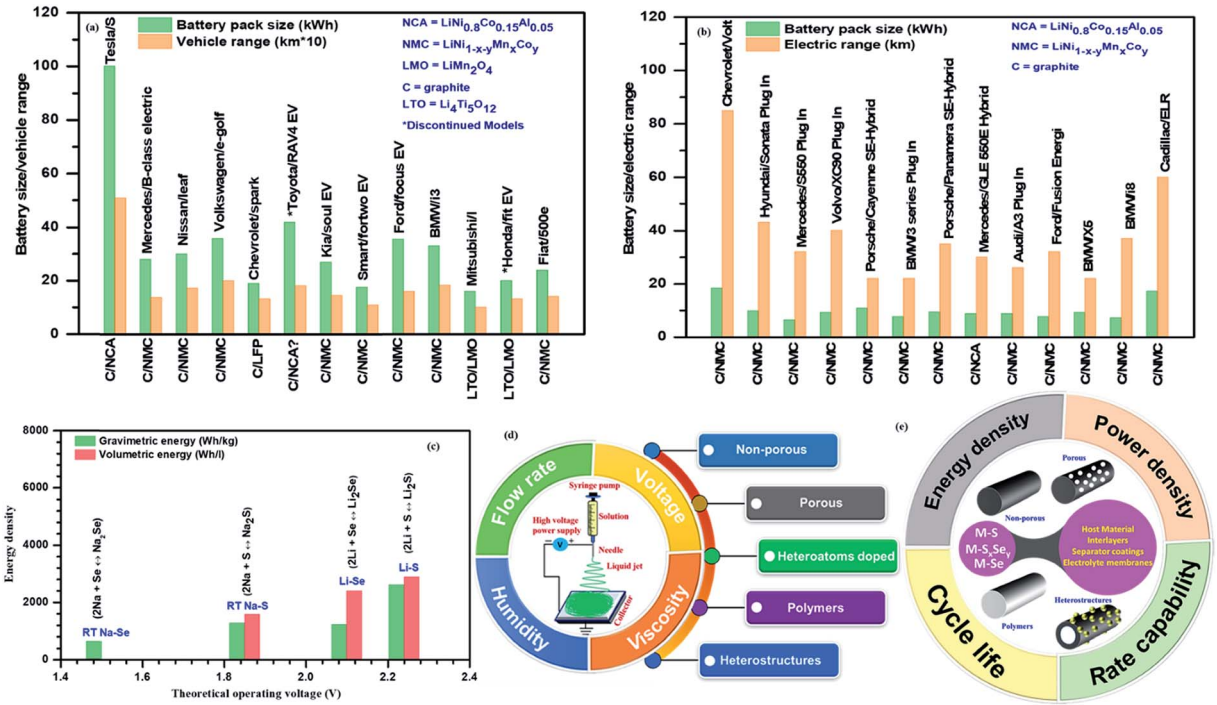

Fig. 1 Battery size and electric vehicle range for various available models of LIB packs for (a) hybrid vehicles and (b) electric plug-in vehicles. The *x*-axis shows various chemistries (cell structures) in these batteries. The model/company details are mentioned vertically in figures for each battery pack. (c) Gravimetric and volumetric energy densities of X (S, density ~1.96 g cm^{-3}; Se, density ~4.819 g cm^{-3}) cathode based rechargeable batteries using M-metal anodes (Li^+ and Na^+). (d) A typical electrospinning set-up and parameters influencing the physical properties of different nanofiber structures, and (e) a schematic showing the use of different electrospun structures as various components in M–S, M–S_xSe_y and M–Se batteries and their effect on the electrochemical characteristics (*e.g.*, energy and power densities, cycle life, rate capability) of these devices.

did not attract significant interest due to their very short cycle life.[35] The seminal work reported on Li–S batteries by Nazar's group in 2009 with rationally designed S-cathodes resuscitated the attention worldwide for revisiting the potential of room temperature metal–sulfur batteries. Fig. 1(c) presents the theoretical gravimetric and volumetric energy density of various metal–sulfur (M–S) batteries and their maximum practical operating voltage.[23,36–44] Li–S batteries have the highest gravimetric energy density of ~2600 W h kg^{-1} compared to other M-anode based S batteries.[35,44] Due to their astonishing energy density, M–S batteries are also promising alternatives to large-sized LIB packs for future hybrid vehicles.[23,36–44] However, M–S batteries are plagued by various long-lasting technical challenges due to the lack of sustainable and highly reversible sulfur cathodes. In metal–S batteries, elemental S electrochemically reduces to M_2S_2/M_2S usually through the formation of soluble intermediate metal-polysulfides (M_2S_n; $3 \leq n \leq 8$).[44,45] The critical challenges for the practicality of metal–S cells are (1) the low conductivity of S, *i.e.*, 5×10^{-30} S cm^{-1} at 25 °C (undermined sulfur utilization and low capacity) and solid-state products M_2S_2/M_2S, (2) high reactivity (harmful by-products), (3) substantial volume expansion during reduction (*e.g.*, ~80% in Li–S batteries from S (2.07 g cm^{-3}) to Li_2S (1.66 g cm^{-3}) conversion) reactions (mechanical instability), (4) dendrite formation at the metal anode due to non-homogeneous nucleation (short cycle life), and (5) infamous shuttle phenomena of soluble polysulfides (low coulombic efficiency and short cycle life).[23,28,36–46] Significant progress has been made in M–S batteries with the introduction of advanced functional nanomaterials as sulfur hosts, polysulfide blocking (interlayer) layers, thin layers on separators and selective membranes (separators).[23,36–44]

Another promising candidate from group 16 (VI) is selenium (Se) with its salient features such as relatively low reactivity, electrochemically similar nature to sulfur, semiconductivity (1×10^{-3} S cm^{-1}) and more controllable chemistry in electrochemical cells.[47–51] In M–Se batteries, electrochemical reduction of Se to M_2Se (M = Li, Na) takes place through intermediate poly-selenides.[50] Therefore, M–Se batteries also suffer from ill-famed 'shuttle phenomena' in commonly used ether based liquid electrolytes and volume expansion of Se during reduction, as in the case of M–S batteries.

Moreover, metal–Se cells exhibit a low theoretical capacity of ~675 mA h g^{-1} due to the high mass of selenium in comparison to sulfur.[50] However, regarding volumetric capacity, a relatively higher density of selenium (4.809 g cm^{-3}) than sulfur (α-S, 2.07 g cm^{-3}) allows metal–Se batteries to compete with metal–S batteries (*e.g.*, 3467 mA h cm^{-3} for Li–S batteries and 3253 mA h cm^{-3} for Li–Se).[50] Other essential advantages of elemental Se are (a) a higher utilization rate and faster electrochemical reaction rate due to selenium's semiconducting nature, (b) a higher autoignition and melting point than S (S = 115.2 °C; Se = 221

°C) – relatively safer during short-circuiting and overheating, and (c) compatibility with cost-effective carbonate-based electrolytes due to considerably stable intermediate poly-selenides.[50] While M–Se batteries have invaluable advantages and compete with M–S batteries, they are still in their nascent stage.

In the last few decades, the development of nanoscale materials with different morphologies and dimensionalities (0-D, 1-D, 2-D, and 3-D) has played a determining role in the advancement of secondary M–X (S, Se) batteries. Among the nanoarchitectures explored in these batteries, electrospun 1-D materials have emerged as the forerunner due to their interesting peculiarities such as 1-D longitudinal electron transport, a high surface to volume ratio and less agglomeration than ordinary nanoparticles.[52] Among many available synthetic strategies including template-directed synthesis, the solution-phase method, the vapor-phase route, self-assembly, and electrodeposition, electrospinning is one of the most straightforward, cost-effective, and industrially viable technologies for developing 1-D nanofibrous materials.[53] Electrospinning is a versatile technique that uses an electrohydrodynamic mechanism to fabricate 1-D organic, inorganic and hybrid nanofibers on a large scale with the incorporation of interesting properties such as porosity, low density, and controllable dimensions/diameters.[53] Moreover, electrospinning allows the production of application-oriented homogeneous and heterogeneous nanofibers in a variety of solid non-porous, porous, hollow, and core–shell architectures for their use in different M–X (S, Se) batteries.[53–56] In the recent past, rationally designed electrospun carbon nanofibers (CNFs), functionalized carbon/polymer nanofibers, composite nanofibers (*e.g.*, CNFs/oxides and CNFs/carbides), and heteroatom-doped nanofibers (*e.g.*, N-doped CNFs) have been utilized in M–S batteries.[43,57–59] These nanostructures have shown great potential for M–S batteries not only as functional sulfur hosts for trapping the dissolved polysulfides (through physical adsorption and confinement, chemisorption, and polar or Lewis-acid type interactions), but also as electrolyte membranes/functional separator coatings, or interlayers.[43,58,59] As the electrochemistry of M–Se batteries is analogous to that of M–S batteries, there is a growing interest for the use of such electrospun nanostructures in M–Se batteries as selenium hosts, polyselenide blocking layers and functional separators. Since the gravimetric capacity (energy) of M–X (S, Se) batteries depends on the total weight of all the components, it is vital to eradicate the additional dead elements such as binders, current collectors (*e.g.*, Al foil) and conducting additives (*e.g.*, carbon black). Electrospun structures have the advantage of free-standing nature, which makes them even more suitable for such M–X (S, Se) batteries.[43,58,59]

There exist several articles that review the recent progress in the application of electrospun nanostructures in rechargeable batteries.[52,53,56,58,60–73] However, these review articles primarily focus on their use in Li-ion and Na-ion batteries and rarely discuss conversion cathode (S, Se) based batteries.[4,55,56,63,66,67,72,73] To the best of our knowledge, there is no review article in the literature comprehensively focusing on the recent progress made in various next-generation sulfur (Li–S and Na–S), sulfur–selenium (Li–S_xSe_y and Na–S_xSe_y), and selenium (Li–Se and Na–Se) batteries using rationally designed electrospun nanostructures. In this article, we critically review the synthesis strategies used for electrospinning of novel nanostructures and the recent progress accomplished with function-directed use of these nanostructures as cathodes, interlayers, and electrolyte membranes/separator coatings in lithium and sodium metal-based sulfur/selenium batteries. First, we provide an introduction of M–S (Se) batteries and a brief overview of the electrospinning technique to build a foundation for analyzing the structure–property correlation given in the literature. The review then focuses on the recent advances made in Li–S batteries using various electrospun nanostructures of (a) carbon, (b) polymer, and (c) oxide, carbide, and metal based heterostructures as cathodes, interlayers, separator coatings and electrolyte membranes. We further discuss the recently reported strategies for the advancement of RT Na–S and Se based lithium and sodium batteries (Li–S_xSe_y, RT Na–S_xSe_y and RT Na–Se) using electrospun nanostructures. Furthermore, we define a significant parameter denoted as the 'fraction of (electrochemically) active cathode (FAC)' and calculate the effective sulfur utilization and effective capacity in Li–S cells for a comparative analysis between various powder/slurry based nanomaterials and electrospun nanostructures. Finally, we provide a concluding remark on the state-of-the-art progress and remaining critical challenges along with prospects towards electrospun nanostructure based M–S (Se) batteries.

2. A brief introduction of electrospinning

Electrospinning is a fiber-spinning process that uses high voltage (~7–32 kV) to produce fibers with controllable diameters ranging from a few nm to micrometers. It is a versatile technique that can be tailored to control the degree of graphitization, heteroatom functionality (*i.e.*, N), and a variety of function-directed homogeneous and heterogeneous complex architectures such as hollow, core–shell or porous nanofibers.[53] An electrospinning set-up typically consists of four major components *viz.*, a metallic needle with a blunt tip, a high voltage source/electric field supply, a syringe filled with a viscous polymeric/spinning solution, and a grounded conducting substrate/collector (*e.g.*, Al-foil) as shown in Fig. 1(d).[54] During the electrospinning process, when the applied electric field (voltage) overcomes the surface tension of the solution droplet, the charged solution gets ejected as a jet towards the grounded conducting collector.[55] The jet typically undergoes a whipping motion enabling significant thinning of the diameter. While traveling to the collector, the solvent evaporates from the jet solution and charged fibers eventually get accumulated on the collector.[74] This spinning procedure gives a non-woven fiber mat made up of nanofibers with diameters between a few nanometers to micrometers. Several factors are known to influence the diameter of nanofibers and the final nanostructure including the intrinsic properties of the spinning solution such as electrical conductivity, concentration, surface tension and viscosity as well as operating conditions such as the

flow rate, applied voltage/electric field intensity, tip-collector distance and humidity.[54,55,74] Since surface tension, conductivity and concentration are related to the spinning solution, which is largely determined by the targeted application, the flow rate of the solution turns out to be a critical factor in determining the diameter of fibers as follows:[54,75]

$$D_f \sim c^{1/2} (Q/I)^{2/3} \gamma^{1/3}$$

where D_f is the fiber diameter, 'c' is the concentration, 'Q' is the flow rate, γ is the surface tension, and 'I' is the characteristic current of the spinning set-up. Therefore, following the above power law, the diameter of the fibers is predicted to increase with the increasing flow rate, which is in agreement with the experimental findings reported earlier.[76] The diameter of the fibers is also influenced by the viscosity and generally increases with increasing viscosity of the solution as follows:[54,75]

$$D_f = k\eta^n$$

where η is the viscosity of the spinning solution (η is proportional to M^a), M is the molecular weight of polymers, k and a are constants (function of applied temperature, type of polymer and solvent), and n depends on polymers. The diameter of the as-spun fibers further decreases during heat treatments (for the formation of carbon, for example) due to evaporation of the residual solvents and removal of heteroatoms. Furthermore, the viscosity and surface tension of the solution must be adequate in order to get smooth fibers. A solution with a very low viscosity will result in particles (electrospraying) instead of continuous smooth fibers (electrospinning).[54,55,74] In contrast, a solution with a very high viscosity will be enormously hard to pull and will result in an unstable feed rate.[54,55,74,75] Humidity is another factor, which strongly affects the morphology of the fibers. A highly humid environment will result in condensation of water on the fiber surface and lead to pore formation on the surface.[54,55,74] The applied voltage and tip-collector distance also affect the structure and morphology of the fibers. A high applied voltage and small tip-collector distance will reduce the time for the solvent to evaporate and result in bead formation. Therefore, the tip-collector distance (voltage) should be optimum to form bead-free smooth fibers.[54,55,74,75]

The electrospinning technique offers immense opportunities to develop unique fiber architectures such as porous, hollow, or core–shell by varying post-treatment conditions and polymer solutions or using specially designed spinnerets.[74,77] Generally, the porosity/textural properties can be controlled/enhanced by (a) changing the post-fabrication heating process (heating at different temperatures in different environments such as Ar, H_2, and CO_2),[78–80] (b) activating nanofibers with various agents (*e.g.*, KOH),[81] (c) using additional sacrificial polymers (*e.g.*, Nafion, polymethyl methacrylate, and polystyrene), along with the primary polymer such as polyacrylonitrile (PAN, a common polymer for carbon nanofibers with a high yield),[82–84] and (d) employing thermally stable and easily removable hard templates (*e.g.*, SiO_2, ZnO, Fe, Ni, and Fe).[53–55,74,75,77] Co-electrospinning or coaxial electrospinning techniques allow the synthesis of hollow or core–shell nanofibers to impart multiple chemistries/functionalities to a single fiber.[85,86] In these approaches, two different solutions flow into either single or two specially designed concentric capillaries/nozzles using two individual syringe pumps and eventually consolidate after stretching and solvent evaporation.[53,54,85,86] Hollow or core–shell nanofibers can be designed by carefully choosing solvents and precursors (polymers, alkoxides or salts) for core and shell solutions. The final structure of the fibers depends on the miscibility of the core and shell solutions. The miscible solutions usually result in various phases/porosity in fibers due to phase separation during solidification whereas immiscible solutions give core–shell nanofibers. Hollow nanofibers can be produced by carefully selecting the core solution (*e.g.*, mineral oil or aqueous), which can be easily removed by pyrolysis or selective dissolution using solvents/etching agents.[86] More details about the choice of core and shell solutions and governing electrospinning parameters to obtain hollow and core–shell nanofibers are available in recently published review articles.[52,85,86]

So far, we have discussed the pros and cons/challenges of various emerging rechargeable battery chemistries based on conversion type S and Se cathodes. Then we briefly introduced the electrospinning technique and various parameters influencing the final structure and morphology of the fibers. As mentioned above, the one-step electrospinning technique is capable of producing homogeneous/heterogeneous function-directed nanofiber structures on a large scale. In the recent past, various non-porous, porous, core–shell, and hollow nanofiber structures of carbon, metal oxides, polymers and composites have been introduced into M–X (S, Se) batteries aiming at their long cycle life, high coulombic efficiency and enhanced capacity. In the subsequent sections, we will focus on the use of such electrospun structures in various metal–sulfur (selenium) batteries as sulfur (selenium) hosts, polysulfide (selenide) blocking layers (interlayers), and selective membrane/separators. Finally, we will provide our conclusions and future prospects on the roadmap for developing M–X (S, Se) batteries using these advanced electrospun nanostructures.

3. Electrospun nanofibers in metal–sulfur and metal–selenium batteries

A typical metal–sulfur (selenium) battery comprises a sulfur (selenium) cathode, a separator, an electrolyte, and a metal (M) anode.[36,46,87] The difference between the electrochemical potentials of the anode (μ_M^{oc}) and cathode (μ_X^{oc}) in the open circuit state defines the maximum voltage that the M–S (Se) battery can hold (ϕ_{oc}).[46,51,87] Upon discharge, the electrochemical potential of the S (Se) cathode increases (μ_X) until the battery reaches the cut-off potential (ϕ).[46,51,87]

In a typical discharge process, S (Se) electrochemically reduces to M_2S/M_2Se (M^+: Li^+, Na^+) *via* soluble intermediate poly-sulfides (-selenides), *i.e.*, $(S, Se)_k^{2-}$ ($4 \leq k \leq 8$).[46,88] Therefore, M–S (Se) batteries typically show two plateaus during the electrochemical reduction of S (Se) to M_2S/M_2Se (Fig. 2(a)).[46,88]

The high plateau at a potential ϕ_{hp} (*e.g.*, ~2.30 V for S[46] and ~2.1 V for Se[88] in ether electrolyte based Li–S (Se) cells) corresponds to the reduction of elemental S (Se) to higher order soluble poly-sulfides (selenides) (region I).[36,46,47,50,51,89–93] In the case of M–S batteries, the most stable allotrope at 25 °C, *i.e.*, octasulfur (cyclo-S_8) known as orthorhombic α-S_8, is reduced through ring opening, resulting in the formation of soluble higher-order polysulfides (region I):[36,46,89–93]

$$S_8 + 2e^- + 2M^+ \rightarrow M_2S_8\ (M^+ = Li^+, Na^+)$$

On the other hand, trigonal Se (t-Se) constructed from Se chains is the most thermodynamic stable phase among all the major allotropes of Se. The reduction process of Se resembles that of the sulfur cathode, and therefore results in the formation of long chain polyselenides in ether electrolytes (region I):[47,50,51]

$$Se_8 + 2e^- + 2M^+ \rightarrow M_2Se_8\ (M^+ = Li^+, Na^+)$$

The sloped region (II) between the higher and lower plateaus (region with a change in chemical potential) is due to the conversion of higher order poly-sulfides (selenides) to lower order poly-sulfides (selenides) through disproportion reactions given below:[36,43,46,47,50,51,87,89–95]

$$3M_2S_8\ (M_2Se_8) + 2e^- + 2M^+ \rightarrow 4M_2S_6\ (M_2Se_6)\ (M^+ = Li^+, Na^+)$$

$$2M_2S_6\ (M_2Se_6) + 2e^- + 2M^+ \rightarrow 3M_2S_4\ (M_2Se_4)\ (M^+ = Li^+, Na^+)$$

The liquid–liquid transition of higher order polysulfides (polyselenides) to lower order polysulfides (polyselenides) is the most complicated step.[36,46,89–93] The second plateau at a lower potential ϕ_{lp} (*e.g.*, ~2.1 V for S[46] and ~1.95 V for Se[88] in ether electrolyte based Li–S (Se) cells) represents a further reduction of these lower order intermediate poly-sulfides (selenides) to solid state products, *i.e.*, M_2S/M_2Se (regions III and IV):[36,46,47,50,51,89–93]

$$M_2S_4\ (M_2Se_4) + 2e^- + 2M^+ \rightarrow 2M_2S_2\ (M_2Se_2)\ (M^+ = Li^+, Na^+)$$

$$M_2S_2\ (M_2Se_2) + 2e^- + 2M^+ \rightarrow 2M_2S\ (M_2Se)\ (M^+ = Li^+, Na^+)$$

The transition of solid-state S (Se) to soluble polysulfides (polyselenides) and lower order polysulfides (polyselenides) to solid-state M_2S_2 (M_2Se_2) involves fast or moderate kinetics,

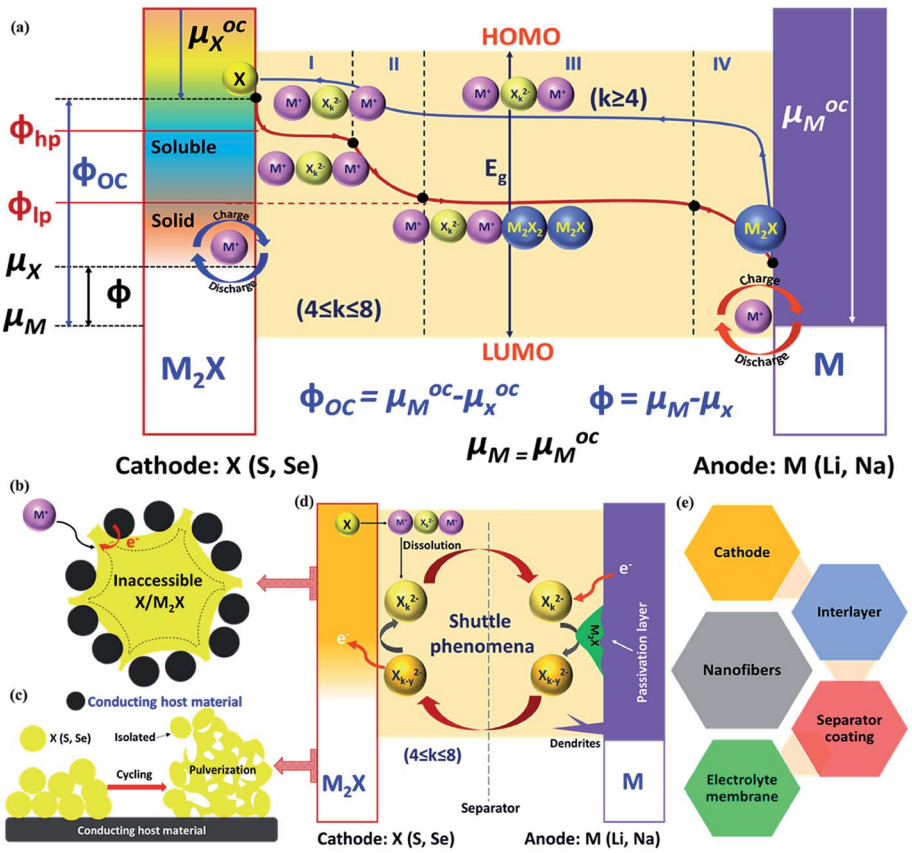

Fig. 2 A schematic showing (a) the fundamental electrochemistry involved in M–S (Se) batteries, (b) effect on the utilization of X (S, Se) due to inaccessible insulating cores, (c) pulverization of electrodes due to repeated volume changes, (d) loss of active material due to the shuttle effect and resultant passivation layer on the metal (M) anode, and (e) use of electrospun nanofibers as various components in M–S (Se) batteries.

while the last solid to solid transition of M_2S_2 (M_2Se_2) to M_2S (M_2Se) is kinetically slow and likely suffers from high polarization.[36,46,47,50,51,89–93] Consequently, the discharge process terminates rapidly once the M_2S (M_2Se) covers the whole cathode framework.[36,46,89–93] It is noteworthy that the discharge/charge rate, stability of intermediate species, electrolyte composition, chemical equilibria between polysulfide (polyselenide) species, and choice of solvent ultimately govern the mechanistic pathway for the conversion of S (Se) to M_2S (M_2Se).[36,46,47,50,51,89–93] During oxidation (charge), a reversible solid–liquid–solid process occurs and M_2S/M_2Se products convert back to elemental S (Se) *via* soluble intermediate polysulfides (polyselenides).[36,43,46,47,50,51,87,89–95] M–S (Se) batteries are confronted with long-lasting challenges, which are discussed below:

(i) The poor electrical and ionic conductivity of S and its deep discharge products M_2S_2/M_2S result in high internal resistance of the battery (large polarization → reduced energy efficiency of the battery).[36,46,89–93] Furthermore, due to the poor conductivity of S (or M_2S_2/M_2S), large insulating cores formed during S-infiltration/cathode preparation (or M_2S_2/M_2S deposition during discharge) become inaccessible and lead to underutilization of active material (low capacity) as shown in Fig. 2(b).[36,46,89–93] Therefore, use of S as a cathode material necessitates its integration with nanoscale conducting host materials.[36,46,89–93] Although Se has semiconducting nature, it also requires (like S) conducting host materials in order to suppress the shuttle effect and achieve long cycling and high coulombic efficiency.[47,50,51]

(ii) The repeated volume change (expansion during reduction and shrinkage during oxidation) during reduction/oxidation causes pulverization of the electrode (mechanical instability due to cracks, fractures, and loose contact (or complete isolation) of the active material with the conducting network or current collector) as shown in Fig. 2(c), which ultimately leads to fast capacity decay.[36,46,47,50,51,89–93]

(iii) The infamous shuttle effect, which involves the shuttling of dissolved polysulfides (polyselenides) between the M anode and S (Se) cathode during the charge process.[47,50,51] The shuttle effect results in the loss of active material and side reduction reactions with the M anode (passivation layer of M_2S/M_2Se) as shown in Fig. 2(d), which ultimately lead to a short cycle life.[36,43,46,47,50,51,87,89–95]

(iv) The anode (M) instability due to dendrite (Fig. 2(d)) and solid electrolyte interphase (SEI) layer formation, causing low deposition efficiency of M, and irreversible capacity loss upon the charging process or short circuiting of the battery system.[36,46,47,50,51,89–93] In this scenario, an excess amount of M is required to pair with the S (Se) cathode, which eventually deteriorates the energy density of battery systems.[36,46,47,50,51,89–93]

In the context of the practically challenging unique electrochemistry of M–S (Se) batteries, various rationally designed electrospun nanostructures of carbon, transition metal oxides, carbides, polymers, and nanocomposites have been employed in M–S (Se) batteries. These novel structures not only help to minimize the escape of polysulfides (selenides) towards the anode *via* physical or chemical adsorption and polar–polar, Lewis acid–base or thiosulfate type interactions but also provide channels for electron transfer and accommodate volume expansion during reduction/oxidation reactions. Consequently, these materials actively govern the capacity, rate performance, cycling and coulombic efficiency of M–S (Se) batteries. The following sections provide a comprehensive perspective of the recent progress made in M–S (Se) batteries with the use of various electrospun nanostructures as host materials in the cathode, interlayers, separator coatings and electrolyte membranes.

3.1 Electrospun nanostructures in Li–S batteries

3.1.1 Carbon nanofibers in Li–S batteries

CNF-based cathodes with sulfur as the active material. Electrospun carbon nanofibers (CNFs) have attracted considerable attention for a long time in Li–S batteries as conducting host materials due to their low density, high surface to volume ratio, nanosized pore distribution, good electrical conductivity, and remarkable structural strength. However, electrospun CNFs from a single polymer matrix usually offer insufficient surface active sites due to their considerably small surface area (mostly non-porous) and micro/meso-pore volume. Therefore, S-cathodes prepared using these non-porous CNFs and the most common melt-sulfur infiltration technique (155 °C/10–12 h) result in accommodation of sulfur mostly into inter-fiber macropores/voids, which limit prolonged cycling of the Li–S cell due to severe polysulfide dissolution.[96] Over the past decade, electrospun carbon nanofibers with different morphologies and architectures have been designed for Li–S batteries to surmount these challenges.[81–84,97–111] Ji *et al.* reported early work with the use of PAN/PMMA (polyacrylonitrile/Poly (methyl methacrylate); mass ratio 1 : 1) derived electrospun porous CNFs (Fig. 3(a)) and chemically deposited sulfur as cathodes in Li–S batteries.[82] The prepared CNF–S with 42 wt% S in the composite showed a high specific capacity of ~1439 mA h g^{-1} at a 0.05C rate with 85% capacity retention after 30 cycles (Fig. 3(b)). The high specific capacity was attributed to a large contact area between the chemically deposited sulfur and porous CNFs (surface area = 123 m^2 g^{-1} and pore volume = 0.27 cm^3 g^{-1}). However, the poor cycling stability of these cathodes was possibly due to (a) significant loss of sulfur confined in pores under wetting conditions during cell operation (ether electrolyte), which ultimately resulted in severe polysulfide dissolution,[112] and (b) weak interactions (physical adsorption) of the intermediate polysulfides with nonpolar CNFs.[113,114] It is important to mention that addition of the additive and binder during cathode preparation ultimately reduced the sulfur content to 29.4% in this study. Recently, Zhang *et al.* developed free-standing porous graphitic carbon nanofibers (surface area = 409 m^2 g^{-1}) using *in situ* formed FeO_x nanoparticles (10–30 nm) (during carbonization at 800 °C in N_2) as a template and employed them in Li–S batteries without binders or additives.[105] The developed porous graphitic CNF/S cathodes (Fig. 3(c)) with a high sulfur loading of 70 wt% in the final cathode delivered a high initial capacity of ~840 mA h g^{-1} at a 1C rate with ~83% capacity retention over

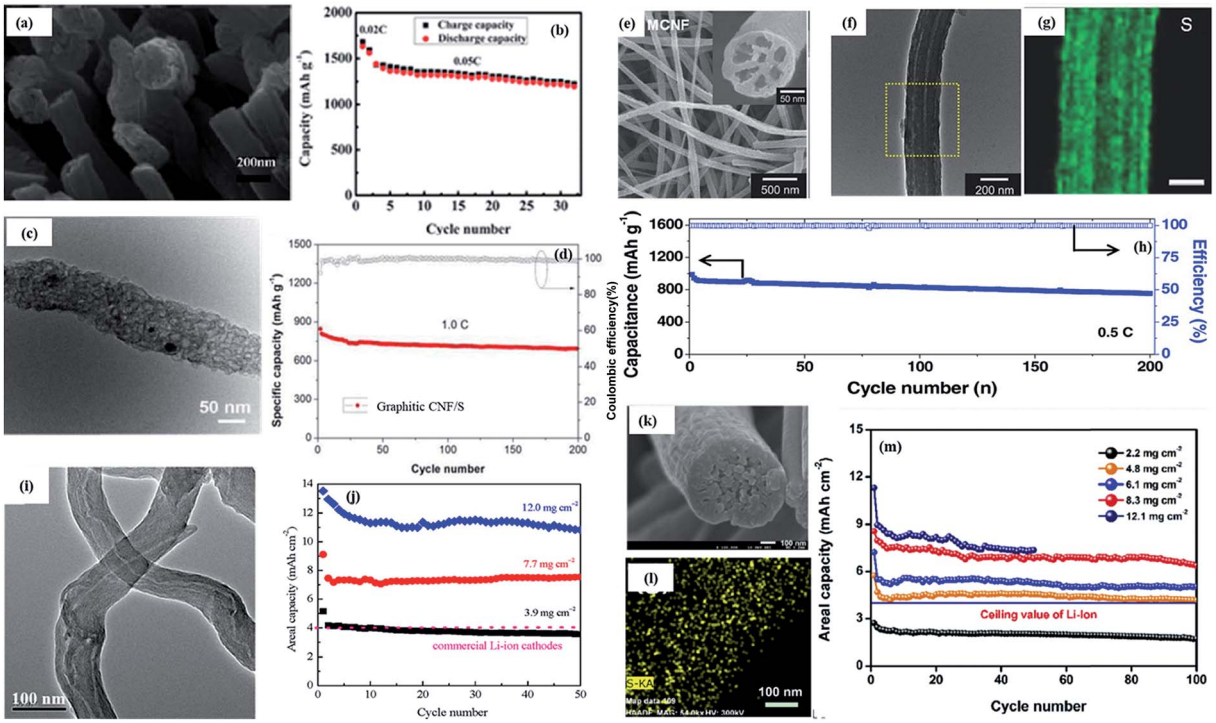

Fig. 3 (a and b) SEM image of the CNF–S nanocomposite and its cycling performance at a constant rate of 0.05C after an initial activation process at 0.02C for 2 cycles, respectively (reproduced with permission from ref. 82. Copyright 2014 the Royal Society of Chemistry); (c and d) TEM image of porous graphitic CNFs after sulfur infiltration, and the cycling performance and coulombic efficiency of graphitic CNFs/S cathodes for 200 cycles at a current rate of 1C (reproduced with permission from ref. 105. Copyright 2016 The Electrochemical Society); (e) low- and enlarged cross-sectional (inset) FE-SEM images of MCNFs, (f) TEM image of the sulfur-embedded MCNFs, (g) EELS dot mapping of the sulfur in sulfur-embedded MCNFs (scale bar: 50 nm), and (h) discharge capacity and coulombic efficiency of MCNFs/S cathodes with ~4.6 mg cm^{-2} sulfur loading over 200 cycles at a 0.5C rate (reproduced with permission from ref. 81. 2016 WILEY-VCH Verlag GmbH & Co. KGaA, Weinheim.); (i and j) TEM image of the CNF/CNT electrode and areal capacity of CNT/CNF/S cathodes with different sulfur loadings by stacking different layers during cycling at a current density of 0.6 mA cm^{-2}, respectively (reproduced with permission from ref. 105. 2018 American Chemical Society); (k and l) FE-SEM image of the HPCNF/S cathode and EDS mapping of sulfur and (m) cycle performance of the Li–S cells with the HPCNF/S cathode at sulfur loading from 2.2 to 12.1 mg cm^{-2} at a 0.2 C-rate (reproduced with permission from ref. 111. 2017 Elsevier Ltd).

200 cycles (Fig. 3(d)). The excellent electrochemical performance of the porous graphitic CNF/S cathodes was ascribed to several structural advantages including porous carbon structures (polysulfide reservoirs), improved electrical conductivity of CNFs due to graphitization (efficient sulfur utilization and fast reaction kinetics), and inherent macropores/voids (facile diffusion of Li^+ ions) of free-standing interlaced nanofibers. It is important to mention that the areal capacity of Li–S cells is mostly under-emphasized in the literature, but it is as crucial as the gravimetric capacity for practical applications. The areal capacity of the CNF/S based Li–S cells discussed above is <5 mA h cm^{-2}.[81,82,105] Considering the lower average voltage (~2.15 V) than that of LIBs (~3.5 V), practical Li–S cells will need to have an areal capacity of ≥6 mA h cm^{-2} and a specific capacity of ≥800 mA h g^{-1}. Therefore, practical Li–S cells demand an areal sulfur loading of ≥5 mg cm^{-2} along with a high sulfur content (≥70% in the final cathode) and sulfur utilization (≥70%) to outperform the energy density of commercial Li-ion batteries (ceiling areal capacity ~4 mA h cm^{-2}).[115,116] These prerequisites recently encouraged researchers to develop Li–S batteries with a high areal sulfur loading and sulfur content. However, an increase in the areal sulfur loading (or areal capacity) and sulfur content brings about slow kinetics due to the formation of inaccessible cores of insulating sulfur, poor electrolyte wetting of the cathode, underutilization of sulfur, extreme pulverization of the cathode due to repeated volume change, and exacerbated shuttle effect. These severe issues ultimately result in the limited areal/gravimetric capacity, low coulombic efficiency, and compromised cycle life of Li–S batteries.[110,111] Therefore, many research efforts have been aimed at the development of structurally featured electrospun CNFs with a large pore volume and highly distributed pores to overcome the abovementioned problems.[84,110,111,117] The pore volume of the porous host matrix directly influences the achievable sulfur loading in the cathodes as given below:[91,96]

$$\text{Sulfur content } (\%) = 100 \times \frac{\frac{V}{1.8}d}{\frac{V}{1.8}d + 1}$$

where V is the pore volume, and d is the density of sulfur (2.07 cm^3 g^{-1} for α-S). In this regard, free-standing CNFs provide an

added advantage of large pore volume along with other benefits such as elimination of dead weight (binders, conducting additives and additional current-collectors). Besides the high pore volume, wide pore size distribution is another valuable asset of CNFs for their sustainable performance at a high sulfur loading. Micropores (<2 nm) in CNFs enable a large interfacial contact area with sulfur and serve as reservoirs for trapping the intermediate polysulfides. Nevertheless, micropores often lead to low pore volume (low sulfur content) and slow Li^+ transport (sluggish kinetics). In contrast, mesopores (2–50 nm) and macropores (>50 nm) of CNFs are desirable for achieving a high sulfur content and better electrolyte penetration but generally result in inferior cycling stability. Consequently, most recent focus is on the development of CNFs with complex hierarchical porosity (micropores as well as mesopores/macro-pores), which could potentially accommodate a high amount of sulfur through large pore volume, provide a large contact area for effective sulfur utilization, accommodate volume changes, and also trap polysulfides through micropores for prolonged cycling of Li–S batteries.[110,111] Moreover, the robust free-standing 3D architecture of interlaced CNFs could provide a high structural/mechanical strength at a high sulfur loading during the volume changes.[84,110,111,118] In most cases, the activation process or sacrificial templates have been used to design such CNF structures. For example, Lee *et al.* prepared sulfur cathodes (loading ~2.2 mg cm^{-2}, ~64 wt% in the final cathode) using multichannel carbon nanofibers (MCNFs; surface area ~1617 m^2 g^{-1} and pore volume = 1.82 cm^3 g^{-1}) developed through a single-nozzle co-electrospinning technique.[81] A PAN/PMMA blend was electrospun and then activated using KOH ($6KOH + C \rightarrow 2K + 3H_2 + 2K_2CO_3$; T = 800 °C) to prepare MCNFs. The MCNF structures possessed parallel mesoporous channels (hollow channels with a diameter of ~20 nm along the length of carbon fibers) interconnected to micropores (Fig. 3(e)). The sulfur was infiltrated by combining chemical precipitation and melt diffusion (155 °C/12 h) processes. The TEM and elemental mapping results showed that sulfur was infiltrated within the fiber as given in Fig. 3(f and g). The MCNFs/sulfur composite cathodes displayed excellent rate performance (initial capacity of ~1351 mA h g^{-1} at a 0.2C rate and 847 mA h g^{-1} at a 5C rate), maintaining ~68% of the initial capacity after 300 cycles at a 0.2C rate. Moreover, these MCNFs/S cathodes with ~4.6 mg cm^{-2} sulfur loading showed a high initial capacity of ~1000 mA h g^{-1} at a 0.5C rate with ~76% capacity retention after 200 cycles (Fig. 3(h)). The excellent electrochemical performance of Li–S cells was attributed to the novel MCNF structure where the parallel mesoporous channels promoted high sulfur loading and utilization, while microporous channels assisted with functional groups act as polysulfide reservoirs.

Similarly, Zhang *et al.* recently used sulfur infiltrated electrospun porous CNF/carbon nanotube (CNT) mats as cathodes and achieved a high areal capacity in Li–S batteries.[110] The free-standing porous CNF/CNT mats were fabricated by electrospinning a solution of SiO_2 (template)/PAN/CNTs in dimethylformamide (DMF) and tetrahydrofuran (THF) solvents. The pyrolysis of PAN and removal of SiO_2 nanoparticles allowed the CNF/CNT mats to achieve a high surface area of ~1020 m^2 g^{-1}, pore sizes between 2 and 10 nm, and a large pore volume of ~1.66 cm^3 g^{-1}. Moreover, the CNT structures embedded into CNFs (Fig. 3(i)) resulted in a more flexible 3D CNF/CNT architecture with improved electrical conductivity and mechanical stability. Therefore, the developed CNT/CNF/S cathodes (stacked two layers with a total sulfur loading of ~3.9 mg cm^{-2}, ~62 wt%) through the solution infiltration method (S/CS_2) displayed a high initial discharge capacity of ~1321 mA h g^{-1} (5.15 mA h cm^{-2}) at a 0.1C rate and excellent cycling stability with ~80% capacity retention after 100 cycles. Moreover, the CNT/CNF/S cathodes with a high sulfur loading of ~12.0 mg cm^{-2} (stacked three layers) showed an excellent areal capacity of ~10.8 mA h cm^{-2} (~900 mA h g^{-1}) even after 50 cycles (Fig. 3(j)). The incorporation of CNTs into electrospun CNFs add together the peculiarities of both the components into a free-standing 3D architecture, *i.e.*, robustness, electrical conductivity, interfiber macropores for better electrolyte accessibility, and eradication of inactive elements (*e.g.*, binders, conducting additives, and Al foil). These features of CNT/CNF/S cathodes allowed them to show a high areal capacity of ~10.8 mA h cm^{-2} (~900 mA h g^{-1}) at a high sulfur loading of ~12 mg cm^{-2}. More recently, Zhao *et al.* demonstrated Li–S batteries with an areal capacity of ~11.3 mA h cm^{-2} using electrospun root-like hierarchically porous carbon nanofiber (HPCNF) based free-standing sulfur cathodes.[111] The free-standing HPCNF mats were fabricated by electrospinning PVP (polyvinylpyrrolidone)/P123 (Pluronic P123)/TEOS (tetraethyl orthosilicate) solution followed by carbonization at 800 °C in an inert N_2 environment. The silica template formed *in situ* (assisted by P123) served as the pore-forming agent and helped HPCNFs to exhibit a surface area of ~1626 m^2 g^{-1}, a pore volume of ~3 cm^3 g^{-1} and combined micropores (<2 nm) and mesopores (2–50 nm). The HPCNF/S cathodes were prepared with various sulfur loadings (2.2–12.1 mg cm^{-2}) by combining solution (S/CS_2) and melt diffusion methods (155 °C/12 h). The FESEM image and elemental mapping of the HPCNF/S cathode showed that sulfur was infiltrated within root-like hierarchically porous carbon nanofibers (HPCNFs) as given in Fig. 3(k and l). The unique free-standing HCPNF/S cathode material with 12.1 mg cm^{-2} sulfur loading exhibited an areal capacity of ~11.3 mA h cm^{-2} at a 0.2C rate in the first cycle (sulfur utilization >80%) and retained an areal capacity of ≥7.5 mA h cm^{-2} over 50 cycles. Moreover, at 8.3 mg cm^{-2} (~80 wt%) sulfur loading, these HPCNF/S cathodes delivered an initial areal capacity of ~9 mA h cm^{-2} and retained ≥6.0 mA h cm^{-2} after 100 cycles (Fig. 3(m)). The excellent performance of HPCNF/S cathodes was attributed to the unique root-like porous CNF structures (similar to the vascular structure in plant roots) with central macropores (along with the fiber diameter) surrounded by micro-/mesopores on the periphery. The developed robust free-standing 3D HPCNF architecture enabled better sulfur utilization, provided reservoirs for polysulfides and prevented the structural collapse during volume changes thus allowing Li–S batteries to sustain up to 100 cycles at a high sulfur loading.

Additionally, some efforts have been committed to altering sulfur infiltration conditions/methods into free-standing

electrospun nanofiber mats aiming at a high gravimetric/areal capacity of Li–S batteries.

For example, Yun *et al.* demonstrated a high areal capacity of ~7.9 mA h cm^{-2} in Li–S batteries using PAN-derived electrospun CNF (surface area = 23 m^2 g^{-1}) based sulfur cathodes.[108] The CNF/S cathodes were prepared by simply immersing CNF mats directly into a sulfur-containing slurry (Fig. 4(a)). The slurry was prepared using sublimed sulfur and the MWCNT additive (weight ratio of 95 : 5) in *N*-methyl-2-pyrrolidone (NMP) solvent followed by ultrasonication (2 h) and stirring (2 h) at room temperature. The disk shape punched 12 mm circular CNF electrodes were immersed in the slurry for 10 seconds and dried at 60 °C in a vacuum oven for 12 hours. The developed CNF/S cathodes delivered a high areal capacity of ~7.9 mA h cm^{-2} (~752 mA h g^{-1}) at a high sulfur loading of ~10.5 mg cm^{-2} with ~90.3% capacity retention (~7.14 mA h cm^{-2}) after 100 cycles (Fig. 4(d and e)). The excellent performance was attributed to solidification of the intermediate polysulfides into Li_2S in the inter-fiber macropores of the CNF matrix with specific wetting angles through cohesive forces as shown in Fig. 4(b and c).[108] Our group (Dillard *et al.*)[119] recently developed an ultra-rapid technique for sulfur infiltration requiring only 140 °C and slight pressure (<250 psi) for 5 seconds to design light-weight free-standing CNF (or other free-standing 3D substrates) based sulfur cathodes, which is cost-effective and scalable compared to conventional sulfur melt deposition techniques requiring high temperatures (155–300 °C), long times (8–10 h), and heavy components (Al foil) as a substrate for the slurry-cast process. Chung *et al.* then extended this ultra-rapid technique to achieve 10 mg cm^{-2} areal loading and ~65 wt% sulfur content in S/CNFs (although commercial CNFs).[120] The developed free-standing S/CNF cathodes delivered high gravimetric and areal capacity values of 415–730 mA h g^{-1} and 7–12 mA h cm^{-2} at a low E/S ratio of 6 μL mg^{-1} and achieved excellent capacity retention rates of over 70% after 200 cycles.

CNF-based cathodes with Li_2S as the active material. Fully lithiated Li_2S (a sulfur compound) is also a promising alternative cathode material for developing Li–S batteries with high energy density due to its high theoretical gravimetric capacity of 1166 mA h g^{-1} and ability to pair with safer Li-metal free anodes (*e.g.*, graphite, silicon, and tin).[121–124] However, the low electrical conductivity (10^{-13} S cm^{-1}) of Li_2S necessitates the use of conducting host materials for significantly improving its electrochemical activity.[121–124] Furthermore, the commonly used sulfur melt-infiltration techniques become impractical in the case of Li_2S due to its (a) very high melting temperature (1372 °C) in comparison to sulfur (~115 °C) and (b) environmental sensitivity of Li_2S, which makes the cathode preparation more stringent.[125] There are few reports on the development of Li_2S/carbon cathodes for Li–S batteries using alternative methods such as solution precipitation from organic lithium compounds or ball-milling.[121–124] However, these studies show limited areal capacity (<2 mA h cm^{-2}) in Li–S batteries due to a low Li_2S loading (<2 mg cm^{-2}).[121–124] Furthermore, these studies use expensive Li_2S as a raw material/precursor, which increases the overall cost of cathode production. There is surprisingly not much attention paid to the development of Li_2S based free-standing cathodes. The few papers that exist in the literature focus on the development of free-standing Li_2S/CNF composite materials using the electrospinning approach.[125,126] Among these studies, Yu *et al.* demonstrated the most impressive areal/gravimetric capacity of Li–S batteries using electrospun free-standing Li_2S/CNF composite cathodes.[125] The free-standing Li_2S/CNF cathodes were developed by electrospinning a blend of highly stable (against moisture and oxygen) inexpensive lithium sulfate (Li_2SO_4) and PVP polymer under ambient conditions (Fig. 4(f)). Here, the carbothermal reaction between Li_2SO_4 and carbon ($Li_2SO_4 + 2C \rightarrow Li_2S + 2CO_2$) at a high annealing temperature (800 °C) led to the formation of ultrafine Li_2S nanoparticles in the conducting CNF network. After the simple electrospinning process, the triple-layered Li_2S/CNF

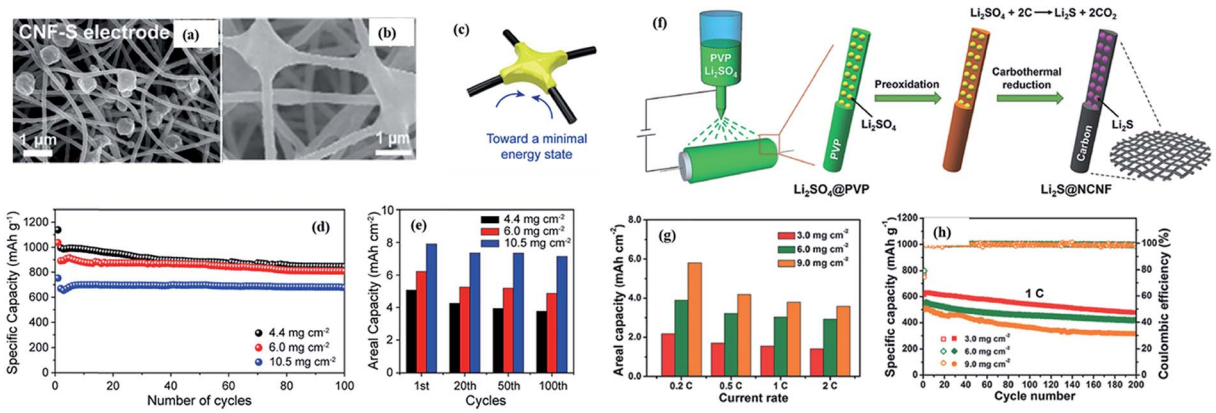

Fig. 4 SEM image of (a) the CNF/S cathode and (b) after first charge CNF/S cathode, (c) schematic of the deposition of sulfur species during the electrochemical reaction *via* the cohesive force of viscous polysulfides, and (d and e) cycle performance and areal capacity of CNF/S cathodes (0.1C) with sulfur loadings of 4.4, 6.0, and 10.5 mg cm^{-2}, respectively (reproduced with permission from ref. 108. Copyright 2017 American Chemical Society); (f) schematic illustration of the production of freestanding flexible Li_2S/CNF paper electrodes *via* Ar-protected carbothermal reduction of Li_2SO_4@PVP fabrics made by electrospinning under ambient conditions, (g) cycling performance and coulombic efficiency of Li_2S/CNF cathodes with Li_2S loadings of 3.0, 6.0, and 9.0 mg cm^{-2} at 1.0C, and (h) areal specific capacities of Li_2S/CNF cathodes with various Li_2S loadings at varied current rates of 0.2–2.0C (reproduced with permission from ref. 125. 2016 WILEY-VCH Verlag GmbH & Co. KGaA, Weinheim.).

cathodes with a very high areal loading of Li_2S (9.0 mg cm^{-2}) delivered an initial areal capacity of 4.68 mA h cm^{-2} and a gravimetric capacity of 520 mA h g^{-1} with ~65% retention over 200 cycles (Fig. 4 (g and h)). The excellent performance was attributed to homogeneously dispersed ultrafine Li_2S nanoparticles in the mechanically robust conducting interwoven 3D architecture of the CNF. Moreover, this simple single-step electrospinning approach greatly reduced the cost of production and the processing complexity of Li_2S cathodes.

CNF-based cathodes with a catholyte as the active material. Similarly, the use of polysulfides (Li_2S_k) as the starting active material (known as catholytes) has proven to be a promising approach to increase the areal capacity of Li–S batteries.[127–129] The catholyte provides enhanced Li^+ transportation and reaction activity over solid state sulfur thus results in better utilization of the active material at a high loading.[127] To this end, there are a few approaches in the literature centered on the development of self-standing 3D architectures for catholytes *via* electrospinning as it can provide 3D long-range conducting channels for electron transfer and voids for high volume catholyte loading.[127,129] For example, Han *et al.* recently demonstrated an outstanding areal capacity of a Li–S pouch cell using electrospun CNF/reduced graphene oxide (rGO) as the conductive framework for hosting lithium polysulfide (Li_2S_6) containing a liquid catholyte.[129] The developed CNF/rGO/catholyte electrodes delivered an areal capacity of ~15.5 mA h cm^{-2} corresponding to a sulfur loading of ~20.3 mg_{sulfur} cm^{-2} with >80% capacity retention over 50 cycles. The synergy between the Li^+ conducting Li_2S_6 catholyte and electrically conducting free-standing 3D CNF/rGO architecture led to such excellent performance. The electrolyte to sulfur (E/S) ratio is another critical parameter, which is essential in determining the final energy density of Li–S batteries. It has been realized that even with outstanding gravimetric/areal capacity at a satisfactory sulfur loading and utilization, the final energy density of Li–S batteries cannot outmatch that of commercial LIBs with the use of an excessive amount of electrolyte (>4 μL mg^{-1}).[91] To address this issue, Agostini *et al.* recently designed Li–S cells with a high areal capacity of ~4.8 mA h cm^{-2} (~800 mA h g^{-1}) at a relatively low E/S ratio of ~1.66 μL mg^{-1} (10 μL cm^{-2}).[117] In this study, first, self-supporting, binder-free, functionalized CNFs were prepared through electrospinning of a solution containing PAN/PMMA/SiO_2. The as-spun nanofibers were then stabilized in air at 250 °C for 1 h and subsequently, carbonized at 700 °C for 3 h under a constant Ar/H_2 (95 : 5) flow to get CNFs with oxygen functionalities. Then, a solution of 1 M Li_2S_8 in dimethyl ether (DME) was dropped directly on the CNF at 100 °C, and DME was allowed to evaporate to get final cathodes with a sulfur loading of ~6 mg cm^{-2}. In this process, most of the deposited Li_2S_8 polysulfides were dissolved in the electrolyte and resulted in *in situ* formation of the catholyte. Part of sulfur species were retained on the CNF as inactive Li_2S–(S)–O_3 species. The developed CNF/S cathodes displayed an areal capacity starting from ~5.4 mA h cm^{-2} (900 mA h g^{-1}) and stabilizing at ~4.8 mA h cm^{-2} (800 mA h g^{-1}) with no further drop up to 400 cycles (coulombic efficiency 100%). The *in situ* formed catholyte and polar oxygen functionality of the CNF prevented the shuttling of polysulfides to the anode thus making it possible for these Li–S cells to deliver a remarkable performance at a meager E/S ratio.

Heteroatom doped CNFs as cathodes. Besides tuning the textural properties – porosity and surface area of carbon materials – chemical doping with heteroatoms (*e.g.*, N and O) is also a promising approach for improving their activity in Li–S batteries.[129–137] The heteroatom doping in carbon materials can synchronously ameliorate their electrical conductivity, facilitate ionic transport and provide anchoring sites for strong coupling with intermediate polysulfides (B. E. = 1.3–2.6 eV).[114,134–136,138,139] In this context, Hou *et al.* systematically calculated the interaction energies of various hetero-atom (B, N, O, F, P, S, and Cl) doped nanocarbon (C) with intermediate lithium polysulfides (Li_2S_k) using density functional theory (DFT).[140] Based on their DFT calculations, rationales to favor a stiff binding with lithium polysulfides are summarized as follows:

(1) The dopant should have a lone pair of electrons (Lewis base) to interact with Li (Lewis acid) of polysulfides *via* electrostatic dipole–dipole interactions.

(2) The dopant should possess a higher electronegativity than C atoms to generate a permanent dipole moment at the local doping site.

(3) The dopant should have a sufficiently small radius to pair with the Li of polysulfides.

(4) The dopant should exhibit a stable bonding to the C lattice in order to interact with lithium polysulfides reversibly.

With all these considerations, N has been found to be the most effective dopant for carbon materials in Li–S batteries as evident from the literature.[129–136,139,141–144] Due to its almost similar atomic size and high electronegativity (3.04) compared to that of carbon (2.55), it can easily replace C atoms and form bonds with neighboring C atoms.[140] The doped N atom in the C lattice is generally present in three distinctive forms *viz.*, pyrrolic N (rN), pyridinic N (pN) and graphitic (quaternary) N (gN). The *ab initio* calculations establish that the rN and pN forms of the doped N atom are more promising than gN for polysulfide trapping.[145] An inclusion of pN or rN atoms in the C lattice not only can improve the electrical conductivity for enhanced sulfur utilization but also can ameliorate the binding ability of carbon materials through $LiS_kLi^+\cdots N$ type interactions for cycling stability.[138,140,145] Besides other N-doped carbonaceous materials such as graphene[146] and hollow carbon nanospheres,[133] N-doped electrospun CNFs have been explored in Li–S batteries. For example, Liang *et al.* recently reported the use of N-doped CNFs (NCNFs) with 3D interconnected pores as a sulfur host in Li–S batteries.[131] N-doped CNFs were prepared by electrospinning a solution of PVP with varying contents (20%, 25%, and 30%) of PTFE (polytetrafluoroethylene) followed by carbonization at 1000 °C in a N_2 atmosphere. Here, PVP worked as a source of carbon as well as N doping atoms whereas PTFE served as the sacrificial polymer to generate pores. S–NCNF composites were prepared by grinding NCNFs and commercial sulfur together and heating at 300 °C in an Ar environment. Later, a slurry of S–NCNF in NMP solvent was prepared and coated on Al foil to get the final S–NCNF cathodes (~59 wt% sulfur in the final cathode).

The S–NCNF cathodes fabricated with a 25% PTFE content showed better performance with a high discharge capacity of ~1094 mA h g^{-1} at a C/2 rate and ~76% capacity retention after 300 cycles (Fig. 5(c)). The S–NCNF (25% PTFE) cathodes exhibited suitable 3D interconnected porous channels for the accommodation of volume changes, relatively high conductivity compared to that of the other two NCNFs (20% and 30% PTFE) for better sulfur utilization, and a significant fraction of rN (25.6%) and pN (15.7%) atoms in the C lattice for trapping polysulfides (a schematic of the lithium polysulfide adsorption in the N-doped carbon is given in Fig. 5(a and b)). These features allowed S–NCNF (25% PTFE) to show a high capacity and long-term cycling. Similarly, Gao *et al.* recently designed self-standing N and O dual-doped carbon nanofibers (NOCNFs) based on polymer chain design and electrospinning followed by carbonization at 800 °C for 1 h in a N_2 environment and used them as interlayers in Li–S cells with slurry based cathodes (~4.5 mg cm^{-2}, 80 wt% S in the whole cathode).[147] The solution for electrospinning was prepared by dissolving 4,4′-oxydianiline (ODA) and pyromellitic dianhydride (PMDA) in DMF with and without dicyandiamide. Here, dicyandiamide was introduced to substantially improve the N concentration in the polymer chains. The developed slurry-cast sulfur cathode based Li–S cells with the NOCNF interlayer delivered a high initial discharge capacity of ~947 mA h g^{-1} with ~84% capacity retention after 200 cycles (areal capacity ~3.54 mA h cm^{-2}) at a 0.1C rate and excellent rate performance up to 5C, superior to Li–S cells fabricated with a CNF interlayer and no interlayer. The

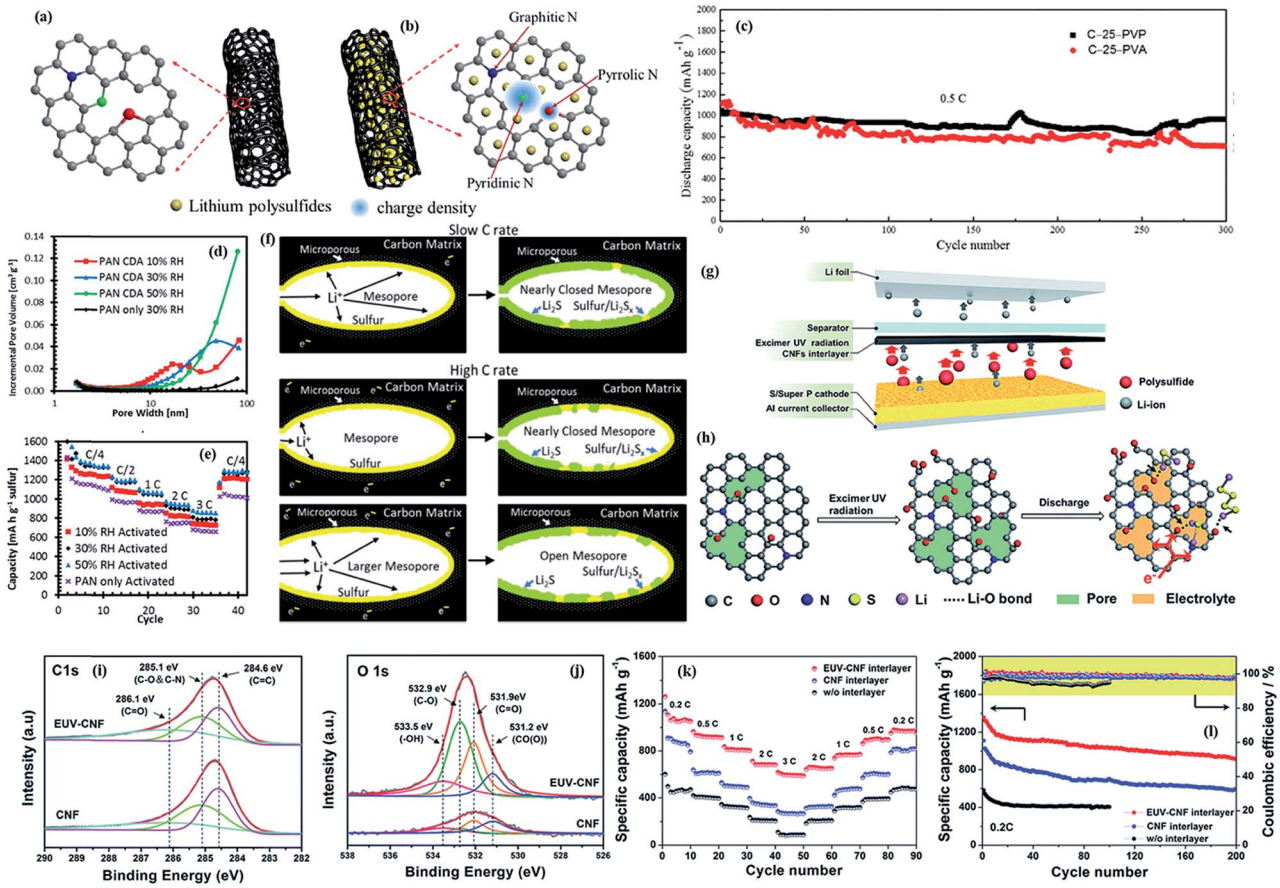

Fig. 5 (a and b) Schematic of the lithium polysulfide adsorption in the N-doped carbon: structure diagrams of NCNFs and the structure diagram for the trapping of lithium polysulfides by NCNFs and charge density of different nitrogen configurations, and (c) cycling performance of S–NCNF at a constant rate of 0.5C (reproduced with permission from ref. 131. Copyright 2018 Elsevier Ltd.); (d) incremental pore volume distribution of four carbonized and activated samples initially electrospun at different relative humidity (RH) levels. The first three samples are 1 : 1 blends of PAN and CDA and the fourth is PAN only, (e) rate performance with 10 cycles at 0.25C and 5 cycles at 0.5C, 1C, 2C, 3C, and 0.25C of cells with 18 mg interlayers of different mesopore and micropore distributions and 1.8 mg sulfur cathodes, and (f) illustration of the potential effect of the charging rate. At slow charging rates, lithium ions can have enough time to diffuse throughout the pore before reacting, while at higher charging rates, the ion does not diffuse as far, which nearly blocks the pore more quickly before all the sulfur is lithiated. Larger mesopores tend to have larger openings, which prevent diffusion limitations (reproduced with permission from ref. 150. Copyright 2016 The Electrochemical Society); (g) model of the assembled Li–S cell featuring a S cathode, EUV-CNF interlayer, separator, and Li metal. The EUV-CNF interlayer effectively blocks the migration of polysulfides to the Li metal during discharge. (h) Element content variation on the CNF surface before and after excimer UV light irradiation and the mechanism of polysulfide adsorption, (i and j) C 1s high-resolution and O 1s high-resolution XPS spectra of CNF and EUV-CNF interlayers, respectively, (k) rate performance of batteries with EUV-CNF, CNF, or no interlayer at current rates of 0.2–3C, and (l) charge–discharge capacities and coulombic efficiencies of the Li–S cells at a rate of 0.2C over 200 cycles (reproduced with permission from ref. 156. Copyright the Royal Society of Chemistry 2018).

authors showed that dual N and O functionality not only suppressed the shuttle effect with a strong polysulfide absorption ability but also improved the sulfur utilization in a two step reaction, especially from S_8 to Li_2S_4 conversion. Very recently, Yao *et al.* developed zeolitic imidazolate framework (ZIF-8) derived nitrogen-doped carbon nanofibers using an electrospinning/carbonization process and applied them as the current collector and binder free membrane containing a Li_2S_6 catholyte for lithium–sulfur batteries.[148] The Li–S cells based on the free-standing N–CNFs/Li_2S_6 membrane showed a high first-cycle discharge capacity of ~1175 mA h g^{-1} at 0.1C and excellent rate capability (~702 mA h g^{-1} at 1C), more stable electrochemical behavior than the CNFs/Li_2S_6 membrane. Furthermore, the Li–S cell with N–CNFs/Li_2S_6 (~3 mg cm^{-2} S loading) exhibited an initial discharge capacity of ~677 mA h g^{-1} and retained a capacity of ~467 mA h g^{-1} after 150 cycles. The superior performance of the NCNF membrane to that of the CNF membrane was ascribed to the synergistic effects of physical (porosity) and chemical (N-functionality) adsorption of lithium polysulfides and improved electronic conductivity of 3D free-standing NCNF membranes.

CNFs as interlayers. The use of carbon-based porous interlayers has also been proven to be beneficial for improving the performance of Li–S batteries. An interlayer is an additional freestanding film between the cathode and the conventional separator. Su and Manthiram proposed the concept of the interlayer for the first time by introducing a microporous carbon paper.[149] In this configuration, the C paper (interlayer) serves as an 'upper current collector', which improves the electrochemical performance not only by blocking (physical adsorption/van der Waals interactions) the lithium polysulfides but also by lengthening their diffusion pathways to the anode. Ever since the introduction of the interlayer concept by Manthiram and co-workers, many research efforts have been aimed at rational design of interlayers with a tunable pore size and surface area for Li–S batteries.[80,146,150–153] Electrospun freestanding nanofiber mats are desirable interlayers as they can be used without additional inactive elements (*e.g.*, binders and conducting additives).[80,150,152,154] In this review, our group (Singhal *et al.*) studied the effects of the surface area, pore size, and thickness of the freestanding binder-free electrospun CNF interlayers on the electrochemical performance of conventional sulfur cathode (60 wt% and *ca.* 1.45 mg cm^{-2}) based Li–S batteries.[152] We prepared three carbonized PAN-derived CNF samples (different in their textural properties) *viz.*, non-porous NCNF, CO_2 activated microporous CNF (ACNF), and micro–mesoporous CNF (MCNF) and used them as interlayers. We found that at a fast charging/discharging (1C) rate, the ACNF based Li–S batteries showed better capacity retention than the other two (NCNF and MCNF) interlayers. However, at a slow (C/5) rate, the capacity retention increased with increasing surface area and pore size (MCNF > ACNF > NCNF). More specifically, the MCNF at a C/5 rate delivered a high initial discharge capacity of ~1549 mA h g^{-1} and 83.1% capacity retention over 100 cycles. We suggested that mesopores present in the MCNF interlayers facilitate the reactivation of the deposited active materials (S during charge and Li_2S_2/Li_2S during discharge) thus resulting in higher capacity retention than that of the other two interlayers at a slow rate. Later, Williams *et al.* systematically investigated the dependence of the rate-performance of conventional S-cathode (slurry) based Li–S batteries on large mesopores in electrospun CNF interlayers.[150] The CNF interlayers with micropores and large mesopores (<10 nm) were produced by electrospinning a blend of two immiscible PAN and cellulose diacetate (CDA, sacrificial component) polymers in DMF solvent followed by carbonization (at 1000 °C for 8 h under a N_2 environment) and activation (at 350 °C in air for 4 h). The average size of the mesopores in the CNF interlayers was further adjusted between 17 and 50 nm by changing the humidity conditions (10%, 30%, and 50% relative humidity (RH)) during the initial electrospinning process as shown in the pore size distribution curve in Fig. 5(d). The change in relative humidity helped control the size of phase-separated domains in the blend before solidification thus helping to adjust the average mesopore size.[150] A reference microporous CNF interlayer was also prepared at 30% RH without the use of the sacrificial CDA polymer. Interestingly, the Li–S cell with the 50% RH CNF interlayer (largest pores) displayed maximum capacity retention at 1C, 2C, and 3C, approximately 850 mA h g^{-1} at 3C from the initial capacity value of ~1500 mA h g^{-1} at C/4. The Li–S cells with the 30% RH interlayer exhibited similar performance to the cell with the 50% RH CNF at C/4 and C/2 rates but did not perform well at high rates over 1C (Fig. 5(e)). Moreover, Li–S cells with the 10% RH CNF interlayer and 30% RH reference CNF interlayer (PAN only sample without CDA) showed the lowest capacity retention at high C rates (Fig. 5(e)). The excellent rate performance of the 30% RH and 50% RH CNF interlayers was attributed to the presence of large mesopores. At high C rates, polysulfides lithiate as soon as the Li^+ enters the pore, which leads to pore-narrowing and perhaps pore-blocking. Pore-narrowing (blocking) restricts the lithiation of other polysulfides due to limited diffusion of Li^+ ions. The authors suggested that the presence of large pores in the 30% RH and 50% RH CNF interlayers helped them to maintain the required current at high C-rates by facilitating the diffusion of Li^+ ions into the pores for polysulfide lithiation. The potential effect of the charging rate on the rate performance is schematically illustrated in Fig. 5(f). Recently, Lee *et al.* designed highly conducting graphitic carbon fiber felt (GCFF) through graphitization of electrospun PAN fibers and used it as an interlayer in conventional S-cathode (slurry; 0.7 mg cm^{-2} S) based Li–S batteries.[155] The GFCC was prepared using three steps: (I) stabilization of the as-spun PAN nanofibers at 250 °C for 3 h in air; (II) carbonization at 1000 °C for 3 h in an Ar environment; and finally, (III) annealing at 2800 °C for 2 h in an Ar environment. The Li–S with the GCFF interlayer delivered a high initial discharge capacity of ~1280 mA h g^{-1} at a C/5 rate with ~78.4% capacity retention over 100 cycles, which was much better than that achieved without a GCFF interlayer (initial capacity ~785.73 mA h g^{-1}, ~43.9% retention over 100 cycles). Moreover, at a 1C rate, the Li–S cell exhibited an initial discharge capacity of ~1554 mA h g^{-1} with ~53% capacity retention even after 300 cycles. It was shown that GCFF interlayers improved the reversibility of the reduction/oxidation process due to their

highly conducting graphitic structures and decreased the electrode polarization. More recently, Wu *et al.* used an excimer ultraviolet radiation (EUV) source to modify the surface functionality of an electrospun CNF interlayer (Fig. 5(g)).[156] The PAN-carbonized (at 800 °C for 6 h in argon) CNF interlayer was irradiated for 20 minutes (100% power) with a UV lamp in air (oxygen and moisture), which resulted in the formation of functional groups such as –OH and C=O (as shown in C 1s and O 1s XPS spectra in Fig. 5(h)) as well as nanopores on the surface of the CNF. The conventional S-cathode (~1.5 mg cm^{-2} S) based Li–S cell with the EUV-CNF (oxygenated functionalities) interlayer delivered the highest capacity of ~1262 mA h g^{-1} at a C/5 rate, which exceeded that of Li–S cells with the CNF interlayer (~1139 mA h g^{-1}) and with no interlayer (~603 mA h g^{-1}). Furthermore, the Li–S cell with the EUV-CNF interlayer exhibited long-term cycling stability with ~67.6% capacity retention over 200 cycles at a C/5 rate (Fig. 5(l)). Moreover, the Li–S cell with the EUV-CNF interlayer also showed an improved rate performance compared with the other two Li–S cells with the reference CNF interlayer and with no interlayer (Fig. 5(k)). The excellent performance of the Li–S cell with the EUV-CNF interlayer was attributed to the physical adsorption (pores) of polysulfides, favorable Li–O interactions with diffusing polysulfides *via* oxygenated surface functionalities (chemical trapping) (Fig. 5(h)), and improved utilization of the immobilized active material by the conducting CNF interlayer.

To summarize, electrospun CNF structures have played a significant role in the recent advancement of Li–S batteries. Li–S cells with excellent electrochemical performance have been reported by (a) controlling the pore size, pore volume and surface area of CNFs through activation agents (*e.g.*, KOH and CO_2) and sacrificial templates (*e.g.*, SiO_2 and PMMA), (2) modifying methods of sulfur infiltration into CNFs, and (3) using Li_2S or catholytes as starting materials with CNFs. Furthermore, the new Li–S cell configurations with CNF interlayers have also shown significant improvements. However, there is still a lot more room for improvement in the performance of Li–S batteries with electrospun CNF structures. The performance of Li–S batteries can be improved in future by rationalizing PS-functionality (optimal pores for sulfur loading and utilization, and polysulfide trapping), and e-functionality (conductivity and catalytic activity for reactivation of immobilized active materials) of CNF structures. Moreover, a deeper understanding of how key design parameters (*e.g.*, thickness, pore size, pore shape, pore volume, surface area, surface functionality, and heteroatom doping) of electrospun CNF materials affect the overall Li–S battery performance (*i.e.*, areal and gravimetric capacity, cycling, coulombic efficiency, and rate capability) is essential. This understanding can direct researchers toward improving Li–S battery performance and exceeding the ceiling gravimetric and areal capacity of commercial Li-ion batteries. In the following sections, we will now comprehensively review the recent progress made in Li–S batteries using electrospun polymeric and heterostructures.

3.1.2 Polymers in Li–S batteries

Cathodes and interlayers. The recent advancement of Li–S batteries has relied upon the use of various polymeric materials as cathodes, interlayers, and electrolyte membranes.[157–175] In this regard, the simple electrospinning technique allows innovative designing of polymeric structures to address the critical challenges imposed by Li–S chemistry. On the cathode side, the use of electronically conducting polymers such as polypyrrole (PPy) and polyaniline (PANI) with nitrogen functionality offers strong affinity towards lithium polysulfides through chemisorption thus helping in improving the cycle life.[160,167,170,176] For example, Zhu *et al.* recently designed a freestanding 3-D CNF/S/PANI composite architecture (schematic is given in Fig. 6(a)) by combining the electrospinning technique and *in situ* polymerization.[165] First, freestanding CNF mats were developed by electrospinning a PAN solution followed by stabilization and carbonization at 1000 °C for 1 h. Then, S was infiltrated into the CNF mats using S/CS_2 solution to ensure homogeneous distribution of S on the surface of the CNF and efficient contact between the CNF and S in the CNF/S electrodes. Finally, *in situ* polymerization of PANI was performed directly on the CNF/S structures using the aniline monomer, phytic acid, and ammonium persulfate to get the final 3D CNF/S/PANI architecture. The TEM image of single CNF/S/PANi and corresponding elemental mappings of C, S, and N elements revealed uniform distribution of S and PANi as shown in Fig. 6(b). The electrochemical performance was evaluated in an ethereal electrolyte prepared using 1 M bis(trifluoromethane)sulfonamide lithium (LiTFSI) and 0.1 M lithium nitrate ($LiNO_3$) in a solvent mixture of 1,2-dimethoxyethane (DME)/1,3-dioxolane (DOL) (1 : 1 by volume). The conventional slurry based C/S cathode (70 wt% S) and CNF/S cathode (1 mg cm^{-2} S; ~58 wt% S) exhibited an initial capacity of ~807 mA h g^{-1} and ~909 mA h g^{-1}, respectively, at a C/5 rate and maintained only ~44.8% and ~60.7% of their initial capacity after 300 cycles with a capacity decay rate of ~0.36 and ~0.13% per cycle, respectively. Importantly, the CNF/S/PANI cathode (1 mg cm^{-2} S; ~52 wt% S) displayed a high initial capacity of ~1278 mA h g^{-1} at a C/5 rate and retained ~74.6% of the initial capacity after 300 cycles with a capacity decay rate of ~0.08% per cycle (Fig. 6(c)). Furthermore, at a 2 mg cm^{-2} (~67 wt%) S loading, the CNF/S/PANI cathode showed a capacity of ~711 mA h g^{-1} at a C/5 rate after 300 cycles (Fig. 6(d)). The excellent performance of the CNF/S/PANI was attributed to the presence of the uniform PANI layer on the CNF/S structures. The conducting PANI layer in the 3D CNF/S/PANI architecture synergistically (a) improved the sulfur utilization, (b) inhibited the shuttling of polysulfides through their chemical trapping with N-rich functionality, and (c) helped to accommodate the volume changes and to maintain the structural integrity of the cathode. In another study, Li *et al.* demonstrated an improved electrochemical performance of Li–S batteries using electrospun cyclized-PAN–CNF (CP@CNF) interlayers.[171] In this work, first, freestanding CNF mats were fabricated by electrospinning a PAN solution in DMF solvent. The CNF mats were then immersed in a 5 wt% PAN solution for 30 s and dried at 80 °C or 12 h. The CP@CNF interlayers were finally achieved by stabilizing PAN coated CNF mats at 300 °C for 10 h in an Ar environment. A schematic of the CNF film, the PAN coated CNF film, the intermolecular cyclization reaction, the CP@CNF film

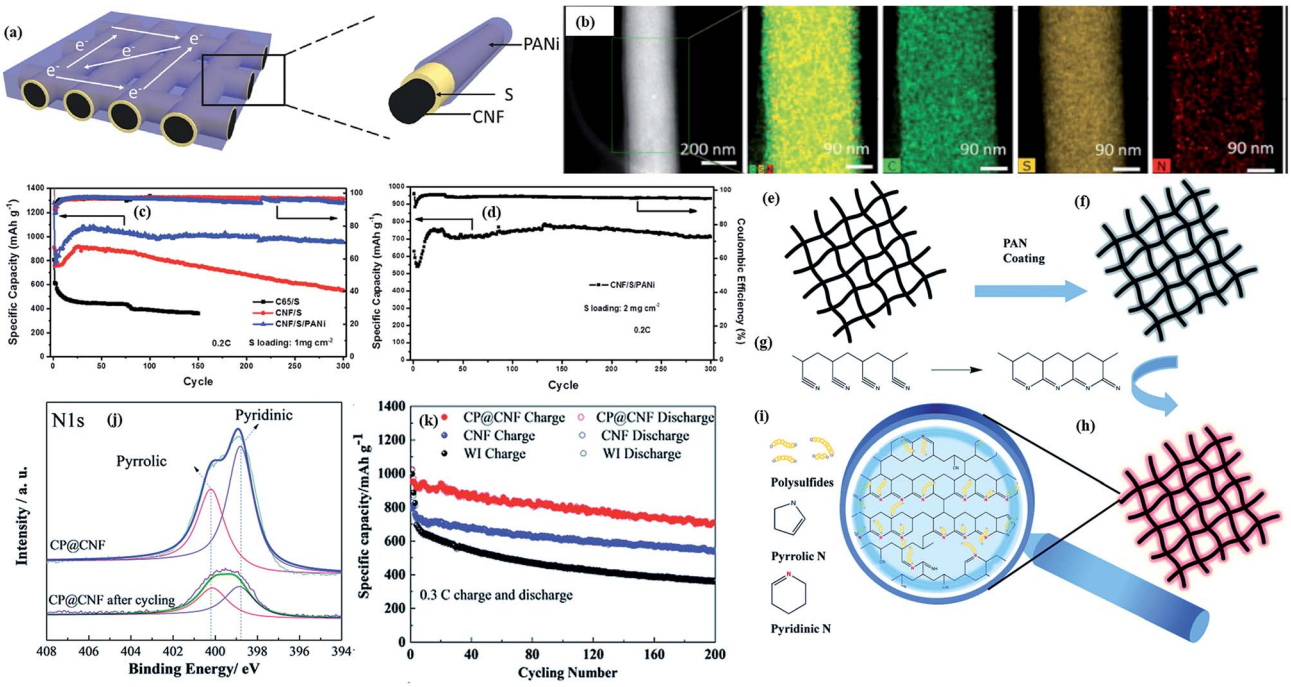

Fig. 6 (a) Schematic illustration of the CNF/S/PANI electrode configuration, (b) STEM image of single CNF/S/PANi and corresponding elemental mappings of C, S, and N elements revealing uniform distribution of S and PANi, (c) cycling performance of the CNF/S/PANi electrode at higher current densities of 0.5 and 1C (S loading: 1 mg cm^{-2}), and (d) cycling performance of the CNF/S/PANi electrode (S loading: 2 mg cm^{-2}) (reproduced with permission from ref. 165. Copyright 2018 WILEY-VCH Verlag GmbH & Co. KGaA, Weinheim.); (e–i) schematic of the CNF film, the PAN coated CNF film, the intermolecular cyclization reaction, the CP@CNF film and the chemical structures of cyclized-PAN, respectively, (j) XPS spectra of CP@CNF interlayers after cycling, and (k) cycling performances of Li–S cells with CNF, without CNF (WI) and CP@CNF interlayers at a 0.3C rate (reproduced with permission from ref. 171. Copyright 2016 the Royal Society of Chemistry).

and the chemical structures of cyclized-PAN is shown in Fig. 6(e–i). The electrochemical performance of Li–S batteries (with CNF and CP@CNF interlayers and with no interlayer) was evaluated using conventional slurry based cathodes (1.2 mg cm^{-2}; 60 wt% S) in the ethereal electrolyte (1 M LiTFSI in DME : DOL (v/v) with 1 wt% $LiNO_3$). The Li–S cell with the CP@CNF interlayer delivered a better cycling and rate performance compared to the other two Li–S cells with and without CNF interlayers. More specifically, the Li–S cell with the CP@CNF interlayer exhibited high reversible capacities of ~910 mA h g^{-1} (retention = 85.1%) and ~710 mA h g^{-1} (retention = 74.6%) after 100 and 200 cycles, respectively, at a 0.3C rate with a high coulombic efficiency of ~99.5% (Fig. 6(k)). In the CP@PAN interlayer structure, the conducting CNF skeleton serves as an upper current collector and enables better sulfur utilization. Using postmortem FTIR, XPS (N 1s XPS spectra are shown Fig. 6(j)) and TEM studies, it was shown that the cyclic-PAN layer with abundant polar C=N (*i.e.*, pN (pyridinic)) groups (compared to the CNF interlayer alone) minimizes the shuttle effect through both physical (similar to the CNF interlayer) and chemical trapping (chemisorption through p-electrons on pN) of polysulfides.

Electrolyte membranes. Recently, Shanthi *et al.*, for the first time, developed nanofiller incorporated freestanding poly(-vinylidene fluoride-*co*-hexafluoropropylene) (PVdF-HFP) membranes and used them as a host matrix for the preparation of gel polymer electrolytes (GPEs) – a liquid electrolyte incorporated into a polymer matrix.[157] In particular, they used commercial fumed f-SiO_2, and sol–gel derived nm-TiO_2 and nm-SiO_2 nanoparticulates as the nanofillers. The use of GPEs in Li–S batteries as electrolyte-separator assembly brings about several unique advantages over their liquid counterpart such as minimal electrolyte leakage, no internal short-circuiting, and reduced polysulfide dissolution and shuttle.[177,178] GPEs with electrospun porous and fibrous polymeric membranes have been shown to be more efficient in rechargeable batteries than fibrous membranes developed from melt or solution spinning due to their superior structural/mechanical stability and ionic conductivity.[157,179,180] Furthermore, the use of oxide nanofillers in GPE membranes has been shown to augment the ionic conductivity and mechanical properties of GPE films.[177,178] Therefore, Shanthi *et al.*[157] first prepared PVDF-HFP-oxide/nanofiller membranes by electrospinning a solution of PVDF-HFP (10 wt%), LiTFSI (0.1 wt%), and a nanofiller (nm-SiO_2/nm-TiO_2/f-SiO_2; 0.1 wt%) in a mixed solvent of acetone/DMF (3 : 7; w/w) followed by drying under vacuum at 60 °C for 12 h. The final GPEs were obtained by first heat pressing these membranes at 80 °C for 30 min at 1 atm pressure and then soaking them in an ethereal electrolyte (1.8 M LiTFSI and 0.1 M $LiNO_3$ in DME/DOL (1 : 1; v/v)) for 30 min. The SEM image of the electrospun PVdF-HFP polymer membranes with dissolved LiTFSI (10 wt%) and dispersed f-SiO_2 (10 wt%) is shown in Fig. 7(a). These GPEs were tested with commercial S-powder based cathodes in Li–S batteries. Control Li–S cells were also

examined under identical conditions replacing the GPEs with a liquid electrolyte and commercial polypropylene (Celgard 2400; PP) membrane separator.

The electrochemical results showed that an optimum GPE (E/S = 3–4 mL g^{-1}) based on PVDF-HFP/f-SiO_2 exhibits stable cycling performance over 100 cycles (fade rate ~0.056% per cycle) in Li–S batteries with an initial specific capacity of 895 mA h g^{-1} at a 0.1 C-rate (Fig. 7(b)). In contrast, Li–S cells with the commercial separator and liquid electrolyte displayed a low initial capacity of ~557 mA h g^{-1} that decreased to 132 mA h g^{-1} within 10 cycles, despite a high E/S ratio of 50–65 mL g^{-1}. The GPEs based on PVDF-HFP/f-SiO_2 serve as electrolyte-separator assembly in Li–S cells and have superior mechanical stability (Fig. 7(c)) due to interconnected PVDF-HPF nanofibers, high lithium ion conductivity (comparable to that of liquid electrolytes), and higher liquid electrolyte uptake (>250%) with structural stability. Furthermore, these membranes exhibit higher electrochemical stability and a lower interfacial resistance. Moreover, the GPE membranes help to reduce polysulfide dissolution and shuttle due to their smaller pore size (~15 nm) than the commercial separator (~25 nm). These attractive attributes of GPEs allowed Li–S cells to show superior performance. This recent work could motivate researchers to explore electrospun-membrane based GPEs in Li–S batteries at low E/S ratios.

Sulfurized PAN (SPAN) in carbonate electrolytes. Polymers have also played a significant role in enabling the use of commercially viable carbonate electrolytes for Li–S batteries.[181–183] From the perspective of capacity, the high solubility of intermediate lithium polysulfides in ethereal electrolytes is essential as it enables better sulfur utilization and complete reduction of S to Li_2S.[166,181–183] However, in most instances, the severe internal shuttle effect and Li-corrosion in ethereal electrolytes ultimately lead to low coulombic efficiency and short cycle life of Li–S batteries.[184] Furthermore, the low boiling point of commonly used ethereal electrolytes (*e.g.*, 75 °C for DOL)[184] and oxidizing nature of the $LiNO_3$ additive[185] (commonly used in ether electrolytes for stable SEI formation on the Li-anode) impose serious safety challenges for the operation of Li–S batteries at elevated temperatures.[181–183] On the other hand, the traditional carbonate-based electrolytes (*e.g.*, 1 M $LiPF_6$ in ethylene carbonate (EC) and diethyl carbonate (DEC) (v/v; 1 : 1)) are cost-effective and have a higher boiling point (*e.g.*, 243 °C for EC and 242 °C for PC), and very low solubility of polysulfides.[181–184,186,187] Nonetheless, the use of carbonate electrolytes is only possible under certain conditions due to the formation of thioether and methylated thiolate during discharge through a chemical reaction between

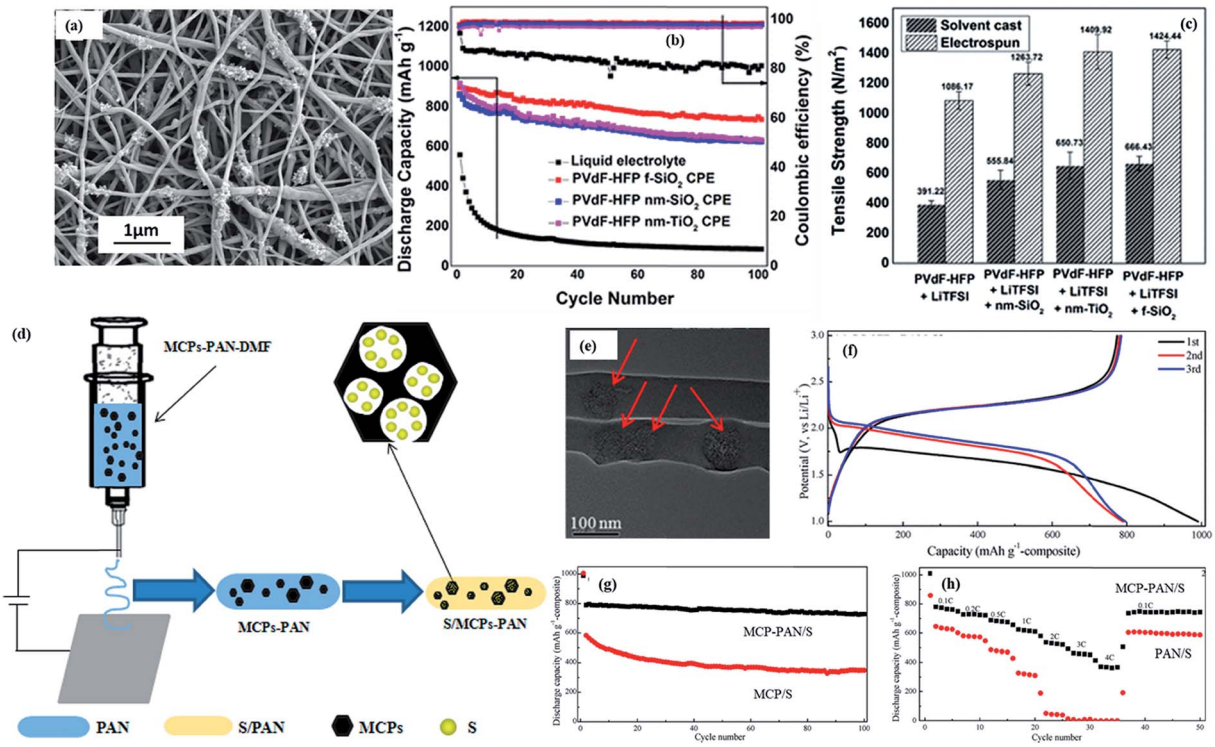

Fig. 7 (a) SEM images of electrospun PVdF-HFP polymer membranes with dissolved LiTFSI (10 wt%) and dispersed f-SiO_2 (10 wt%), (b) cycle performance and coulombic efficiencies of Li–S cells with different polymer membranes, and (c) comparison of tensile strengths of various electrospun and solvent cast membranes. Each datum represents an average of three independent tests run on three different samples under identical conditions. (Reproduced with permission from ref. 157. Copyright 2018 American Chemical Society); (d) illustration of the preparation process of MCPs–PAN/S multi-composites, (e) TEM image of MCPs–PAN nanofibers with MOF-derived MCPs indicated by red arrows, (f) initial three charge–discharge curves of MCPs–PAN/S cathodes (52 wt% S), (g) cycle performances of MCPs/S and MCPs–PAN/S (52 wt% S) at a current density of 160 mA g_{sulfur}^{-1}, and (h) high rate-performance of MCPs–PAN/S (52 wt% S) and PAN/S composites (reproduced with permission from ref. 189. Copyright 2017 American Chemical Society).

nucleophilic polysulfides (S_k^{2-}) and carbonates.[183,187] In this regard, two feasible solutions have been proposed: confining sulfur (short chains of sulfur; S_{2-4}) in microporous carbon (pore diameter <0.7 nm)[188] and using sulfurized polymers.[168] The short chains of sulfur confined in micropores or covalently bonded S in sulfurized polymers have been shown to give rise to a single plateau in the discharge cycle, which corresponds to a direct conversion of sulfur to Li_2S.[171,188] However, the confinement of S in micropores generally requires a complex multistep process and precise control of pore size in carbon using activation agents. The approach involving sulfurization of polymers is relatively simple.[188] Among sulfurized polymers, sulfurized PAN (SPAN) has received significant attention as a high-performance cathode material due to covalently bonded sulfur and nitrile groups of PAN.[160,166,171] The interaction of the nitrile group of PAN with Li_2S through coordination bonding allows uniform distribution of Li_2S.[160,166,171] Interestingly, Zhang *et al.* developed a novel structure of SPAN using electrospinning, which brings two approaches together – the confined short chains of sulfur and covalently bonded sulfur into a single material.[189] First, the synthesized zeolitic imidazolate framework (ZIF-8) was carbonized at 900 °C for 6 h under an Ar flow to get microporous carbon polyhedrons (MCPs). Then, MCP encapsulated PAN nanofibers were developed by electrospinning a PAN/MCP blend in DMF (TEM is given Fig. 7(e)). The PAN/S (without MCP as control) and MCP–PAN/S (52 wt% S) composites were developed by first heating the fiber with sulfur at 155 °C for 3 h and then heating at 300 °C for 4 h under an Ar flow. The preparation process of MCP–PAN/S multi-composites is summarized in Fig. 7(d). The final cathodes were prepared by casting a slurry of active material on Al foil with a sulfur loading of ~1 mg cm^{-2}. The electrochemical performance was evaluated using 1.0 M $LiPF_6$ in mixed solvents of PC/EC/DEC (1 : 4 : 5 by volume; DEC : diethyl carbonate) as the electrolyte. It is noteworthy that MCP–PAN/S cathodes showed charge–discharge curves with a single plateau (except in the first cycle), typically reported for S/microporous carbon or SPAN in carbonate electrolytes (Fig. 7(f)). Moreover, the MCP–PAN/S cathode delivered superior electrochemical performance including a large reversible capacity of ~790 mA h $g_{composite}^{-1}$ (~1519 mA h g_{sulfur}^{-1}) in the second cycle with ~84.4% capacity retention over 200 cycles (Fig. 7(g)), high S-utilization (~90.7%), large initial coulombic efficiency (~78.2%), and high rate capability up to 4C rate (Fig. 7(h)). The electrochemical results indicate that the presence of MCP in MCP–PAN/S synergistically overcomes the disadvantages (initial poor coulombic efficiency, low sulfur content and utilization, and poor rate capability) of individual components *viz.*, MCP/S (confined sulfur) and SPAN (sulfurized polymer) in carbonate electrolytes. While MCPs enable a sufficient sulfur loading, PAN nanofibers provide structural stability and offer 3D channels for easy ionic and electronic transport. Furthermore, S-contained PAN acts as a buffer layer, which significantly improved the initial coulombic efficiency by preventing the penetration of carbonate solvents without compromising the ionic and electronic transport.

In summary, the electrospun structures of polymers have shown great potential for the advancement of Li–S batteries in the recent past. In particular, the use of GPEs from electrospun polymeric membranes seems to be a foreseeable solution to the ill-famed shuttle effect. The future research efforts should aim at the development of electrospun GPE based Li–S cells under more realistic conditions in order to examine the viability of this approach. Similarly, sulfurized polymers are also promising cathode materials for Li–S batteries. However, the low sulfur content (electrochemically analogous to S_8), poor initial coulombic efficiency, and unsatisfactory rate performance of these sulfurized polymers are long-lasting limitations. More research efforts are required to rationally design the electrospun structures of sulfurized polymers in order to improve their performance further. At the same time, a better understanding of the role of electrochemically inert polymer chains would help to impart desirable properties to the sulfurized polymeric materials.

3.1.3 Electrospun heterostructures for Li–S batteries

Metal oxide based heterostructures. As discussed above, the electrospun CNFs with complex micro–mesoporosity and 3D interconnected channels for electrons and ions are capable of accommodating sulfur and physically blocking the diffusion of intermediate lithium polysulfides towards the Li anode. The introduction of heteroatoms into the conjugate nonpolar carbon planes can further enhance the functionality of CNFs, wherein doped-heteroatom sites can potentially anchor polysulfides through polar–polar and dipole–dipole interactions. Nanostructured polar inorganic compounds (*e.g.*, oxides and carbides) are another class of materials, which exhibit high binding energy with polysulfides.[190–197] These inorganic compounds strongly bind intermediate lithium polysulfides (B. E. = 2.6–7.0 eV) through polar–polar, Lewis acid–base or thiosulfate–polythionate conversion type interactions and can enable high capacity and long cycle life in Li–S cells.[113,114,195–198] However, the poor electrical conductivity of these organic compounds (*e.g.*, 5×10^{-30} S cm^{-1} for the vacancy free lattice of TiO_2) necessitates a rational design of their composites with conducting agents (*e.g.*, carbon).[195] In this context, electrospinning of hybrid organic/inorganic gel is the most straightforward approach, which simplifies the fabrication process of 3D CNF/inorganic heterostructures and allows direct anchoring of the inorganic component to CNFs.[190,199–201] In the recent past, various electrospun CNF/inorganic heterostructures have been explored as sulfur hosts, interlayers and Li-protection layers in Li–S batteries.[190,199,200,202,203] For example, Song *et al.* designed a 3D flexible CNF/graphene architecture decorated with ultrafine TiO_2 nanoparticles (C/G/TiO_2) using the electrospinning technique and employed it as a sulfur host in Li–S batteries.[204] The free-standing C/G/TiO_2 electrodes were prepared by electrospinning a solution of PAN/graphene oxide/TEOS/titanium isopropoxide (TIP) in DMF. The as-electrospun nanofibers were stabilized at 250 °C in air for 5 h and carbonized at 1000 °C for 2 h under an Ar/H_2 flow. The final free-standing C/G/TiO_2–S cathodes (1.2 mg cm^{-2}, 55 wt% S in the cathode) were developed by soaking the carbonized mats in S/CS_2 solution for 10 minutes and drying in air at 60 °C for 4 h.

A schematic illustration of the fabrication process of the C/G/TiO_2–S composite is given in Fig. 8(a). The SEM image (Fig. 8(b)) of the C/G/TiO_2–S composite showed that no bulk sulfur particles were found on the surface of C/G/TiO_2–S, showing a homogeneous distribution of S inside the CNF framework. The HRTEM image with lattice fringes and the selected area diffraction (SAED) pattern (Fig. 8(c)) of C/G/TiO_2–S further demonstrated that rutile type polycrystalline TiO_2 nanocrystals (circled with white dotted lines) were present with an average size of 5 nm.

The developed C/G/TiO_2–S cathodes delivered an initial capacity of 1501 mA h g^{-1} at C/10, excellent rate performance (668 mA h g^{-1} at 5C as shown in Fig. 8(e)) and long cycling stability (987 mA h g^{-1} at 1C with 62.6% retention after 500 cycles as shown in Fig. 8(f)). Moreover, the C/G/TiO_2–S cathodes with areal sulfur loadings of 2.4, 3.6, and 4.8 mg cm^{-2} exhibited initial capacities of 967, 890, and 814 mA h g^{-1} at a 1C rate, and capacity retentions of 76, 69, and 60% after 100 cycles, respectively (Fig. 8(d)). The excellent electrochemical performance of the C/G/TiO_2–S cathodes was attributed to (a) induced micro–meso-porosity (by sacrificial TEOS) and flexibility (by graphene) for accommodating the volume changes, (b) inherent 3D channels for facile transport of electrons and ions, and (c) strong affinity of polar TiO_2 to polysulfide anions *via* hydrophilic Ti–O groups and surface hydroxyl groups (B. E. = 2.1–3.6 eV).

Nazar *et al.* proposed that the nature of interactions between polysulfide anions and metal oxides is strongly governed by their redox potential *vs.* Li/Li^+.[198] Metal oxides (*e.g.*, TiO_2; 1.5 V *vs.* Li/Li^+) with a redox potential <2 V (below the polysulfide window of 2.1 V ≤ redox potential ≤ 2.4 V) bind polysulfides through surface interactions. In contrast, metal oxides (*e.g.*, V_2O_5 = 3.4 V and MnO_2 = 3.05 V *vs.* Li/Li^+; redox mediators) with a redox potential >3 V (above the polysulfide window of 2.1 V ≤ redox potential ≤ 2.4 V) can oxidize the polysulfides to thiosulfate ($S_2O_3^{2-}$) or sulfate. The *in situ* formed thiosulfate species, *i.e.*, $[O_3S–S]^{2-}$, can potentially anchor higher order polysulfides by creating an intermediate polythionate complex $[O_3S–S–S_{k-2}–S–SO_3;\ k \geq 4]$ and simultaneously induce the formation of insoluble lower order sulfides (S^{2-}). Inspired by this work, Liu *et al.* demonstrated the prolonged cycle life of Li–S cells using novel V_2O_5-decorated CNFs (VCNFs) as the interlayer.[199] The VCNF interlayer was developed by growing V_2O_5 nanoflakes on the electrospun CNFs (made using PAN/DMF solution) with the solvothermal method. The FESEM image (Fig. 9(a)) of VCNFs showed that a 50 nm thick layer of V_2O_5 uniformly wrapped each individual CNF. The TEM image in

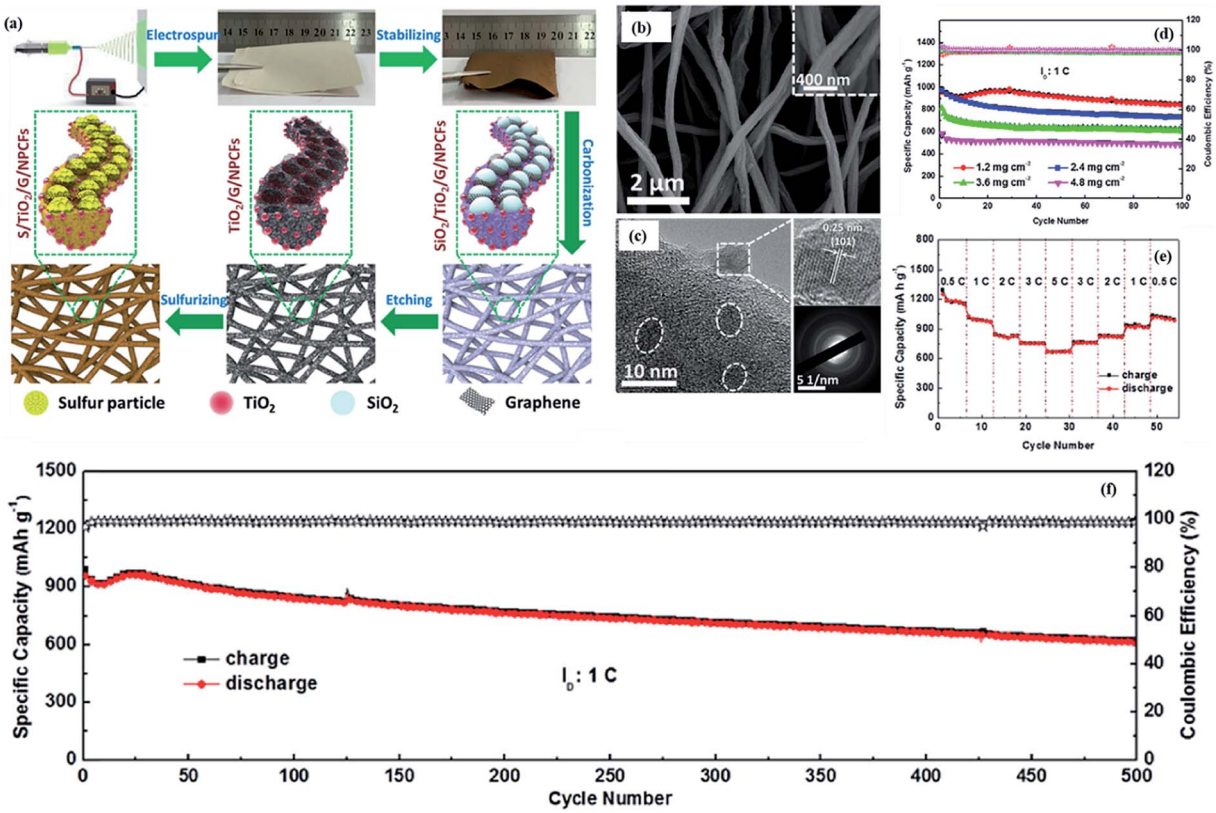

Fig. 8 (a) Schematic illustration of the fabrication process of the C/G/TiO_2–S composite, (b) SEM image of the C/G/TiO_2–S composite, and (c) HRTEM and SAED images of the C/G/TiO_2–S composite. TiO_2 nanocrystals (circled with white dotted lines) have an average size of 5 nm. The lattice fringes enlarged from the HRTEM image and the corresponding SAED pattern show that the phase of the nanoparticles is rutile TiO_2 with a polycrystalline structure. (d) Cycling performance of the C/G/TiO_2–S electrode with different sulfur contents at a current rate of 1C, (e) rate capability of the C/G/TiO_2–S electrode recorded at the current rates of 0.5C, 1C, 2C, 3C, and 5C, and (f) long-term cycling performance of the C/G/TiO_2–S electrode at 1C (reproduced with permission from ref. 204. Copyright 2017 Elsevier B.V.).

Fig. 9(d) further revealed a 1D V_2O_5 architecture with a crystalline flaky morphology homogenously distributed on every single nanofiber. The sulfur cathodes (S = 2 mg cm^{-2}) were prepared by coating a carbon–sulfur slurry (70% S, 20% super P, 10% PVDF in NMP) on carbon-coated Al-foil and drying at 60 °C for 24 h. Impressively, Li–S cells with the VCNF interlayer showed a high discharge capacity of 576 mA h g^{-1} at a 3C rate after 1000 cycles with ~70.6% retention (fading rate = 0.03% per cycle) of the initial capacity (Fig. 9(c)). In comparison, Li–S cells with a bare CNF interlayer delivered a low discharge capacity of 265 mA h g^{-1} after 1000 cycles with ~33.6% retention (fading rate = 0.06% per cycle) of the initial capacity. Furthermore, Li–S cells with VCNF interlayer exhibited excellent rate performance (up to 5C) (Fig. 9(d)) and suppressed self-discharge (Fig. 9(e and f)). The superior electrochemical performance of Li–S cells (with the VCNF interlayer) was assigned to (a) the V_2O_5 in the VCNF interlayer with a strong affinity towards polysulfides (*e.g.*, 3.73 eV for V_2O_5–Li_2S_4 interactions)[205] as well as redox-mediator function (high redox potential), (b) the robust 3D conducting VCNF architecture for re-utilization of the active material and (c) inherent interfiber macropores/voids for facile ion transfer.

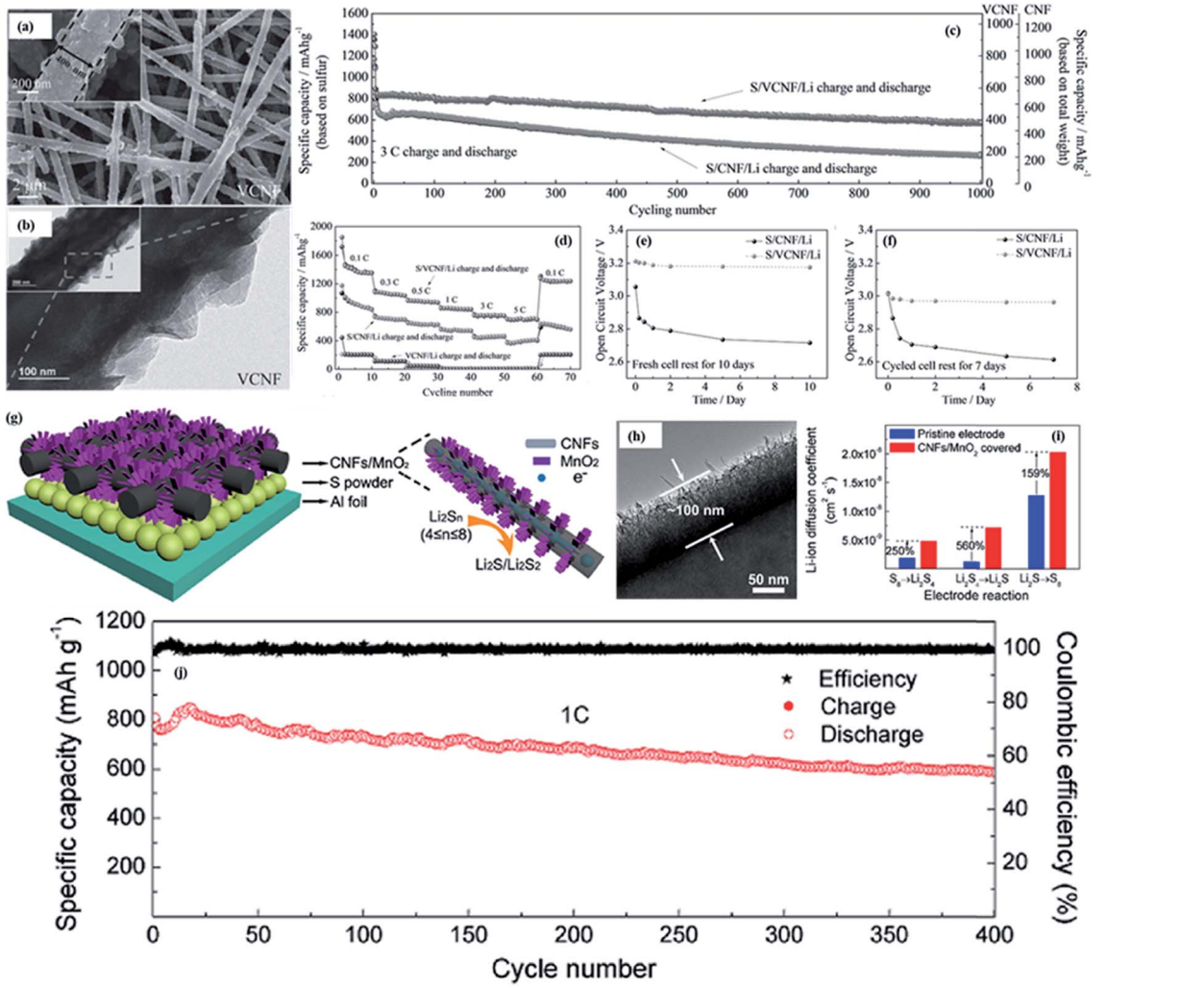

Fig. 9 (a) FESEM image of VCNFs (the high-resolution image is shown in the inset), (b) HRTEM image of VCNFs (high-resolution image is shown in the inset), (c) long term cycling performance of S/CNF/Li (bare CNF interlayer) and S/VCNF/Li (VCNF interlayer) cells at 3C, (d) rate performances of S/CNF/Li, S/VCNF/Li, and VCNF/Li (without S cathodes) cells from 0.1 to 5C, (e) the open-circuit voltage of S/CNF/Li and S/VCNF/Li fresh cells during original storage. The initial OCV of the S/VCNF/Li fresh cell (3.22 V) is higher than that of the S/CNF/Li one (3.06 V), and remains rather stable in the subsequent 10 days with a final cut-off voltage of 3.18 V. The highly stable OCV of the S/VCNF/Li fresh cell is associated with the formation and immobilization of polysulfides in the cathode. (f) The open-circuit voltage of S/CNF/Li and S/VCNF/Li cycled cells during interrupt storage. S/CNF/Li and S/VCNF/Li cells were charged back to 3.0 V after 100 cycles and stored for seven days and again cycled. During the whole interrupt rest for S/VCNF/Li, OCV values are above 2.96 V, which is similar to the fresh cell thus corroborating a suppressed self-discharge due to the VCNF interlayer. (Reproduced with permission from ref. 199. Copyright 2017 Elsevier B.V.); (g) schematic illustration of the Li–S battery with a sulfur cathode covered with the CNFs/MnO_2 composite, (h) TEM image of the CNFs/MnO_2 composite. The dense MnO_2 nanosheets were radially grown on the surface of CNFs to a thickness about 100 nm. (i) Calculated diffusion coefficient of lithium ions for the CNFs/MnO_2 composite covered S-electrode and the pristine S-electrode, and (j) long-term cycling performance and the coulombic efficiency at a current density of 1C for the CNFs/MnO_2 composite covered S-electrode (reproduced with permission from ref. 201. Copyright 2018 Elsevier Ltd.).

Similarly, Liu *et al.* developed CNF/birnessite-MnO_2 (CNF/MnO_2) composite electrodes using electrospinning and used it as a sulfur host in a Li–S battery.[201] A schematic illustration of the Li–S battery with a sulfur cathode covered with the CNFs/MnO_2 composite is shown in Fig. 9(g). The CNF/MnO_2 electrodes were prepared by soaking CNFs (carbonized PAN nanofibers) in aqueous $KMnO_4$ solution at room temperature for 48 h and then drying at 60 °C under vacuum. Here, the room temperature growth of MnO_2 was governed by the redox reaction between MnO_4^- and C ($4MnO_4^- + 3C + 4H^+ \rightarrow 4MnO_2 + 3CO_2 + 2H_2O$). The TEM image in Fig. 9(h) exhibited the dense MnO_2 nanosheets radially grown on the surface of the CNFs to a thickness about 100 nm. The CNF/MnO_2–S cathodes were prepared using commercial sublimated sulfur and cast on Al foil. The Li–S cell with the CNF/MnO_2–S cathode (1.5 mg cm^{-2} S) delivered a high initial capacity of ~788 mA h g^{-1} at 1C (coulombic efficiency ≥ 99%) with ~75% retention after 400 cycles exhibiting a slow decay rate of 0.063% per cycle (Fig. 9(j)).

In this composite, nano-textured MnO_2 anchored on CNFs was shown to improve the kinetics for the conversion of soluble Li_2S_4 to insoluble Li_2S_2/Li_2S. More specifically, the diffusion coefficient of Li^+ for the CNF/MnO_2 cathode during $Li_2S_4 \rightarrow Li_2S$ conversion was greatly enhanced (~560%) compared to that for the pristine cathode (without CNF/MnO_2) (Fig. 9(i)). Therefore, the MnO_2 component in the composite cathode serves as a bifunctional agent, which not only entraps polysulfides within the cathode through polythionate complex formation but also promotes reduction kinetics.

Non-stoichiometric metal oxide based heterostructures. Recently, reduced forms of TiO_2 such as titanium suboxides (*e.g.*, Ti_4O_7 with two Ti^{4+} (3 d^0) and two Ti^{3+} (3 d^1)), and titanium monoxide (TiO with Ti^{2+} (3 d^2)) have been employed as sulfur hosts and interlayers in Li–S batteries.[206–209] The use of such bifunctional oxides in Li–S batteries brings about two main advantages: (i) substantial improvement in the electrical and ionic conductivity due to oxygen vacancies in the Ti and O sublattices and (ii) strong binding of polysulfide anions (S_k^{2-}, Lewis base) with unsaturated Ti-centers (vacant d-orbital, Lewis acid) through Lewis acid–base (*i.e.*, covalent coordination) type interactions (B. E. ≥3.5 eV).[114,207,210] Nevertheless, the preparation of these Ti oxides (*via* carbothermal reaction or reducing H_2 gas) requires a high temperature (usually >800 °C) treatment, resulting in highly dense materials (low surface area) with irregular particulates.[211] Consequently, these dense Ti oxides show a compromised performance in Li–S batteries due to their reduced host–polysulfide interfacial (interaction) area. There are few reports on the development of sophisticated architectures (*e.g.*, hollow TiO/C microspheres) of these Ti oxides with a high surface area.[207,208] However, the complicated synthesis route adopted to design such novel architectures is impractical on a large scale. Furthermore, these powder based Ti oxides are used in a slurry form with additional inactive elements (binders and conducting additives), which results in a low sulfur loading in the final cathode.[207–209] In this view, the combination of electrospinning and carbothermal processes provides a simple, cost-effective approach for the development of free-standing Ti-oxide electrodes without the need for a complicated synthesis route. For example, Tang *et al.* recently developed a carbon/Ti_4O_7 non-woven fabric through electrospinning and used as a multifunctional interlayer in a Li–S battery.[212] The free-standing C/Ti_4O_7 mat was prepared by electrospinning a solution of PVP/TIP in ethyl alcohol and calcining at 1100 °C under a steady N_2 flow. The TEM image of C/Ti_4O_7 showed that Ti_4O_7 nanoparticles were tightly surrounded by a thin layer of carbon in a bamboo-like shape as given in Fig. 10(a).

The Li–S cells based on S-cathodes (63 wt% and 1.5 mg cm^{-2} S in the final cathode) and the C/Ti_4O_7 interlayer exhibited superior electrochemical performance to those fabricated with a bare C interlayer. More specifically, Li–S cells with the C/Ti_4O_7 interlayer delivered a high initial discharge capacity (~1046 mA h g^{-1} at 2C rate), excellent rate capability (capacities of ~721, 710 and 648 mA h g^{-1} at 1C, 2C and 4C, respectively after 200 cycles as given in Fig. 10(b)), and long cycle life (~562 mA h g^{-1} at 2C even after 500 cycles as given in Fig. 10(c)). The Ti_4O_7 suboxide is one of the Magneli phases (Ti_nO_{2n-1}; $4 \leq n \leq 9$) of Ti with two equally populated Ti^{4+} (d^0) and Ti^{3+} (d^1) states, high conductivity and ~62.5% unsaturated Ti centers (Ti_{5c} and Ti_{4c}) on the surface.[198,207,208,213] These unsaturated Ti centers with a vacant d orbital (Lewis acid) serve as strong anchoring sites for polysulfide anions (Lewis base due to lone pair electrons of the terminal S) and hold them through reversible coordinate covalent S ← Ti bonding (so-called 'Lewis acid–base interaction').[198,207,208] Furthermore, an ensemble of these unsaturated Ti centers in Ti_4O_7 (every 4th edge-shared TiO_6 octahedron is shearing due to the reduction of Ti and O vacancies) are arranged in the step sites and readily available to polysulfide anions for chemical interactions.[198,207,208] Therefore, the conducting C/Ti_4O_7 interlayer can alleviate the polysulfide shuttle, and catalytically re-activate the deposited active materials in a working Li–S cell. All these features of the C/Ti_4O_7 interlayer thus enabled Li–S cells to achieve excellent performance.

Recent theoretical predictions indicated that surface defects and coordination of the terminated Ti atoms play a decisive role in the binding capability/energy of these Ti oxides with polysulfides.[210] According to DFT calculations, surface Ti_{5c} (5 coordination) atoms have a higher affinity towards polysulfide anions than Ti_{6c} atoms.[210,214] Hence, TiO could be more effective in Li–S batteries than Magneli Ti_4O_7 (with 37–38% Ti atoms as Ti_{6c}) and TiO_2 (with 50% Ti atoms as Ti_{6c}) since all (100%) the surface Ti atoms in TiO have either a Ti_{5c} or a Ti_{4c} coordination number.[209,214] Therefore, our group (Singh *et al.*) recently designed free-standing mats of TiO/CNFs (surface area 427 m^2 g^{-1}) through electrospinning of hybrid TIP/PVP gel in binary ethanol/acetic acid solvents and used them as a sulfur host in a Li–S battery.[79] The SEM image revealed that the fibrous structures of the TiO/CNF sample were coarser with TiO nanoparticles protruding from the surface of nanofibers (Fig. 10(d)). The TiO/CNF–S cathodes (S = ~2 mg cm^{-2}; ~50 wt%) fabricated with the rapid sulfur melt infiltration (heat-pressing at 140 °C for 5 s at a pressure ≤ 250 psi) technique developed in our lab[215] delivered high initial discharge capacities of ~1080, ~975, and ~791 mA h g^{-1} at C/10, C/5, and C/2 rates, respectively (Fig. 10(e)). After an initial capacity drop within a few cycles (probably due to redistribution/activation of the elemental

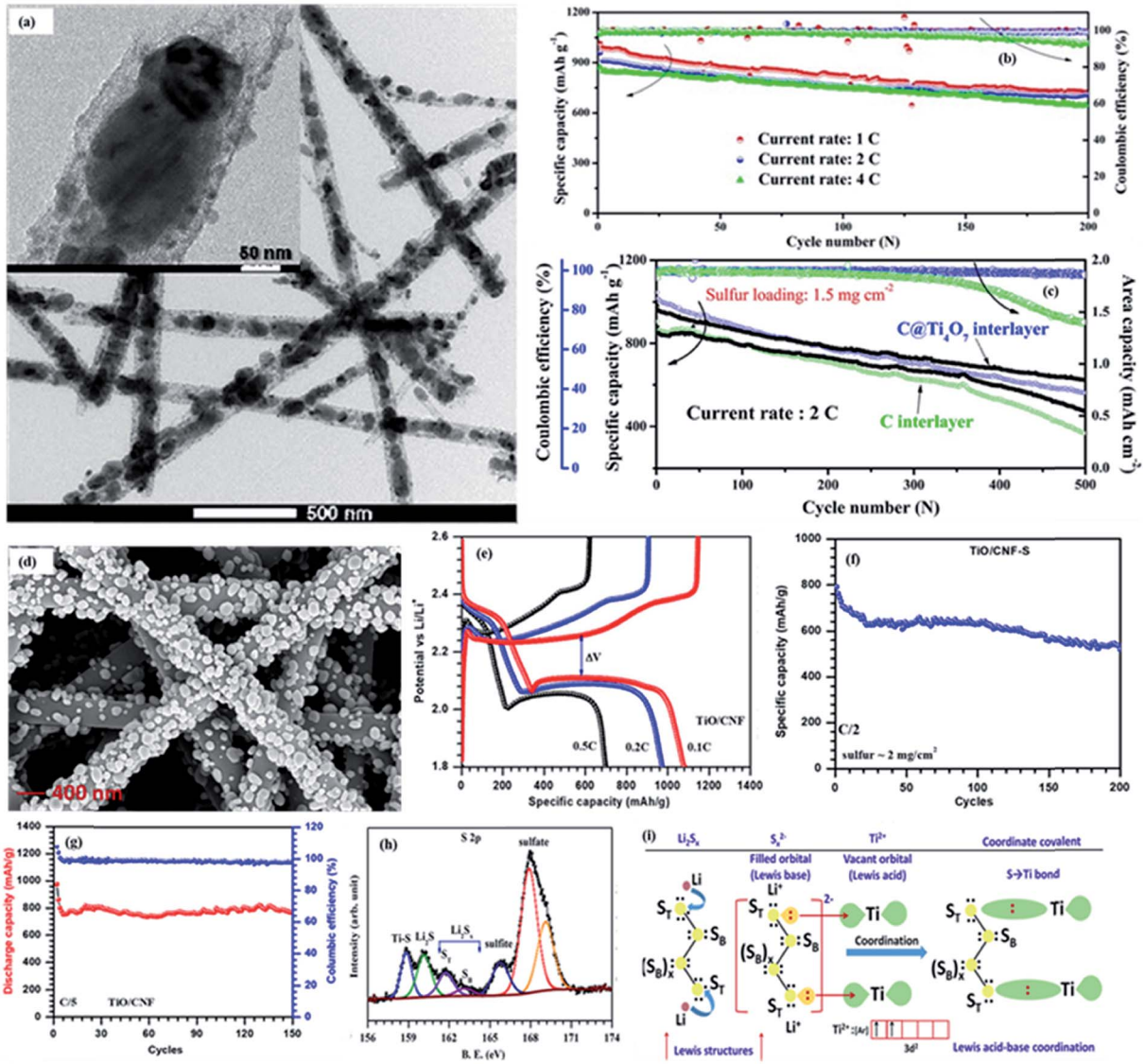

Fig. 10 (a) TEM image of C/Ti_4O_7 nanofibers (the high-resolution image is shown in the inset), (b) high rate cycle performance of C/Ti_4O_7 interlayer cells with a 0.2 M $LiNO_3$ additive, and (c) long term cycle life of C/Ti_4O_7 interlayer cells and C interlayer cells at 2C (reproduced with permission from ref. 212. Copyright 2018 Elsevier Ltd.); (d) SEM image of TiO/CNF nanofibers, (e) first galvanostatic charge–discharge curve of TiO/CNF–S cathodes at different C-rates, (f and g) cyclic stability test of TiO/CNF–S cathodes at C/2 and C/5 rates over 200 and 150 cycles, respectively, and (h and i) core-level S 2p of the cycled TiO/CNF–S cathode and a schematic explaining the Ti ← S bond formation through coordination between unsaturated Ti centers (Lewis acid) and terminal S (S_T) of polysulfides (reproduced with permission from ref. 79. Copyright 2018 American Chemical Society).

sulfur), TiO/CNF–S cathodes showed stable cycling and retained a capacity of ~787 mA h g^{-1} (C/5) and 518 mA h g^{-1} (C/2) over 150 and 200 cycles, respectively (Fig. 10(f and g)). With the post-mortem XRD and XPS (S 2p XPS spectra are given in Fig. 10(h)) measurements, we confirmed the presence of a reversible coordinate covalent Ti ← S bond between TiO ($3d^2$) and polysulfide (S_k^{2-}) anions. A schematic explaining the Ti ← S bond formation through coordination between unsaturated Ti centers (Lewis acid) and terminal S (S_T) of polysulfides is given in Fig. 10(i). The high electrical conductivity (1.1 S cm^{-1}) and strong polysulfide binding ability of TiO/CNFs allowed Li–S cells to show good performance at 2 mg cm^{-2} sulfur loading.

Heterostructures with catalytic functionality. In Li–S batteries, the slow reduction of lithium polysulfides to insoluble Li_2S_2/Li_2S is the leading cause for the shuttle effect, which eventually leads to a low coulombic efficiency and a short cycle life.[214] Therefore, an ideal sulfur host is desired to have not only a firm binding with polysulfides but also the ability to promote polysulfides to Li_2S/Li_2S_2 conversion (catalytic function).[191,214] In this context, the use of catalytic materials including transition metals and their carbides, nitrides, and sulfides is promising.[191,196,214,216] These materials not only exhibit high polysulfide-anchoring ability through chemical interactions (long cycling stability) but also show a strong catalytic function

for the conversion of polysulfides to Li_2S_2/Li_2S (fast kinetics and high capacity).[214,216] There are quite a few reports on the use of such catalytic materials (*e.g.*, TiN, TiC, CoS_2, and VN) in Li–S batteries aiming at high capacity and long cycle life.[195,214,217–222] Nevertheless, in most of the studies, these materials are usually present as large crystallites, which eventually offer a reduced number of active sites for polysulfide interactions and catalytic function. Furthermore, a multi-step synthesis process is generally required to develop these materials for their productive use in Li–S batteries. In this context, the electrospinning technique could offer a simple and economical approach for the fabrication of heterostructures of metal carbides, sulfides, and nitrides with controllable crystallite size. At present, the development of heterostructures of these materials through the electrospinning technique is still in its nascent stage. Recently, Shang *et al.* developed free-standing N-doped CNF/β-Mo_2C (NCNF–Mo_2C) electrodes by electrospinning a solution of PAN/molybdenum acetylacetonate dioxide in DMF solvent and used them as a 3D current collector in Li–S batteries.[193] The annealed NCNF–Mo_2C preserved the interconnected 3D framework structure with long and straight nanofibers as shown in Fig. 11(a). The HRTEM image in Fig. 11(b) confirmed the tight loading of ultrafine Mo_2C nanostructures (2–10 nm) without aggregation onto the nanofiber. The energy-dispersive X-ray spectroscopy (EDS) mapping evidenced that constituent C, Mo and N elements possessed a correlated spatial distribution (Fig. 11(c)). The electrochemical performance was tested using a 1 M Li_2S_6 catholyte (as an active material; corresponds to 2 mg S) and an ethereal electrolyte. The NCNF–Mo_2C based Li–S cells delivered a high capacity of 1086 mA h g^{-1} at a C/5 rate (after initial activation cycles), excellent rate performance up to 1C (750 mA h g^{-1}), high coulombic efficiency (~100%) and prolonged cycling over 275 cycles at C/5 without apparent capacity fading (retention ~ 100%) (Fig. 11(d)).

Moreover, the NCNF–Mo_2C electrode showed a relatively lower polarization (ΔE, the difference between oxidation and reduction potentials) and lower overpotential (energy barrier for $Li_2S \rightarrow S_k^{2-}$ ($k \geq 4$) conversion during the charge process) than that of bare NCNFs (without Mo_2C), which indicates its catalytic functionality (Fig. 11(e)). Here, hexagonal β-Mo_2C with high electrical conductivity (~10^2 S cm^{-1}) served as a polar metallic substrate offering a strong affinity towards polysulfides and enhancing transformation between soluble polysulfides and insoluble solid-state products, *viz.*, S and Li_2S_2/Li_2S. Using DFT calculations, the authors also show that a much stronger Mo–S type chemical bonding (B. E. = 3.83 eV) is present between Mo of Mo_2C (101) and S of Li_2S_6 (Fig. 11(f)). Therefore, the free-standing NCNF–Mo_2C electrode has a 'positive' catalytic effect and strong affinity to polysulfides, which eventually led to an outstanding electrochemical performance in Li–S cells.

Recently, some approaches have also been dedicated to modifying commercial separators with functional materials (for conductivity and polysulfide binding) in order to alleviate the polysulfide shuttle and protect the Li-anode in Li–S batteries.[223,224] A thin layer of functional material on separators allows reducing the weight/volume fraction occupied by these inactive materials without sacrificing their activity, which is essential for the high energy density of Li–S batteries.[223] Various materials including metal oxides, polymers, and functionalized carbon have been used as an ion-sieving layer on separators to improve the performance of Li–S batteries.[159,173,174,223–226] However, it is still critical to develop lightweight, thin coating layers (on the cathode side) of these multifunctional materials on separators while retaining fast Li-ion diffusion, especially with nanoparticles due to aggregation during the slurry-cast process.[226] In this regard, Chen *et al.* proposed the use of electrospun cobalt, nitrogen co-doped porous CNF/reduced graphene oxide (Co–N–CNF/rGO) as a thin layer on a commercial PP (polypropylene) separator in Li–S batteries.[225] First, mesoporous Co–N–CNF nanofibers (a surface area ~470 m^2 g^{-1}, pore volume ~0.439 cm^3 g^{-1}, and average pore diameter ~3.5 nm) were fabricated by electrospinning a solution of PAN, SiO_2 (template), and Co precursor followed by carbonization (800 °C, 2 h, argon flow) and template removal with NaOH. The TEM results showed that ultrafine Co nanoparticles (average size ~24 nm) were dispersed uniformly in the nanofibers (Fig. 11(g)). EDS mapping further showed a homogeneous distribution of Co, N and C elements along the whole nanofiber (Fig. 11(g)). In addition, many crooked graphitic lattice fringes were clearly observed on the edge of metallic Co (Fig. 11(h)), suggesting that metallic Co was wrapped by graphitic carbon through a self-assembly approach. A dispersion of Co–N–CNF and rGO (in ethanol) was then deposited on a PP separator by vacuum filtration to get a ~6 μm thick (0.083 mg cm^{-2}) coating of the Co–N–CNF/rGO composite. The electrochemical performance was evaluated using a slurry based S-cathode (~63 wt%, 1.2 mg cm^{-2} S in the final cathode) and an ethereal (LiTFSI in DME : DOL) electrolyte. The Li–S cell based on the modified (with Co–N–CNF/rGO) PP separator delivered a high capacity of ~1344 mA h g^{-1} at C/10, high rate capability (~659 mA h g^{-1} at 5C) (Fig. 11(j)), excellent cycling stability (~71.2% retention of the initial capacity of ~865 mA h g^{-1} at C/2 over 500 cycles) (Fig. 11(i)) and high coulombic efficiency (~100%). Here, the rGO not only served as a blocking (physical/chemical) layer for polysulfides but also helped to construct a stable film on the separator. The N–CNF component forms a 3D conducting network, which improves the electrolyte wettability of the separator and ensures easy Li^+ transport and hence guarantees high rate performance. The contact angle results displayed that the ethereal electrolyte thoroughly wets the modified separator within 2 s, much better than the bare PP separator (contact angle ~ 19.63°) (Fig. 11(k)). Furthermore, the ultrafine metallic Co nanoparticles in nanofibers improve the sulfur utilization (due to conductivity) and redox kinetics (due to catalytic functionality), thus giving rise to excellent cycling stability and high coulombic efficiency.

In summary, confining the lithium polysulfides through strong chemical interactions (Lewis acid–base or polythionate type) along with improving the redox kinetics is critical to achieving a remarkable electrochemical performance in Li–S batteries. Undoubtedly, the electrospun heterostructures of transition metals and their oxides, and carbides have shown great potential in this context and played a significant role in

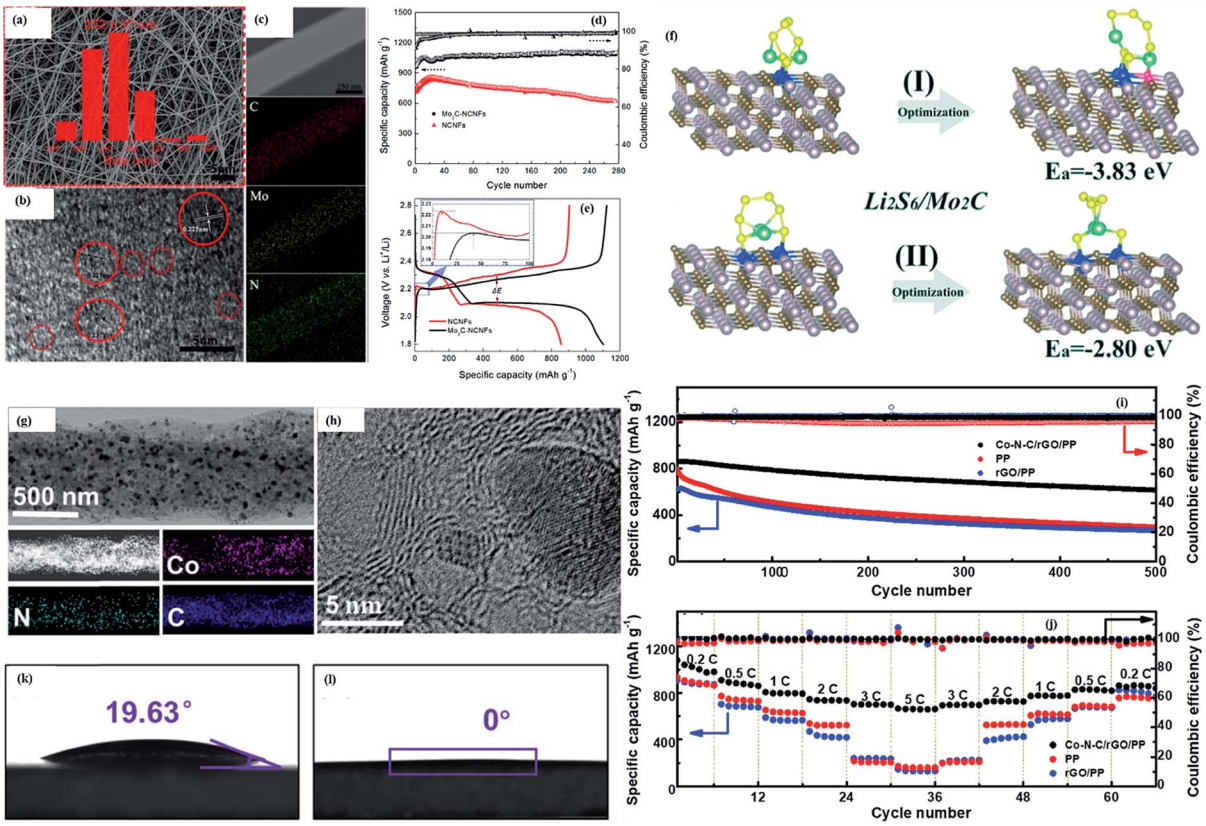

Fig. 11 (a and b) SEM and TEM images of NCNFs-Mo_2C, respectively (nanofibers display an average diameter of 252 ± 37 nm as shown in the inset of (a)), (c) SEM image and corresponding EDS elemental mapping of NCNFs-Mo_2C, (d) cycling stability and coulombic efficiency of NCNFs-Mo_2C and NCNF based Li–S cells, (e) galvanostatic charge–discharge voltage profiles of the stable cycle at 0.2 C and selected charge profiles (inset) of NCNFs-Mo_2C and NCNF based Li–S cells, and (f) DFT results of two stable binding configurations of Li_2S_6 with a single layer of Mo_2C (101) with a calculated binding energy of (I) −3.83 eV and (II) −2.8 eV. (Reproduced with permission from ref. 193. Copyright 2018 Published by Elsevier B.V.); (g) TEM and EDS mapping of Co–N–CNFs, (h) high-resolution TEM image of the Co–N–CNFs, (i and j) cycling stability and rate capability of the cells with different separators over 500 cycles at 0.5C, respectively and (k and l) contact angle photographs of PP and Co–N–CNFs/rGO/PP separators using a liquid electrolyte (reproduced with permission from ref. 225. Copyright 2017 Elsevier B.V.).

the recent advancement of Li–S batteries. However, there is lot more room for improvement by (i) designing these materials with different crystalline phases, lattice orientations, and oxidation states (of metal), (ii) rationalizing their textural properties using templates for optimal active sites, and (iii) reducing their mass/volume fraction in the final cathode. In this view, the electrospinning technique is versatile, which could offer a simple, inexpensive and industry viable synthesis approach to bring about these abovementioned features into a single material. In the following sections, we will now review recent advances made in other sulfur batteries (*e.g.*, Na–S) and metal–selenium batteries using electrospun materials.

3.2 Electrospun nanostructures for RT Na–S batteries

The low cost and natural abundance of the sodium element has stimulated research on Na–S batteries beyond the analogous Li-systems.[227] High-temperature (300–350 °C) Na–S technologies, with a molten Na-electrode and a solid β-Al_2O_3 electrolyte, are now commercially available.[93,228,229] However, the highly corrosive nature of molten Na imposes severe safety and maintenance challenges and demands the use of expensive highly alloyed steels.[90,93] Therefore, high cost and high-temperature operation impede their use in EVs.[90,230] Room-temperature (RT) Na–S batteries are cost-effective and much safer and thus desirable for use in large stationary grids and EVs.[90,231] Therefore, research on the development of high-performance RT Na–S is currently predominant. A RT Na–S cell comprises a sulfur cathode, suitable electrolyte (ethereal or carbonate based), separator and Na metal as the anode. In RT Na–S cells, S is electrochemically reduced to Na_2S during discharge through soluble intermediates (Na_2S_k; $k \geq 4$), which is analogous to Li–S batteries (Fig. 2(a)).[90,227,231] Therefore, RT Na–S batteries also face all the common intrinsic challenges of a Li–S system including low sulfur utilization, volume expansion, and the ill-famed shuttle effect (Fig. 2(b–d)).[90,231–233] Over the last few years, a range of similar conventional approaches (used for Li–S systems) have been applied to cope with such issues by designing novel porous and conducting host materials for sulfur, employing sodium polysulfides (catholytes) or sulfurized PAN as active materials, passivating the Na anode, and modifying/coating separators with functional materials (*e.g.*, Nafion).[94,233–242] However, the reported electrochemical

performances are not satisfactory because the electrochemistry of RT Na–S cells is even more challenging regarding sulfur utilization due to the large size of Na^+ ions[90] and volume change (*i.e.*, pulverization) during sodiation (S → Na_2S; ~260%),[90,231] which lead to low reversible capacity and rapid capacity fade during cycling. As mentioned earlier, electrospinning is a straightforward, cost-effective and industry-viable approach, which offers flexibility in designing materials with tunable textural properties for accommodation of S and volume changes and surface activity for alleviation of the shuttle effect. Therefore, recent studies have been inclined towards the development of rationally engineered novel electrospun nanostructures for RT Na–S batteries.[243–246] However, in this section, we will only focus on some representative examples of these nanostructures, which have produced exceptional electrochemical performance in RT Na–S batteries. For example, Xia *et al.* recently reported the controllable fabrication of carbon hollow nanobubbles on N- and O-co-doped porous carbon nanofibers (CHNBs@PCNF) as a sulfur host for RT Na–S batteries (Fig. 12(a)).[107] The CHNBs@PCNF electrodes (surface area = 420 m^2 g^{-1}; pore volume = 1.64 cm^3 g^{-1}) were prepared by electrospinning a solution of PVA/LiN_3 in water followed by drying at 75 °C under dynamic vacuum and calcination at 650 °C for 3 h under a N_2 environment. Before calcination, the as-spun LiN_3/PVA nanofibers were stabilized at 240 °C for 2 h with slow heating (0.5–1.0 °C per minute) under a nitrogen environment. The slow stabilization could blow up the PVA through gentle N_2 desorption ($6LiN_3 \rightarrow 2Li_3N + 8N_2$), leading to the formation of CHNBs on the CNF. The CHNBs@PCNF was finally washed with hydrochloric acid (HCl) to remove residual impurities (*e.g.*, Li_2CO_3) and dried. The TGA results further showed that LiN_3 also served as a source of the N-dopant into the CNF. The SEM image in Fig. 12(b) showed that a plethora of nanobubbles with diameters between 10 and 60 nm were uniformly and densely distributed on the surfaces of the as-prepared CHNBs@PCNF. The TEM image further confirmed that these carbon nanobubbles were hollow and that the shells were very thin, with a thickness of only ~2 nm (Fig. 12(c)). The S/CHNBs@PCNF cathodes (~57 wt%, 1.4 mg cm^{-2} S in the final cathode) were prepared by a facile melt-infiltration method (155 °C/12 h). The electrochemical tests were conducted in a carbonate-based electrolyte (1 M sodium perchlorate ($NaClO_4$) in EC/PC, 1 : 1 v/v% with the addition of 5 wt% fluoroethylene carbonate (FEC)) within the 1.2–2.8 V potential range (*vs.* Na/Na^+). The S/CHNBs@PCNF cathode delivered an initial discharge capacity of ~1214 mA h g^{-1} at a C/10 rate, good cycling stability with ~65% capacity retention over 50 cycles and excellent rate performance up to 2C (~302 mA h g^{-1}), exceeding those Na–S cells fabricated with the control S/CNF cathode. Furthermore, the S/CHNBs@PCNF cathodes displayed long-term cycling over 400 cycles at 2C with a low capacity fading rate (0.044% per cycle) as given in Fig. 12(d).

The excellent electrochemical performance of the S/CHNBs@PCNF cathode was attributed to the various unique features of electrospun CHNBs@PCNF structures. The CHNBs on PCNFs effectively facilitated the wettability of the electrode and accommodated the volume changes during cycling. The 1D robust PCNF structures ensured continuous electron supply during oxidation/reduction reactions and mechanical integrity of the cathode. The N and O functionalities led to adsorption and trapping of sodium polysulfides and alleviated the shuttle effect. Using DFT calculations, the authors showed that the lone pair electrons of N and O atoms in the C lattice directly interacted with the terminal Na of the sodium polysulfides (Na_2S_k) and suppressed their dissolution and shuttling (Fig. 12(e)). All these features allowed S/CHNBs@PCNF cathodes to show excellent reversible capacity, high rate capability, and long cycle life.

As seen in Li–S batteries, polar metal oxides could strongly bind intermediate polysulfides through chemical interactions and immobilize them on the cathode side. With inspiration from these approaches, Ma *et al.* recently reported a new strategy for developing ultrastable RT Na–S batteries based on S/$BaTiO_3$–C–TiO_2 (CSB@TiO_2) composite cathodes.[247] First, they developed $BaTiO_3$ (BTO, ~3 wt%) encapsulated porous CNFs (CB) by electrospinning a solution of PAN/triblock copolymer F127/$BaTiO_3$ in DMF solvent and subsequently stabilizing (280 °C for 4 h; air) and carbonizing (900 °C for 6 h; N_2) the as-spun nanofibers. Here, the F127 copolymer not only served as a surfactant for uniform dispersion of $BaTiO_3$ into CNFs but also acted as a soft template for pore formation (surface area of CB = 589 m^2 g^{-1}; pore sizes 1–3 nm). Then, the CSB cathodes were prepared using the sulfur melt-infiltration method (160 °C, 10 h). Finally, a protection layer of amorphous TiO_2 (~4 nm thick) was directly grown on the free-standing CSB cathodes with the help of the atomic layer deposition (ALD) technique to get free-standing, binder-free CSB@TiO_2 cathodes (60 wt%, 1.2–1.4 mg cm^{-2} S in the final cathode). A schematic illustration of the CSB@TiO_2 electrode preparation process is shown in Fig. 12(f). The TEM image in Fig. 12(g) showed ≈4 nm thick nanolayer of TiO_2 grown on the surface of the nanofibers. Two control samples *viz.*, C/S and C/S/BTO with a similar S loading were also prepared for comparison. The electrochemical measurements were conducted using 1 M $NaClO_4$ in a binary EC : DEC (1 : 1 v/v) solvent. The CSB@TiO_2 cathodes displayed a high discharge capacity of ~592 mA h g^{-1} (2^{nd} cycle) at 0.5 A g^{-1}, better rate capability up to 2 A g^{-1} (~350 mA h g^{-1}) and superior cycling performance (~611 mA h g^{-1} at 0.5 A g^{-1} after 400 cycles) as compared to the other two (C/S and C/S/BTO) cathodes (Fig. 12(h and i)). It is noteworthy that CSB@TiO_2 cathodes exhibited a capacity of ~525 mA h g^{-1} after 1400 cycles at 1 A g^{-1} (Fig. 12(j)) and ~382 mA h g^{-1} at 2 A g^{-1} after 3000 cycles. The remarkable electrochemical performance of CSB@TiO_2 cathodes was a consequence of various favorable aspects present in the electrospun/ALD based CB@TiO_2 structures as summarized below:

(i) The electrospun 3D architecture of porous CNFs facilitated the sulfur utilization and redox reactions *via* inherent electronic (conducting CNFs) and ionic (inter-fiber macropores) channels.

(ii) The ferroelectric (BTO, ~3 wt%) additive further improved the surface affinity of CNFs towards intermediate sodium polysulfides (Na_2S_k). $BaTiO_3$ (BTO) is a ferroelectric material, which has a spontaneous electrical polarization (induced dipole

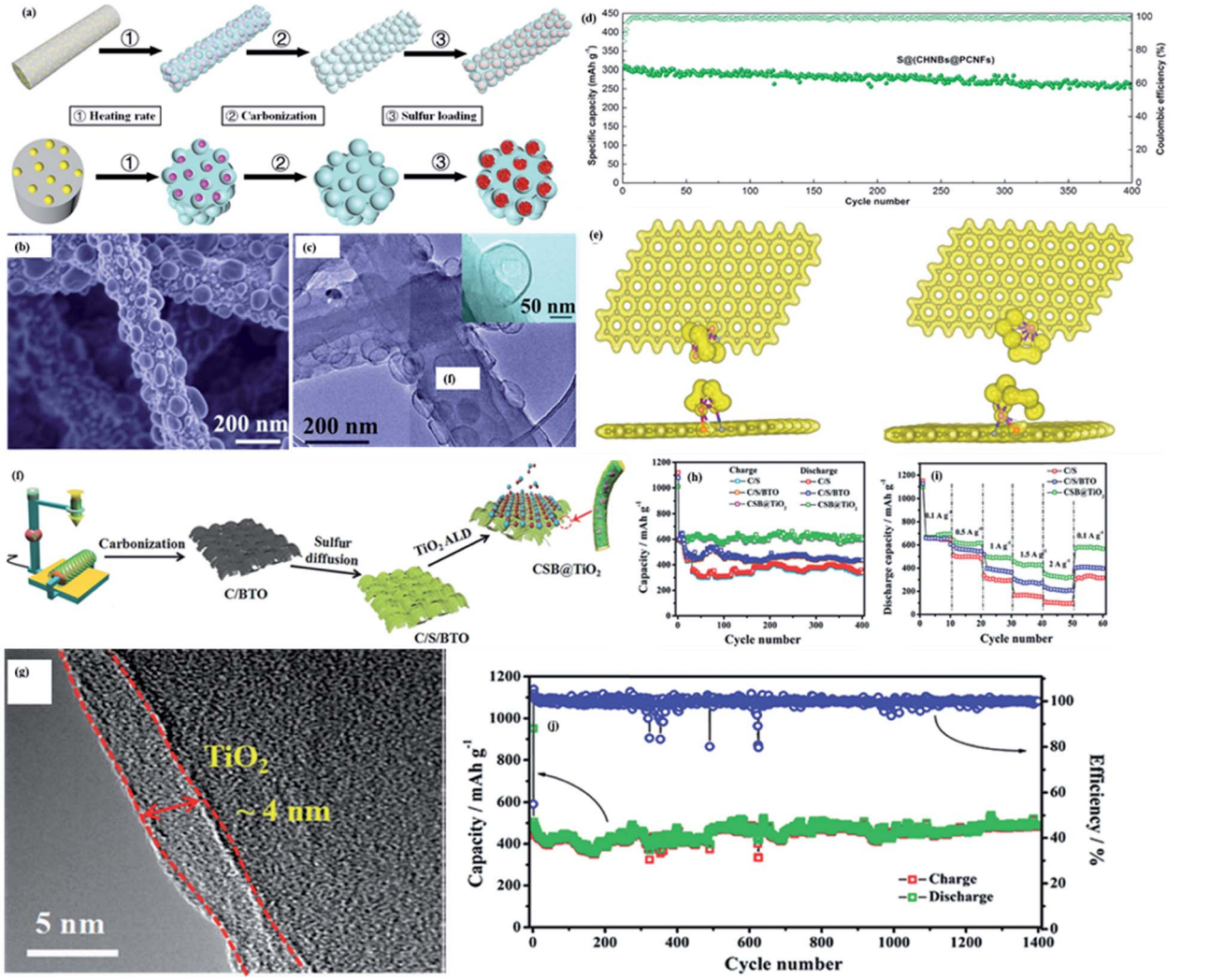

Fig. 12 (a) Schematic illustration of the preparation of S/CHNBs@PCNF cathodes for room temperature Na–S batteries. Yellow, pink, and red balls represent LiN_3, Li_3N, and S particles, respectively, (b) SEM images of CHNBs@PCNFs after calcination of the as-electrospun PVA–LiN_3 nanofibers, (c) TEM image of the as-synthesized CHNBs@PCNFs (the high-resolution image is shown in the inset), (d) cycling performance of Li–S cells based on the S/CHNBs@PCNF cathodes at a current density of 2 C, and (e) atom positions and charge density plot of Na_2S_4 (left) and Na_2S_6 (right) molecular interaction with N, O-codoped carbon. Grey, white, blue, yellow, purple, and red balls represent C, H, N, S, Na, and O atoms, respectively. (Reproduced with permission from ref. 107. Copyright 2018 Published by Elsevier B.V.); (f) schematic illustration of the CSB@TiO_2 electrode preparation process, (g) TEM image of the CSB@TiO_2 nanofiber, (h) cycling performance of C/S, C/S/BTO, and CSB@TiO_2 electrodes at 0.5 A g^{-1}, (i) rate capability of C/S, C/S/BTO, and CSB@TiO_2 electrodes at varied current densities from 0.1 to 0.5, 1, 1.5, and 2 A g^{-1}, and (j) the long-term cycling of the CSB@TiO_2 electrode after 1400 cycles at 1 A g^{-1} (reproduced with permission from ref. 247. Copyright 2018 WILEY-VCH Verlag GmbH & Co. KGaA, Weinheim.).

moment) in an electric field. Therefore, the heteropolar intermediate polysulfides could chemisorb on the spontaneously polarized BTO nanoparticles to screen these induced surface charges (internal electric field). Similar studies have been reported on the Li–S system and shown that BTO provides a stable interaction-surface for polysulfide trapping and maintains its ferroelectricity over cycling.[248]

(iii) The uniform thin layer of amorphous TiO_2 maintained the structural integrity of CSB@TiO_2 cathodes by inhibiting the pulverization of electrodes during dramatic volume changes and confined sodium polysulfides through strong polar–polar interactions.

All these features allowed CSB@TiO_2 cathodes to exhibit high capacity, excellent rate capability, and ultralong cycle life. It is noteworthy that both BTO and TiO_2 served as additives (total wt% <10%) in the CSB@TiO_2 cathodes resulting in a high sulfur content (~60 wt%) in the final cathode.

Undoubtedly, the research on the cost-effective RT Na–S technology is booming. Even though the significant progress regarding sulfur utilization and cycle life has been made in recent years using electrospun nanostructures, the RT Na–S technology is still in its nascent state. More intense research is required to improve the performance of the RT Na–S technology further under realistic conditions. The rich experience and scientific knowledge developed over the last few years in

the Li–S technology should be applied for the advancement of RT Na–S batteries. Particularly, rationally designed various electrospun heterostructures with a suitable pore size/volume and polar additives should be explored as sulfur hosts, interlayers, and electrolyte membranes to bring about significant breakthroughs in RT Na–S batteries shortly.

3.3 Electrospun nanostructures for M–S_xSe_y and M–Se batteries

Due to the semiconducting nature of elemental Se, a small amount of Se can be introduced into S molecules to improve the electrochemical activity of elemental sulfur.[51] The formed heterocyclic S-rich S_xSe_y compounds represent a new class of materials with improved conductivity (kinetics) compared to elemental S and higher theoretical capacity than elemental Se alone.[87,95,249] The preparation of S_xSe_y compounds requires a thermal treatment of the S/Se mixture at a temperature close to the melting point of Se, at which both components are reasonably miscible.[51,87] After the seminal work reported by Amine and co-workers,[48] various S_xSe_y compounds such as SeS_2, Se_2S_5, and $S_{0.94}Se_{0.06}$ with porous and conducting host materials (*e.g.*, carbon) have been explored in Li–S and RT Na–S batteries.[249–251] Inspired by the recent advances obtained using electrospun nanostructures, Yao *et al.* recently developed free-standing $S_{0.6}Se_{0.4}$@CNF composite films with sulfur atoms bonded to a carbon (C–S) lattice through a simple electrospinning technique and used them as cathodes in Li–S and RT Na–S batteries.[252] The PAN nanofibers were produced by electrospinning of a PAN/DMF solution. The $S_{0.6}Se_{0.4}$ compound was prepared by ball-milling of commercial S/Se (S/Se molar ratio = 1.5) powder for 24 h and subsequent heating at 260 °C for 12 h in a sealed autoclave. The $S_{0.6}Se_{0.4}$@CNF composite cathodes (~57.5 wt%, 0.9 mg cm^{-2} active material) were then prepared by co-heating the PAN nanofibers and $S_{0.6}Se_{0.4}$ compound at 600 °C for 6 h (3 K min^{-1}) in a sealed vessel. The scanning transmission electron microscopy (STEM) image and elemental mapping of one part of an individual $S_{0.6}Se_{0.4}$@CNF showed that the CNFs exhibited a smooth surface and S and Se were distributed uniformly all over the carbon matrix (Fig. 13(a)). The C–S stretching vibrations at 176 and 805 cm^{-1} in the Raman spectra confirmed the C–S bonding in the $S_{0.6}Se_{0.4}$@CNF cathode after co-heating $S_{0.6}Se_{0.4}$ and CNFs (Fig. 13(b)). The XRD results showed that a reaction between S (space group of *Fddd*(70)) and Se (space group of *P*3121(152)) led to the formation of $S_{0.6}Se_{0.4}$ (space group of *P*2/*c*(13)) with S–Se bonding (Fig. 13(c)). The electrochemical performance of $S_{0.6}Se_{0.4}$@CNF cathodes in Li–S cells was tested using 1 M $LiPF_6$ in ethylene carbonate–dimethyl carbonate. The electrochemical impedance analysis showed a reduced charge transfer resistance for $S_{0.6}Se_{0.4}$@CNF compared to that of S@CNF in Li–S cells indicating conductivity enhancement due to the presence of Se. The Li–S cells with the $S_{0.6}Se_{0.4}$@CNF cathode maintained a high reversible capacity of ~450 mA h g^{-1} at 0.1 A g^{-1} with ~100 coulombic efficiency and excellent rate performance (379 mA h g^{-1} at 2 A g^{-1}) (Fig. 13(d)), exceeding those of Li–S cells fabricated with S/CNF (~226 mA h g^{-1} after 100 cycles and 82 mA h g^{-1} at 2 A g^{-1}). Furthermore, the $S_{0.6}Se_{0.4}$@CNF cathode maintained a capacity of ~346 mA h g^{-1} at 1 A g^{-1} over 1000 cycles almost without capacity loss (Fig. 13(e)). Moreover, the $S_{0.6}Se_{0.4}$@CNF cathodes were also used in RT Na–S batteries using 1 M $NaClO_4$ in ethylene carbonate–polycarbonate as the electrolyte. At 0.1 A g^{-1}, the Na–S cell with the $S_{0.6}Se_{0.4}$@CNF cathode delivered a discharge capacity of ~417 mA h g^{-1} (with a coulombic efficiency close to 100%) after little capacity loss during the initial few activation cycles and retained ~90% of the initial capacity over 100 cycles (Fig. 13(f)). Moreover, at 0.5 A g^{-1}, the $S_{0.6}Se_{0.4}$@CNF cathode maintained ~70% of the initial capacity of ~290 mA h g^{-1} over 160 cycles (Fig. 13(g)). The excellent performance of the $S_{0.6}Se_{0.4}$@CNF cathode in Li–S and RT Na–S cells was attributed to (i) the introduction of Se into S, which significantly improved the sulfur utilization and suppressed the polysulfide dissolution, (ii) the formation of the C–S bond during co-heating, which helped further in alleviating the shuttle effect, and (iii) the electrospun free-standing 3D CNF architecture, which facilitated the electrolyte transport and accommodated the volume changes during reduction/oxidation reactions.

Different M–Se (M: Li, Na) chemistries have also been developed with the use of elemental Se as an active material.[95] However, similar to M–S (Fig. 2(a)), M–Se batteries also suffer from the shuttle effect and volume changes during the reduction/oxidation process (Fig. 2(c and d)).[51,87,95] Consequently, various porous nanostructures of carbon such as hollow carbon spheres,[253] heteroatom (N and O) dual-doped hierarchical porous carbon,[254] microporous carbon,[255] nitrogen-doped carbon scaffolds,[88] mesoporous graphitic carbon microspheres,[256] tube-in-tube carbon,[257] monolithic carbons,[258] graphite platelet nanofibers,[259] Co and N co-doped porous graphitic carbon,[260] and 3-D hierarchical porous tubular carbon[261] have been employed as the Se host matrix to surmount these challenges and improve the electrochemical performance of M–Se batteries.

Very recently, the use of elemental Se with various electrospun host materials have also been proposed for obtaining a promising cathode in Li–Se and RT Na–Se batteries.[262,263] Park *et al.* recently developed Se-infiltrated MOF-derived porous CNF based cathodes (Se/BP-CNF, 42 wt% Se in the final cathode) for high capacity and rate performance in Li–Se batteries (Fig. 14(a)).[264] The porous CNFs with bimodal micro/mesopores (BP-CNF, surface area = 788 m^2 g^{-1}) and enlarged pore volumes were fabricated by electrospinning a solution of ZIF-8 nanoparticles/PAN in DMF and subsequently carbonizing at 800 °C for 2 h in an Ar flow and activating with KOH. The ZIF-8 with Zn ions and organic ligands served as a template to introduce mesopores into CNFs, whereas the chemical activation with KOH helped to create micropores in the CNFs. The CNFs were etched with a hydrochloric solution to remove residual metallic Zn impurities before KOH treatment. The SEM and TEM results (Fig. 14(b and c)) showed well distributed hollow carbon nanocages within 1D BP-CNF structures originated from the removal of ZIF-8 particles and by the activation process. The Se infiltration was carried out by heating BP-CNF and Se powder together in two steps, at 260 °C for 12 h and

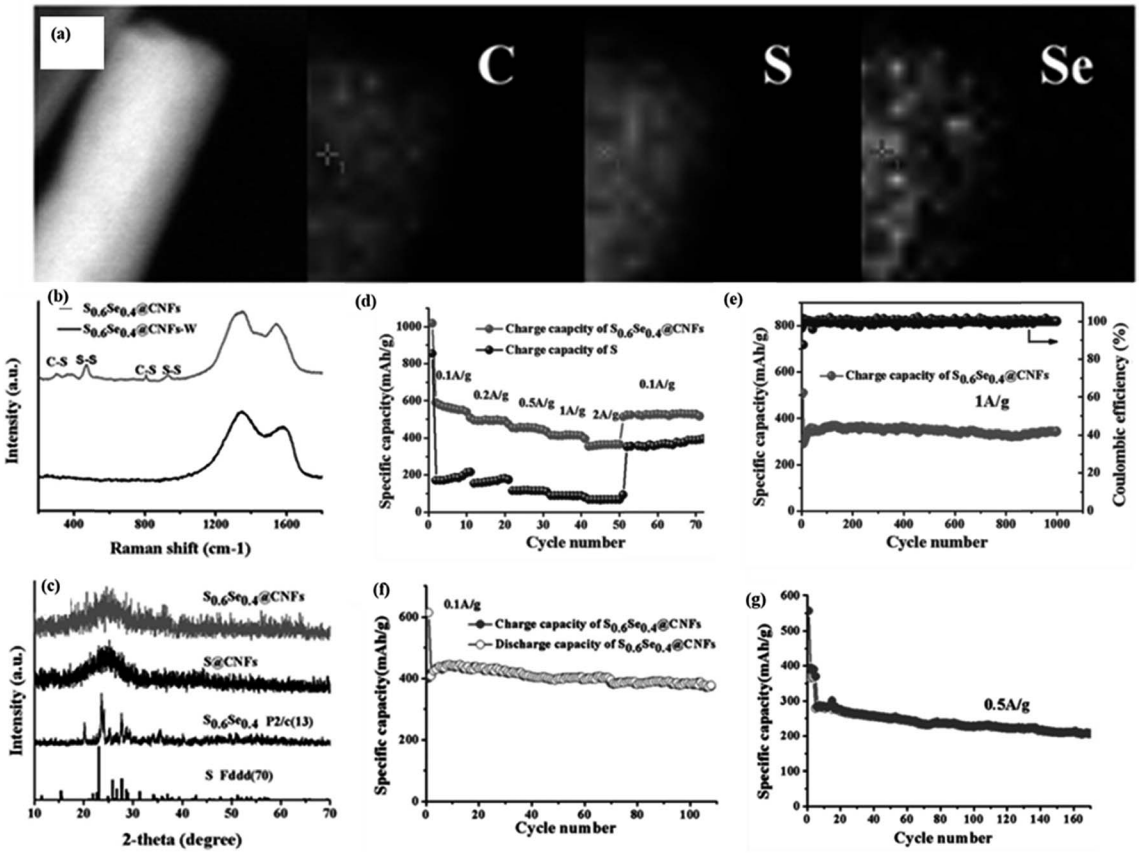

Fig. 13 (a) Scanning transmission electron microscopy (STEM) and corresponding elemental mapping (carbon, sulfur, and selenium) of one part of an individual $S_{0.6}Se_{0.4}$@CNF, (b) Raman spectrum of $S_{0.6}Se_{0.4}$@CNFs (co-heating PAN and $S_{0.6}Se_{0.4}$ compound) and $S_{0.6}Se_{0.4}$@CNFs–W. The $S_{0.6}Se_{0.4}$@CNFs–W electrode was prepared by first carbonizing PAN to CNFs and then infiltrating the $S_{0.6}Se_{0.4}$ compound in order to show that co-heating was responsible for C–S formation, (c) XRD patterns of $S_{0.6}Se_{0.4}$@CNFs and S@CNFs, (d) rate performance of $S_{0.6}Se_{0.4}$@CNFs and S@CNFs for Li–S batteries, (e) long-term cycling performance of the $S_{0.6}Se_{0.4}$@CNF electrode in Li–S batteries at 1 A g^{-1} for 1000 cycles, (f) cycle performances of $S_{0.6}Se_{0.4}$@CNFs in RT Na–S batteries at a current density of 0.1 A g^{-1}, and (g) cycle performances of $S_{0.6}Se_{0.4}$@CNFs in RT Na–S batteries at a current density of 0.5 A g^{-1} (reproduced with permission from ref. 252. Copyright 2017 Wiley-VCH Verlag GmbH & Co. KGaA, Weinheim).

350 °C for 1 h under an Ar environment. The elemental mapping images shown in Fig. 14(d) revealed that Se was confined within the porous structure of BP-CNF, which further confirmed the existence of small-sized micropores. The electrochemical measurements were performed in 1 M $LiPF_6$ dissolved in EC/DEC (1 : 1 v/v). The CV curves of the Se/BP-CNF cathode displayed two small peaks at 2.3 and 2.1 V (absent in the 2nd cycle) and one main reduction peak at 1.8 V in the first discharge (Fig. 14(e)). These two small peaks at 2.3 and 2.1 V are attributed to the transformation of ring-like selenium (r-Se) into chain-like selenium (c-Se), whereas the strong reduction peak at 1.8 V is due to the conversion of Se to Li_2Se. The oxidation peak at 2.1 V during anodic sweep represents the transformation of Li_2Se into elemental Se. The initial discharge capacities of Se/BP-CNF and Se/M-CNF (M-CNF: mesoporous CNFs without KOH activation, surface area = 209 m^2 g^{-1}) cathodes at a C/2 rate were 921 and 342 mA h g^{-1}, respectively, and their initial coulombic efficiencies were ~81 and ~29%, respectively. The high discharge capacity of the Se/BP-CNF cathode was attributed to the high utilization of c-Se with low-range ordering formed due to the presence of well-developed micropores in the BP-CNF. In contrast, the Se/M-CNF cathode displayed a low initial discharge capacity due to the formation of inactive selenium cores within large carbon nanocages of M-CNF during the selenium melt diffusion process. Notably, the Se/BP-CNF cathode retained ~79.2% (from the 2nd cycle) of the initial discharge capacity at a C/2 rate after 300 cycles (Fig. 14(f)). Moreover, the Se/BP-CNF cathode exhibited excellent rate performance up to 10.0C (capacity ~ 568 mA h g^{-1}) (Fig. 14(g)). The excellent electrochemical properties of Se/BP-CNF cathodes in Li–Se batteries were attributed to the unique electrospun bimodal 1D CNF structures where micropores led to the formation of c-Se with short-range ordering and mesopores facilitated the electrolyte transport and utilization of c-Se. Similarly, Yuan *et al.* recently proposed the use of encapsulated elemental Se in electrospun microporous multichannel CNFs (MCNF) as free-standing cathodes (~38.4 wt%. 1.33 mg cm^{-2} Se in the final cathode) for long cycle life in RT Na–Se batteries (Fig. 14(h)).[57]

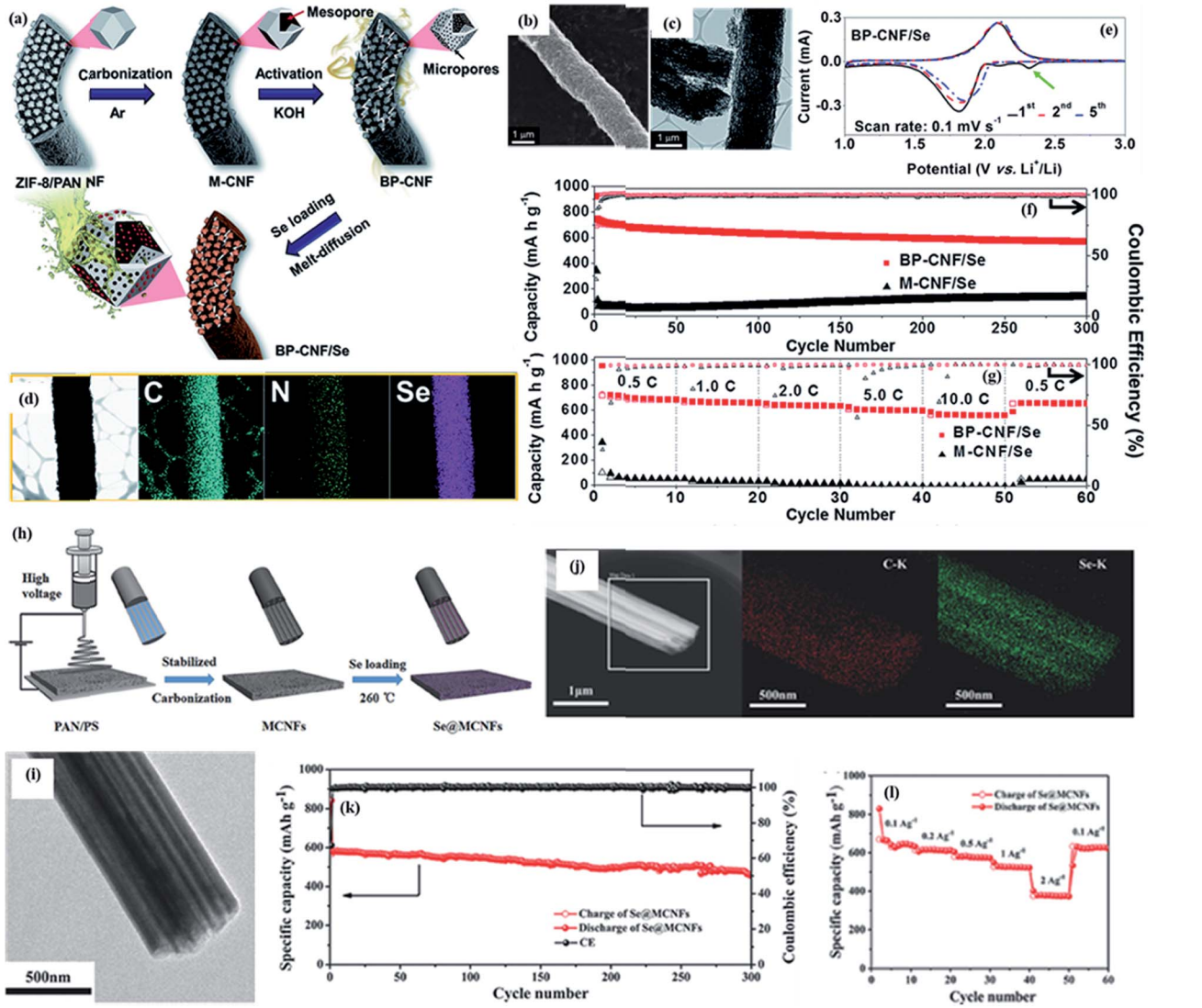

Fig. 14 (a) Formation mechanism of bimodal porous nitrogen-doped carbon nanofibers homogeneously filled with chain-like Se (c-Se), (b and c) SEM and TEM images of the BP-CNF sample, (d) elemental mapping images of Se/BP-CNF cathodes, (e) cyclic voltammograms (CV) of the Se/BP-CNF cathode obtained at 0.1 mV s^{-1} in the potential range of 1.0–3.0 V for the 1st, 2nd, and 5th cycles, (f and g) cycling performance at a current density of 0.5C, and rate performances with the coulombic efficiencies of Se/BP-CNF and Se/M-CNF cathodes (reproduced with permission from ref. 264. Copyright the Royal Society of Chemistry 2018); (h) schematic illustration of the synthesis process of the Se@MCNF electrode, (i and j) TEM image and elemental mapping of the Se@MCNF composite. Red and green correspond to C and Se, respectively. (k) Long-term cycling performance of the RT Na–Se cell based on the Se@MCNF composite at a current density of 0.5 A g^{-1}, and (l) rate capability of the Se@MCNF composite at various current densities (reproduced with permission from ref. 57. Copyright 2017 WILEY-VCH Verlag GmbH & Co. KGaA, Weinheim).

The MCNFs were fabricated by electrospinning a solution of polystyrene (PS)/PAN in DMF solvent and carbonizing the pre-oxidized (280 °C, 3 h, air) PAN/PS nanofibers at 800 °C for 1 h in a N_2 gas flow. The Se was infiltrated into MCNF by heating MCNF and Se powder together at 260 °C for 12 h in a stainless steel vessel sealed under an argon atmosphere. The TEM image and elemental maps of Se@MCNF showed that Se is uniformly impregnated into the micropores and parallel channels present inside the 1D nanofiber structures (Fig. 14(i and j)).

The electrochemical performance was evaluated using 1 M $NaClO_4$ in a mixture of EC : DEC solvents as the electrolyte. The RT Na–Se cells based on the flexible freestanding Se@MCNF cathodes delivered a high specific discharge capacity of ~430 mA h g^{-1} after 300 cycles at 0.5 A g^{-1} with a small capacity decay rate of ~0.067% per cycle (Fig. 14(k)) and remarkable rate performance up to 2 A g^{-1} (379 mA h g^{-1}) (Fig. 14(l)). The excellent electrochemical performance of Se@MCNF cathodes was a consequence of Se-encapsulation into microporous MCNF structures. The encapsulation of Se in MCNF promoted the utilization of Se, alleviated the dissolution and shuttle of polyselenides into the electrolyte and brought about structural stability to the cathode during volume changes. Consequently, the Se@MCNF composite

electrode demonstrated excellent rate capability and long-term cycling when used as a cathode in RT Na–Se batteries. In Table 1, we have summarized the performance of recently reported RT Na–S, Li–S_xSe_y, RT Na–S_xSe_y, Li–Se and RT Na–Se cells based on electrospun structures.

Despite the high cost and low specific capacity of Se compared to S, M–Se (S_xSe_y) batteries have invaluable advantages, which make them attractive for future EVs. With a short practical history of only five years, these batteries have delivered promising results and can compete with their M–S counterparts shortly. The encapsulation of Se or S_xSe_y into rationally designed freestanding electrospun heterostructures appears to be a promising strategy for future advances in these batteries in conventional carbonate electrolytes. Therefore, more intense research is required to explore various electrospun heterostructures as Se hosts, interlayers and membranes in carbonate-based M–Se ($S_{1-x}Se_x$) batteries. Future research efforts should also be actively focused on the use of various *ex situ* and *in situ* techniques to fundamentally understand about the distinct features of Se electrochemistry such as interactions of polyselenides with different host materials, structural and chemical changes in the Se cathode during cycling, and the stability of the S–Se bond during cycling in M–S_xSe_y batteries.

Table 1 Performance of RT Na–S, Li–S_xSe_y, RT Na–S_xSe_y, Li–Se and RT Na–Se cells based on electrospun structures

Sr. No.	Electrode Structure	Electrolyte	Capacity	Cycling
1 (ref. 235)	SPAN/super P/PVDF, 53.9 wt%, 0.7–0.84 mg cm^{-2} S	0.8 M $NaClO_4$ in EC : DEC (1 : 1 = v/v)	Na–S: 219 mA h g_{total}^{-1} at C/10 (5^{th} cycle)	70% retention after 500 cycles
2 (ref. 244)	SPAN (free-standing), 41.0 wt%, ~0.3 mg cm^{-2} S	1 M $NaPF_6$ in EC : DEC (1 : 1 = v/v)	Na–S: 342 mA h g_{sulfur}^{-1} at C/10	77.7% retention after 200 cycles
3 (ref. 107)	Carbon hollow nanobubbles on N- and O-co-doped porous carbon nanofibers (CHNBs@PCNF)/S, 80 wt% active materials: 10 wt% carbon black: 10 wt% carboxyl methylated cellulose (CMC), 57.0 wt%, ~1.4 mg cm^{-2} S	1.0 M $NaClO_4$ in EC : PC (1 : 1 = v/v)	Na–S: 1214 mA h g_{sulfur}^{-1} at C/10	65.0% retention after 50 cycles
4 (ref. 247)	S/$BaTiO_3$–CNF–TiO_2, 60.0 wt%, 1.2–1.4 mg cm^{-2} S (free-standing)	1.0 M $NaClO_4$ in EC : DEC (1 : 1 = v/v)	Na–S: 592 mA h g_{sulfur}^{-1} at 0.5 A g^{-1}	103.21% retention after 400 cycles
5 (ref. 265)	$S_{99.96}Se_{0.04}$/porous CNF, 60.0 wt%, 0.8–1.0 mg cm^{-2} $S_{99.96}Se_{0.04}$ (free-standing)	1 M $LiPF_6$ in EC : DMC (1 : 1 = v/v); 1.0 M $NaClO_4$ in EC : PC (1 : 1 = v/v)	Li–S: 1100 mA h g_{S-Se}^{-1} at 0.1 A g^{-1} Na–S: 1375 mA h g_{S-Se}^{-1} at 0.1 A g^{-1}	76.4% (Li–S) and 55.4% (Na–S) after 100 cycles
6 (ref. 252)	$S_{0.6}Se_{0.4}$/CNF, 57.5 wt%, 0.9 mg cm^{-2} $S_{0.6}Se_{0.4}$ (free-standing)	1 M $LiPF_6$ in EC : DEC (1 : 1 = v/v); 1.0 M $NaClO_4$ in EC : PC (1 : 1 = v/v)	Li–S: ~350 mA h g_{S-Se}^{-1} at 1 A g^{-1} Na–S: 417 mA h g_{S-Se}^{-1} at 0.1 A g^{-1}	~100% (Li–S) retention after 1000 cycles and 90% (Na–S) retention after 100 cycles
7 (ref. 262)	Se/CNFs–CNT, 35 wt% Se (free-standing)	1 M $LiPF_6$ in EC : DEC (1 : 1 = v/v); 1.0 M $NaClO_4$ in EC : DEC (1 : 1 = v/v)	Li–Se: ~950 mA h g_{Se}^{-1} at 0.5 A g^{-1} Na–Se: 781 mA h g_{Se}^{-1} at 0.05 A g^{-1}	~54.4% (Li–Se) retention after 500 cycles and 74.6% (Na–Se) retention after 80 cycles
8 (ref. 263)	Se/hierarchical porous CNF–rGO, 80 wt% active material: 10 wt% acetylene, black: 10 wt% PVDF, 57 wt% Se	1 M $LiPF_6$ in EC : EMC:DMC (mass ratio 1 : 1:1)	Li–Se: ~632 mA h g_{Se}^{-1} at C/5	~97.5% retention after 50 cycles
9 (ref. 264)	Se-infiltrated MOF-derived porous CNF, 70 wt% active material: 10 wt% carbon (super P): 10 wt% sodium carboxymethyl cellulose, (CMC), 42 wt% Se	1 M $LiPF_6$ in EC : DEC (1 : 1 = v/v)	Li–Se: ~742 mA h g_{Se}^{-1} at C/2 (2^{nd} cycle)	~79.2% retention (from the 2^{nd} cycle) after 300 cycles
10 (ref. 57)	Se/microporous multichannel CNF, 80 wt% active material: 10 wt% acetylene black: 10 wt% PVDF, ~38.4 wt%. 1.33 mg cm^{-2} Se	1.0 M $NaClO_4$ in EC : DEC (1 : 1 = v/v)	Na–Se: ~578 mA h g_{Se}^{-1} at 0.5 A g^{-1} (2^{nd} cycle)	~74.4% retention (from the 2^{nd} cycle) after 300 cycles

4. Statistical analysis of the electrochemical performance

To understand the advantages of electrospun free-standing nanostructures, we provide a comparative analysis of recently reported Li–S cells based on non-electrospun powdered, slurry-cast electrospun and free-standing electrospun nanostructures. Because it is challenging to compare the electrochemical performance of literature reports due to large differences in sulfur fraction/areal loading, conditioning cycles, and the resulting capacity, we have introduced the 'fraction of (electrochemically) active cathode (FAC)' as a parameter to account for these differences as given below:

$$\mathrm{FAC}\ (\%) = \frac{f_s \times C_s}{C_{th}} = 100 \times \frac{C_s \times W_s}{(W_T)} \times \frac{1}{C_{th}}$$

$$\mathrm{FAC}'\ (\%) = 100 \times \frac{C_s \times W_s}{(W_T + A \times W_{Al})} \times \frac{1}{C_{th}}$$

where f_s is the sulfur content (weight%) in the final cathode, C_{th} is the theoretical capacity of sulfur (1675 mA h g^{-1}), C_s is the specific capacity (mA h g^{-1}) at a given C rate, W_s is the absolute sulfur amount in the cathode (mg), W_T is the absolute total weight of the cathode including binders, and conducting additives (mg), A is the area of the electrode (cm^2, equals to the absolute sulfur weight/areal loading of sulfur), and W_{Al} is the areal loading of the additional current collector (Al foil, 4 mg cm^{-2}). The first equation for FAC represents the sulfur (active) content in the cathode without the weight of the additional Al foil (current collector), which is usually 3–5 mg cm^{-2}. We have considered the areal loading of the Al foil as 4 mg cm^{-2} for the present analysis. The second equation for FAC′ includes the weight of the additional Al foil as well. The 'FAC' can be seen as a fraction of sulfur electrochemically active in the final cathode (*i.e.*, sulfur content in the final cathode multiplied by the ratio of achieved capacity at a given C rate and theoretical capacity), which is the source for the cell capacity. The concept of the fraction of (electrochemically) active cathode (FAC) will be of great importance in future to represent reliable electrochemical performances as FAC would be more realistic than sulfur content in the composites or in the final cathodes. Since RT Na–S and M–Se batteries are in their nascent stage, we have not included these reports for the FAC calculations. The comparative analysis of FAC for non-electrospun powdered, slurry-cast electrospun and free-standing electrospun nanostructures has led to the following conclusions:

(a) As mentioned in the Introduction section, an areal sulfur loading of ≥5 mg cm^{-2} along with a high sulfur content (≥70% in the final cathode), sulfur utilization (≥70%) and a low E/S ratio of ∼3–4 μL mg^{-1} is required for the commercialization of Li–S cells in order to outperform the energy density of commercial Li-ion batteries. In other words, practical Li–S cells demand an areal sulfur loading of ≥5 mg cm^{-2} along with a FAC of ∼50% (green line in the figures) and an E/S ratio of ∼3–4 μL mg^{-1}. Fig. 15(a) presents the calculated FAC of recently reported various non-electrospun powdered, slurry-cast electrospun and free-standing electrospun nanostructure based Li–S cells. The FAC of most of the non-electrospun powdered and slurry-cast electrospun nanostructure based Li–S cells is between 20 and 50%. In contrast, the FAC values of most of the free-standing electrospun nanostructure based Li–S cells are between 30 and 60%.

(b) The effect of an additional current collector *i.e.* Al foil can be clearly seen in Fig. 15(b), which represents the calculated FAC content based on the total weight of the cathode material (including binders and conducting additives) and the weight of the Al foil. The FAC content for non-electrospun powdered and slurry-cast electrospun nanostructure based electrodes is significantly reduced to ≤30%, whereas the FAC content for free-standing electrospun nanostructure based electrodes remains unchanged.

(c) Fig. 15(c) shows the FAC content (including Al-foil weight) as functions of the areal loading of sulfur and E/S ratio. Although free-standing electrospun nanostructure based electrodes exhibit a relatively higher FAC content, it is still a challenge to construct such electrodes at a high sulfur loading and use them at a low E/S ratio as evident from Fig. 15(c).

The free-standing 3D architecture of electrospun nanostructures not only provides continuous 1D pathways for electrons, better wettability, and a robust electrode structure but also accommodates volume changes during oxidation/reduction. In contrast, the morphology and the porosity of powdered material-based cathodes after the harsh slurry process and their effect on the device performance are uncomprehending. Moreover, these free-standing architectures eliminate the need for additional dead weight. In contrast, the use of specially designed powdered nanostructures as a sulfur host involves a harsh slurry-cast process with the use of inactive heavy elements such as binders/conductive agents (*e.g.*, 10 wt% conducting carbon and 10 wt% poly(vinylidene fluoride)) and additional current collectors (aluminum, usually 3–5 mg cm^{-2}). The presence of these additional dead elements deteriorates the final effective specific capacity (or FAC content) of packed Li–S cells. For example, for a free-standing carbon nanostructure based S-cathode with 70 wt% sulfur in the S/C composite (total areal loading of the S/C composite = 1 mg cm^{-2} and area of the electrode = 1 cm^2, no binder, no additive, no Al foil) and 1000 mA h g^{-1} capacity at a given C rate, the FAC content will be around 42%. In contrast, for a powdered carbon nanostructure based S-cathode with 70 wt% sulfur in the composite (total areal loading of the S/C composite with a binder and conducting additive = 1 mg cm^{-2} and area of the electrode = 1 cm^2) and 1000 mA h g^{-1} capacity at a given C rate, the FAC content will be around 33%, considering 20 wt% being binders and conductive additives. Furthermore, if we include the weight of the additional current collector (Al foil, ∼4 mg cm^{-2}) used to prepare the cathode during the slurry cast process, the FAC content for this powdered S/C nanostructure will further reduce to ∼7% only. Undoubtedly, free-standing electrospun nanostructures pave the way for improving the electrochemical performance of Li–S batteries by eliminating dead elements – binders, conducting additives and additional Al-foil collectors as evident from

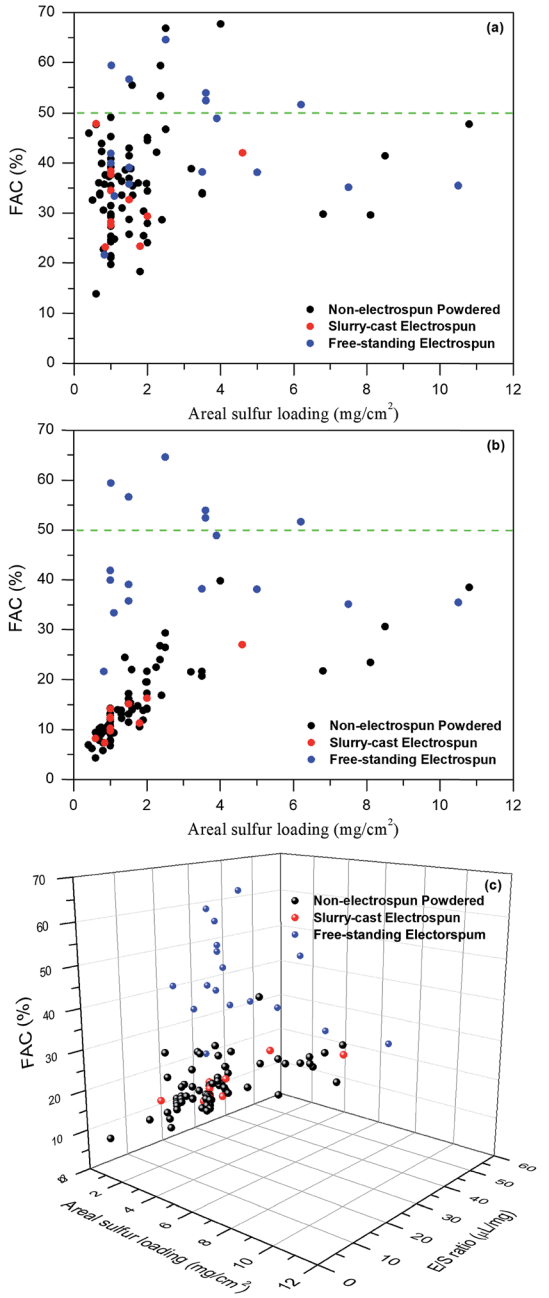

Fig. 15 (a) 'Fraction of (electrochemically) active cathode (FAC)' in the final cathode (without the weight of an additional Al-current collector) *vs.* areal sulfur loading for various non-electrospun powdered, slurry-cast electrospun, and free-standing electrospun nanostructure based Li–S cells reported recently in the literature, (b) 'Fraction of (electrochemically) active cathode (FAC)' in the final cathode (including the weight of an additional Al-current collector 4 mg cm^{-2}) *vs.* areal sulfur loading for various non-electrospun powdered, slurry-cast electrospun, and free-standing electrospun nanostructure based Li–S cells reported recently in the literature, (c) 'Fraction of (electrochemically) active cathode (FAC)' in the final cathode (including the weight of an additional Al-current collector 4 mg cm^{-2}) *vs.* areal sulfur loading and electrolyte to sulfur (E/S) ratio for various non-electrospun powdered, slurry-cast electrospun, and free-standing electrospun nanostructure based Li–S cells reported recently in the literature. The area of the electrodes/cathodes, E/S ratio, and interlayer weight are considered as 1 cm^2, 20 μL mg^{-1}, and 1 mg, respectively, for the papers, which haven't reported these values. Moreover, we have calculated the 'Fraction of (electrochemically) active cathode (FAC)' at C/10, C/5, C/2 and 1C rates for a given paper and chosen the maximum value. The dotted green line represents the required FAC value for the practicality of Li–S cells.

Fig. 15. The intensive research carried out on the development of advanced electrospun nanostructures in recent years has brought about consistent progress in these batteries in terms of capacity, rate capability, and cycle stability as discussed in this review article. With recent achievements and advanced efforts, we believe that the development of rationally designed free-standing 3D electrospun nanostructures with a high sulfur loading, high FAC content, and low E/S ratio will be an important topic of research in future years for the practicality of Li–S batteries.

Another critical issue is that in most of the reports regardless of the cathode structure (electrospun or non-electrospun), the E/S ratio is ≥30 μL mg^{-1} (Fig. 15(c)). To reflect the effect of the electrolyte, we consider that 50% of the cell electrolyte is held within the pores and voids of cathodes. In this scenario, for a given areal sulfur loading (1 mg cm^{-2}), sulfur fraction of ~50% in the electrode, and area (A) of the electrode (1 cm^2), the weight of the electrolyte ($W_{\text{electrolyte}} = 0.5 \times A \times A_S \times f_S \times \rho =$ 15 mg, ρ = electrolyte density (1 mg μL^{-1} assumed)) at a high E/S ratio (30 μL mg^{-1}) becomes a deciding factor for the total cell capacity. Therefore, another important step should be to reduce the E/S ratio to 3–4 μL mg^{-1} ($W_{\text{electrolyte}} = 2$ mg) in order to utilize the potential of non-electrospun powdered, slurry-cast electrospun and free-standing electrospun cathodes. In free-standing electrospun nanostructures, porosity and inherent excessive voids present in the 3D architecture necessitate a high E/S ratio for better sulfur utilization, especially at a high sulfur loading. Therefore, the effect of the E/S ratio becomes more dominating in the case of free-standing electrospun nanostructures since $W_T = 2$ mg and $A \times W_{Al} = 0$ mg due to their free-standing nature.

5. Concluding remarks and future prospects

In a brief summary, we have systematically reviewed recently reported advanced strategies for obtaining novel electrospun electrode materials for S and Se based lithium and sodium batteries. In particular, we have evaluated various electrospun nanostructures including hierarchical porous CNFs, heteroatom doped CNFs, CNF interlayers, catholytes and Li_2S with CNFs, 3D PANI/CNF nanostructures and SPAN in carbonate electrolytes, various electrospun oxides, carbides and metallic heterostructures as hosts, interlayers, and separator coatings in Li–S batteries. In addition, we have discussed porous CNFs and various heterostructures in RT Na–S, Li–S_xSe_y, RT Na–S_xSe_y, Li–Se and RT Na–Se batteries. In Section 3.1.1, we have placed an emphasis on the influence of the hierarchical porosity and large pore volume of electrospun CNFs to achieve high areal capacity in Li–S cells. The Li–S cells have shown promising performances by (a) tailoring the pore size, pore volume and surface area of

electrospun CNFs *via* different activation agents and sacrificial templates, (b) modifying the methods of sulfur infiltration into CNFs, and (c) using Li_2S or catholytes as starting active materials with CNFs. Furthermore, in this section, we have discussed the use of heteroatom doped CNFs and novel configurations with porous/functionalized CNF interlayers to improve the electrochemical performance of Li–S cells. In Section 3.1.2, we have focused on the (a) use of advanced electrospun nanostructures of conducting polymers in the cathode and cyclized PAN in the interlayers, (b) sulfurized PAN with the conventional carbonate electrolyte, and (c) electrospun membranes as gel polymer electrolytes for achieving high performance in Li–S cells. Furthermore, in Section 3.1.3, this review focuses on the improvement in the electrochemical performance of Li–S cells using various electrospun oxide, carbide and metallic heterostructures. The emphasis is placed on the recent approaches for introducing PS-functionality (polar–polar, Lewis acid–base or polythionate type) and e-functionality (conductivity and catalytic activity) into single heterostructure by electrospinning organic/inorganic hybrid gels. Finally, in Sections 3.2 and 3.3, we have discussed recently reported advanced electrospun nanostructures designed for RT Na–S and M–Se batteries to bring substantial improvements in electrochemical performance.

It is important to note that key factors for practical Li–S batteries are high gravimetric and volumetric capacity, high FAC content, high areal sulfur loading, prolonged cycle life, and cheap mass production of materials. Despite the considerable progress made so far using electrospun nanostructures, there are still several bottlenecks and substantial development room for performance enhancement in Li–S batteries. One of the long-lasting challenges is the development of high-performance thick (high-sulfur loading) free-standing S-cathodes. The limited diffusion pathways, electrolyte uptake and kinetics, and severe pulverization in thick S-cathodes result in poor sulfur utilization and short cycle life. Therefore, the development of thick S-electrodes using free-standing electrospun nanostructures demands a 3D architecture that can accommodate a large amount of sulfur and the corresponding volume expansion, maintain the electron conducting and ionic pathways over cycling, and effectively suppress the shuttle effect, while minimizing the electrolyte volume. Important factors to be considered while developing such free-standing 3D architectures are porosity, pore volume, void size, surface area, and electrical conductivity. The use of recently reported hierarchically porous (micropores for polysulfide blocking and mesopores for high S loading) electrospun nanostructures is one of the promising solutions to develop thick S-cathodes with a high areal loading and FAC content. We emphasize that the influence of the parameters of electrospun nanostructures (porosity, pore volume, void size, surface area, and electrical conductivity) should be further studied to comprehensively understand the correlations between the structural features/surface activity of nanostructures and sulfur loading/FAC content, which will eventually help to achieve optimal electrochemical performance. Furthermore, simply increasing the sulfur loading in free-standing electrospun nanostructures only deteriorates the overall cell performance and neutralizes the advantages of electrospun materials. Therefore, new cell configurations also need to be investigated. One possible approach is to construct layer-by-layer 3D S-cathodes using free-standing nanostructures where the thin top and bottom layers (highly microporous) function as polysulfide trapping layers, and the central layers with hierarchical (micro–meso) porosity serve as hosts for a large amount of sulfur. The areal sulfur loading and electrochemical performance can be augmented by adjusting the number of layers and tuning PS functionality (micro-porosity, heteroatom doping, oxides, carbides *etc.*) into top and bottom layers. Second, uniform dispersion of S into the host matrix is essential for high sulfur utilization, especially at high S loadings. The commonly used S melt-infiltration techniques result in the formation of large inactive cores of sulfur (poor S utilization) in voids/inter-fiber macropores of free-standing electrospun 3D architectures, especially in thick electrodes. Therefore, alternative approaches for sulfur impregnation should also be explored to develop thick free-standing 3D electrodes. The possible solutions are (a) chemical synthesis of nanosized sulfur directly on an electrospun architecture and (b) use of catholytes.

To ensure high capacities and prolong cycling, especially at a high sulfur loading, not only the textural properties but also the electronic conductivity of electrospun nanostructures is paramount. The use of 3D architectures of heteroatom doped hierarchically porous electrospun CNFs further decorated with conducting nanoparticles (*e.g.* non-stoichiometric oxides such as Ti_4O_7 and TiO; carbides *e.g.* TiC or metallic Co nanoparticles) would serve as ideal candidates for developing thick S cathodes. Nevertheless, it is important to control the low mass-fraction/loading (3–5%) of electrochemically inactive functional species (*e.g.*, oxides, carbides, and metals) for achieving a high FAC content.

Finally, it is worth mentioning that the poor packing of electrospun nanofibers in free-standing 3D architectures usually results in low volumetric density. The continuous alignment of nanofibers during electrospinning would be a possible strategy not only to improve sulfur distribution within the electrospun host matrix (due to small sized voids in aligned fibers) but also to increase volumetric energy in Li–S batteries. The use of recently developed free-standing electrospun Li_2S nanostructures is also recommended to build Li-anode free practical Li–S batteries with high energy density. These free-standing Li_2S nanostructures not only can overcome the initial activation barrier associated with micro-sized powdered Li_2S particles but also can be combined with alternate (Si and carbon) anodes.

Another important factor is the E/S ratio, which is crucial for designing high energy density Li–S cells. As mentioned earlier, inter-fiber macropores/voids of the free-standing 3D architecture of electrospun nanofibers necessitate a high E/S ratio in Li–S batteries. In this context, the use of catholytes or GPEs with rationally designed free-standing electrospun nanostructures having PS and e-functionality (conductivity, polysulfide trapping capability and catalytic activity) would be possible approaches to simultaneously reduce the E/S ratio and achieve a high sulfur loading (or FAC content) in cathodes. Sulfurized

PAN or similar covalently bonded sulfur based electrospun nanostructures are also interesting as the required amount of electrolyte for such materials is essentially the same as that for Li-ion batteries. However, grafted or tethered polysulfide chains could be more useful than covalently bonded S atoms in order to simultaneously achieve a high sulfur content in the final cathode. The continuous depletion of the electrolyte during cycling due to side reactions with metallic anodes also accounts for a high E/S ratio. Therefore, integration of free-standing electrospun nanostructured based cathodes with stabilized metallic anodes (with a stable SEI layers) may be a promising strategy for achieving a low E/S ratio.

RT Na–S battery systems are still in their nascent stage. Due to the large size of Na^+ than Li^+, the volume change of the sulfur cathode (~260% for complete reduction of S to Na_2S) will be one of the most critical issues for RT Na–S batteries, even more severe than that for the analogous Li–S batteries. In this regard, the development of advanced electrospun nanostructures to accommodate the volume expansion of sulfur cathodes during deep charge/discharge will be more demanding. The electrospun carbon nanostructures with fine tuning of porosity (ion and electron pathways), surface functionality (*e.g.*, heteroatoms), and well embedded ultrafine nanoparticles of conducting non-stoichiometric oxides or metals can lead to high capacity and long-term cycling and circumvent the pulverization (particle cracking and fracture induced by volume expansion) of the electrode during sodiation/de-sodiation. Similarly, selenium based battery systems *viz.*, Li–S_xSe_y, RT Na–S_xSe_y, Li–Se, and RT Na–Se are also in their nascent stage. One of the promising approaches is to leverage the semiconducting nature of selenium to address the poor conductivity of S cathodes to improve sulfur utilization and rate performance. S–Se mixtures are miscible in all proportions, and various S_xSe_y compounds can be prepared, including SSe_5, S_2Se_5, S_4Se_5, SSe, S_5Se_3, S_2Se, and S_7Se, as well as a S_xSe_y compound with a very low amount of Se such as $S_{20}Se$. These S_xSe_y materials offer higher theoretical capacities (675–1550 mA h g^{-1}) compared to Se alone, with substantially improved conductivity compared to that of pure S electrodes. On the other side, the electrical conductivity is not an issue for the Se electrode in Li–Se and RT Na–Se batteries due to its semiconducting nature. However, in both M–Se and M–S_xSe_y batteries, shuttling of intermediate polyselenides and volume expansion are major bottlenecks. Therefore, the progress made over the last few years in Li–S cells using free-standing electrospun nanostructures should be exploited extensively for significant breakthroughs in Se based battery systems. Future studies should focus on the (a) development of rationally designed advanced free-standing electrospun nanostructures for high performance thick Se cathodes, (b) optimization of the S : Se ratio in S_xSe_y compounds for optimal performance in terms of capacity, cycling, and rate capability, and (c) new device configurations with layer-by-layer 3D cathodes, functional interlayers and separators. Furthermore, research efforts on the fundamental understanding of electrochemistry involved (reduction/oxidation mechanisms and performance deteriorating factors) in M–Se (S_xSe_y) systems in different electrolyte systems are vital.

It is critical to maintain the intrinsic properties of electrospun nanostructures at a high production rate. The controllability and degree of accuracy achievable in the fabrication process of electrospun nanostructures are important for their application on an industrial scale. In terms of reproducibility and accuracy in the production stage, electrospun nanostructures are affected by solution (viscosity, concentration, electrical conductivity, and surface tension), equipment (flow rate and voltage), and environmental process parameters (humidity and temperature). We have discussed all these parameters in brief in Section 2. For more information, we refer the readers to review articles focusing on various electrospun fabrication techniques, conditions/parameters for product reproducibility, and challenges and prospects for transition of electrospinning technology from the lab scale to mass production.[53–55,74,75,77,85] We believe that research should also be centered on fabrication strategies for low cost and industrial scale production of electrospun nanostructures to meet the demand for the abovementioned practical battery systems. It remains a major bottleneck to produce electrospun nanostructures on an industrial scale using the single-nozzle electrospinning technique because the rate of fiber production depends on the concentration, the density of spinning jets and the volume of solution forming spinning jets. Multi-nozzle electrospinning, bubble electrospinning, and needleless electrospinning are promising alternatives to the single-nozzle electrospinning technique for mass-production of electrospun nanostructures with high reproducibility. However, at present, these new techniques are too expensive. Nevertheless, these electrospinning techniques will be promising candidates to realize cost-effective large scale production of free-standing nanostructures in the near future.

Conflicts of interest

There are no conflicts to declare.

Acknowledgements

The authors would like to thank the National Science Foundation (Award#s CMMI-1537827, CBET-1804374) and Drexel Ventures Innovations Fund (DVIF) for funding. The authors would like to thank Ayda Rafie (pursuing Ph.D. in our group) for her assistance with the preparation of the figures presented in the conclusion section.

References

1 Z. Yang, J. Zhang, M. C. Kintner-Meyer, X. Lu, D. Choi, J. P. Lemmon and J. Liu, *Chem. Rev.*, 2011, **111**, 3577–3613.
2 J. Muldoon, C. B. Bucur and T. Gregory, *Chem. Rev.*, 2014, **114**, 11683–11720.
3 H. Ibrahim, A. Ilinca and J. Perron, *Renewable Sustainable Energy Rev.*, 2008, **12**, 1221–1250.
4 I. Hadjipaschalis, A. Poullikkas and V. Efthimiou, *Renewable Sustainable Energy Rev.*, 2009, **13**, 1513–1522.
5 K. M. Abraham, *J. Phys. Chem. Lett.*, 2015, **6**, 830–844.

6 C. Wadia, P. Albertus and V. Srinivasan, *J. Power Sources*, 2011, **196**, 1593–1598.
7 J. Liu, J.-G. Zhang, Z. Yang, J. P. Lemmon, C. Imhoff, G. L. Graff, L. Li, J. Hu, C. Wang, J. Xiao, G. Xia, V. V. Viswanathan, S. Baskaran, V. Sprenkle, X. Li, Y. Shao and B. Schwenzer, *Adv. Funct. Mater.*, 2013, **23**, 929–946.
8 J. Yan, Q. Wang, T. Wei and Z. Fan, *Adv. Energy Mater.*, 2014, **4**, 1300816–1300858.
9 G. Wang, L. Zhang and J. Zhang, *Chem. Soc. Rev.*, 2012, **41**, 797–828.
10 S. M. G. Mousavi, F. Faraji, A. Majazi and K. Al-Haddad, *Renewable Sustainable Energy Rev.*, 2017, **67**, 477–490.
11 S. Rehman, L. M. Al-Hadhrami and M. M. Alam, *Renewable Sustainable Energy Rev.*, 2015, **44**, 586–598.
12 M. Budt, D. Wolf, R. Span and J. Yan, *Appl. Energy*, 2016, **170**, 250–268.
13 Y. Sun, N. Liu and Y. Cui, *Nat. Energy*, 2016, **1**, 16071–16082.
14 J. Cabana, L. Monconduit, D. Larcher and M. R. Palacin, *Adv. Mater.*, 2010, **22**, E170–E192.
15 M. S. Whittingham, *Chem. Rev.*, 2004, **104**, 4271–4301.
16 N. Nitta, F. Wu, J. T. Lee and G. Yushin, *Mater. Today*, 2015, **18**, 252–264.
17 G. E. Blomgren, *J. Electrochem. Soc.*, 2017, **164**, A5019–A5025.
18 M. N. Obrovac and V. L. Chevrier, *Chem. Rev.*, 2014, **114**, 11444–11502.
19 M. M. Thackeray, C. Wolverton and E. D. Isaacs, *Energy Environ. Sci.*, 2012, **5**, 7854–7863.
20 A. Manthiram, *ACS Cent. Sci.*, 2017, **3**, 1063–1069.
21 M. S. Whittingham, *Chem. Rev.*, 2014, **114**, 11414–11443.
22 M. R. Palacin, *Chem. Soc. Rev.*, 2009, **38**, 2565–2575.
23 M. Wild, L. O'Neill, T. Zhang, R. Purkayastha, G. Minton, M. Marinescu and G. J. Offer, *Energy Environ. Sci.*, 2015, **8**, 3477–3494.
24 R. Chen, R. Luo, Y. Huang, F. Wu and L. Li, *Adv. Sci.*, 2016, **3**, 1600051–1600089.
25 J. Pan, Y. Y. Xu, H. Yang, Z. Dong, H. Liu and B. Y. Xia, *Adv. Sci.*, 2018, **5**, 1700691–1700720.
26 D. Aurbach, B. D. McCloskey, L. F. Nazar and P. G. Bruce, *Nat. Energy*, 2016, **1**, 16128–16138.
27 Y. Liu, Q. Sun, W. Li, K. R. Adair, J. Li and X. Sun, *Green Energy Environ.*, 2017, **2**, 246–277.
28 A. Manthiram and X. Yu, *Small*, 2015, **11**, 2108–2114.
29 P. Saha, M. K. Datta, O. I. Velikokhatnyi, A. Manivannan, D. Alman and P. N. Kumta, *Prog. Mater. Sci.*, 2014, **66**, 1–86.
30 L. J. Hardwick and C. P. de León, *Johnson Matthey Technol. Rev.*, 2018, **62**, 134–149.
31 L. D. Chen, J. K. Nørskov and A. C. Luntz, *J. Phys. Chem. C*, 2015, **119**, 19660–19667.
32 J. G. Smith, J. Naruse, H. Hiramatsu and D. J. Siegel, *Chem. Mater.*, 2017, **29**, 3152–3163.
33 A. A. Yaroshevsky, *Geochem. Int.*, 2006, **44**, 48–55.
34 Z. Hu and S. Gao, *Chem. Geol.*, 2008, **253**, 205–221.
35 W. Guo and Y. Fu, *Energy Environ. Mater.*, 2018, **1**, 20–27.
36 A. Manthiram, Y. Fu, S. H. Chung, C. Zu and Y. S. Su, *Chem. Rev.*, 2014, **114**, 11751–11787.
37 P. G. Bruce, S. A. Freunberger, L. J. Hardwick and J. M. Tarascon, *Nat. Mater.*, 2012, **11**, 19–29.
38 R. Demir-Cakan, M. Morcrette, G. Babu, A. Guéguen, R. Dedryvère and J.-M. Tarascon, *Energy Environ. Sci.*, 2013, **6**, 176–182.
39 M. K. Song, E. J. Cairns and Y. Zhang, *Nanoscale*, 2013, **5**, 2186–2204.
40 Z. Zhao-Karger and M. Fichtner, *MRS Commun.*, 2017, **7**, 770–784.
41 A. Robba, A. Vizintin, J. Bitenc, G. Mali, I. Arčon, M. Kavčič, M. Žitnik, K. Bučar, G. Aquilanti, C. Martineau-Corcos, A. Randon-Vitanova and R. Dominko, *Chem. Mater.*, 2017, **29**, 9555–9564.
42 P. G. Bruce, B. Scrosati and J. M. Tarascon, *Angew. Chem., Int. Ed. Engl.*, 2008, **47**, 2930–2946.
43 Y. Yang, G. Zheng and Y. Cui, *Chem. Soc. Rev.*, 2013, **42**, 3018–3032.
44 X. Fang and H. Peng, *Small*, 2015, **11**, 1488–1511.
45 W. Kang, N. Deng, J. Ju, Q. Li, D. Wu, X. Ma, L. Li, M. Naebe and B. Cheng, *Nanoscale*, 2016, **8**, 16541–16588.
46 Y. X. Yin, S. Xin, Y. G. Guo and L. J. Wan, *Angew. Chem., Int. Ed.*, 2013, **52**, 13186–13200.
47 C. P. Yang, Y. X. Yin and Y. G. Guo, *J. Phys. Chem. Lett.*, 2015, **6**, 256–266.
48 A. Abouimrane, D. Dambournet, K. W. Chapman, P. J. Chupas, W. Weng and K. Amine, *J. Am. Chem. Soc.*, 2012, **134**, 4505–4508.
49 Y. Liu, Z. Tai, Q. Zhang, H. Wang, W. K. Pang, H. K. Liu, K. Konstantinov and Z. Guo, *Nano Energy*, 2017, **35**, 36–43.
50 G.-L. Xu, J. Liu, R. Amine, Z. Chen and K. Amine, *ACS Energy Lett.*, 2017, **2**, 605–614.
51 A. Eftekhari, *Sustainable Energy Fuels*, 2017, **1**, 14–29.
52 L. Li, S. Peng, J. K. Y. Lee, D. Ji, M. Srinivasan and S. Ramakrishna, *Nano Energy*, 2017, **39**, 111–139.
53 J. V. Patil, S. S. Mali, A. S. Kamble, C. K. Hong, J. H. Kim and P. S. Patil, *Appl. Surf. Sci.*, 2017, **423**, 641–674.
54 S. Cavaliere, S. Subianto, I. Savych, D. J. Jones and J. Rozière, *Energy Environ. Sci.*, 2011, **4**, 4761–4785.
55 Z. Dong, S. J. Kennedy and Y. Wu, *J. Power Sources*, 2011, **196**, 4886–4904.
56 Q. Liu, J. Zhu, L. Zhang and Y. Qiu, *Renewable Sustainable Energy Rev.*, 2018, **81**, 1825–1858.
57 B. Yuan, X. Sun, L. Zeng, Y. Yu and Q. Wang, *Small*, 2018, **14**, 1703252–1703258.
58 H. J. Peng, J. Q. Huang and Q. Zhang, *Chem. Soc. Rev.*, 2017, **46**, 5237–5288.
59 Z. W. Seh, Y. Sun, Q. Zhang and Y. Cui, *Chem. Soc. Rev.*, 2016, **45**, 5605–5634.
60 M. Xu, M. Wang, H. Xu, H. Xue and H. Pang, *Chem.–Asian J.*, 2016, **11**, 2967–2995.
61 V. Thavasi, G. Singh and S. Ramakrishna, *Energy Environ. Sci.*, 2008, **1**, 205–221.
62 X. Li, Y. Chen, H. Huang, Y.-W. Mai and L. Zhou, *Energy Storage Materials*, 2016, **5**, 58–92.
63 J.-W. Jung, C.-L. Lee, S. Yu and I.-D. Kim, *J. Mater. Chem. A*, 2016, **4**, 703–750.

64 A. Chinnappan, C. Baskar, S. Baskar, G. Ratheesh and S. Ramakrishna, *J. Mater. Chem. C*, 2017, **5**, 12657–12673.
65 Z. Li, J.-w. Zhang, L.-g. Yu and J.-w. Zhang, *J. Mater. Sci.*, 2017, **52**, 6173–6195.
66 S. Peng, L. Li, J. Kong Yoong Lee, L. Tian, M. Srinivasan, S. Adams and S. Ramakrishna, *Nano Energy*, 2016, **22**, 361–395.
67 B. Zhang, F. Kang, J.-M. Tarascon and J.-K. Kim, *Prog. Mater. Sci.*, 2016, **76**, 319–380.
68 S. Kalluri, K. H. Seng, Z. Guo, H. K. Liu and S. X. Dou, *RSC Adv.*, 2013, **3**, 25576–25601.
69 L. Mai, J. Sheng, L. Xu, S. Tan and J. Meng, *Acc. Chem. Res.*, 2018, **51**, 950–959.
70 L. Zeng, X. Wei, J. Wang, Y. Jiang, W. Li and Y. Yu, *J. Power Sources*, 2015, **281**, 461–469.
71 Y. He, B. Matthews, J. Wang, L. Song, X. Wang and G. Wu, *J. Mater. Chem. A*, 2018, **6**, 735–753.
72 T. Jin, Q. Han, Y. Wang and L. Jiao, *Small*, 2018, **14**, 1703086–1703111.
73 W. Li, M. Li, K. R. Adair, X. Sun and Y. Yu, *J. Mater. Chem. A*, 2017, **5**, 13882–13906.
74 M. Inagaki, Y. Yang and F. Kang, *Adv. Mater.*, 2012, **24**, 2547–2566.
75 S. Agarwal, A. Greiner and J. H. Wendorff, *Prog. Polym. Sci.*, 2013, **38**, 963–991.
76 V. Beachley and X. Wen, *Mater. Sci. Eng., C*, 2009, **29**, 663–668.
77 C. L. Zhang and S. H. Yu, *Chem. Soc. Rev.*, 2014, **43**, 4423–4448.
78 S.-H. Chung, P. Han, R. Singhal, V. Kalra and A. Manthiram, *Adv. Energy Mater.*, 2015, **5**, 1500738–1500749.
79 A. Singh and V. Kalra, *ACS Appl. Mater. Interfaces*, 2018, **10**, 37937–37947.
80 S. H. Chung, R. Singhal, V. Kalra and A. Manthiram, *J. Phys. Chem. Lett.*, 2015, **6**, 2163–2169.
81 J. S. Lee, W. Kim, J. Jang and A. Manthiram, *Adv. Energy Mater.*, 2016, **7**, 1601943–1601950.
82 L. Ji, M. Rao, S. Aloni, L. Wang, E. J. Cairns and Y. Zhang, *Energy Environ. Sci.*, 2011, **4**, 5053–5059.
83 Y. Chen, X. Li, K.-S. Park, J. Hong, J. Song, L. Zhou, Y.-W. Mai, H. Huang and J. B. Goodenough, *J. Mater. Chem. A*, 2014, **2**, 10126–10130.
84 Z. Li, J. T. Zhang, Y. M. Chen, J. Li and X. W. Lou, *Nat. Commun.*, 2015, **6**, 8850–8857.
85 A. L. Yarin, *Polym. Adv. Technol.*, 2011, **22**, 310–317.
86 H. Qu, S. Wei and Z. Guo, *J. Mater. Chem. A*, 2013, **1**, 11513–11528.
87 J. Jin, X. Tian, N. Srikanth, L. B. Kong and K. Zhou, *J. Mater. Chem. A*, 2017, **5**, 10110–10126.
88 H. Lv, R. Chen, X. Wang, Y. Hu, Y. Wang, T. Chen, L. Ma, G. Zhu, J. Liang, Z. Tie, J. Liu and Z. Jin, *ACS Appl. Mater. Interfaces*, 2017, **9**, 25232–25238.
89 A. Rosenman, E. Markevich, G. Salitra, D. Aurbach, A. Garsuch and F. F. Chesneau, *Adv. Energy Mater.*, 2015, **5**, 1500212–1500232.
90 Y.-X. Wang, B. Zhang, W. Lai, Y. Xu, S.-L. Chou, H.-K. Liu and S.-X. Dou, *Adv. Energy Mater.*, 2017, **7**, 1602829–1602845.
91 R. Fang, S. Zhao, Z. Sun, D. W. Wang, H. M. Cheng and F. Li, *Adv. Mater.*, 2017, **29**, 1606823–1606847.
92 A. Manthiram, S. H. Chung and C. Zu, *Adv. Mater.*, 2015, **27**, 1980–2006.
93 P. Adelhelm, P. Hartmann, C. L. Bender, M. Busche, C. Eufinger and J. Janek, *Beilstein J. Nanotechnol.*, 2015, **6**, 1016–1055.
94 X. Yu and A. Manthiram, *J. Phys. Chem. C*, 2014, **118**, 22952–22959.
95 J. Xu, J. Ma, Q. Fan, S. Guo and S. Dou, *Adv. Mater.*, 2017, **29**, 1606454–1606473.
96 L. Borchardt, M. Oschatz and S. Kaskel, *Chem.–Eur. J*, 2016, **22**, 7324–7351.
97 G. Zheng, Y. Yang, J. J. Cha, S. S. Hong and Y. Cui, *Nano Lett.*, 2011, **11**, 4462–4467.
98 K. Fu, Y. Li, M. Dirican, C. Chen, Y. Lu, J. Zhu, Y. Li, L. Cao, P. D. Bradford and X. Zhang, *Chem. Commun.*, 2014, **50**, 10277–10280.
99 Y. Wu, M. Gao, X. Li, Y. Liu and H. Pan, *J. Alloys Compd.*, 2014, **608**, 220–228.
100 L. Zeng, F. Pan, W. Li, Y. Jiang, X. Zhong and Y. Yu, *Nanoscale*, 2014, **6**, 9579–9587.
101 H. Wang, C. Zhang, Z. Chen, H. K. Liu and Z. Guo, *Carbon*, 2015, **81**, 782–787.
102 F. Wu, L. Shi, D. Mu, H. Xu and B. Wu, *Carbon*, 2015, **86**, 146–155.
103 C.-H. Chang, S.-H. Chung and A. Manthiram, *Mater. Horiz.*, 2017, **4**, 249–258.
104 D. Yang, W. Ni, J. Cheng, Z. Wang, T. Wang, Q. Guan, Y. Zhang, H. Wu, X. Li and B. Wang, *Appl. Surf. Sci.*, 2017, **413**, 209–218.
105 Y. Zhang, P. Wang, H. Tan, X. Fan and K. Huang, *J. Electrochem. Soc.*, 2018, **165**, A741–A745.
106 Y. Wang, *Int. J. Electrochem. Sci.*, 2018, **13**, 8388–8395.
107 G. Xia, L. Zhang, X. Chen, Y. Huang, D. Sun, F. Fang, Z. Guo and X. Yu, *Energy Storage Materials*, 2018, **14**, 314–323.
108 J. H. Yun, J. H. Kim, D. K. Kim and H. W. Lee, *Nano Lett.*, 2018, **18**, 475–481.
109 X.-Q. Zhang, B. He, W.-C. Li and A.-H. Lu, *Nano Res.*, 2018, **11**, 1238–1246.
110 Y. Z. Zhang, Z. Zhang, S. Liu, G. R. Li and X. P. Gao, *ACS Appl. Mater. Interfaces*, 2018, **10**, 8749–8757.
111 X. Zhao, M. Kim, Y. Liu, H.-J. Ahn, K.-W. Kim, K.-K. Cho and J.-H. Ahn, *Carbon*, 2018, **128**, 138–146.
112 J. Scholz, B. Kayaalp, A. C. Juhl, D. Clemens, M. Fröba and S. Mascotto, *ACS Energy Lett.*, 2018, **3**, 387–392.
113 Q. Pang, X. Liang, C. Y. Kwok and L. F. Nazar, *J. Electrochem. Soc.*, 2015, **162**, A2567–A2576.
114 Q. Pang, X. Liang, C. Y. Kwok and L. F. Nazar, *Nat. Energy*, 2016, **1**, 16132–16142.
115 J. Song, T. Xu, M. L. Gordin, P. Zhu, D. Lv, Y.-B. Jiang, Y. Chen, Y. Duan and D. Wang, *Adv. Funct. Mater.*, 2014, **24**, 1243–1250.

116 L. Miao, W. Wang, K. Yuan, Y. Yang and A. Wang, *Chem. Commun.*, 2014, **50**, 13231–13234.
117 M. Agostini, J.-Y. Hwang, H. M. Kim, P. Bruni, S. Brutti, F. Croce, A. Matic and Y.-K. Sun, *Adv. Energy Mater.*, 2018, **8**, 1801560–1801566.
118 J. Lee, B. Ko, J. Kang, Y. Chung, Y. Kim, W. Halim, J. H. Lee and Y. L. Joo, *Mater. Today Energy*, 2017, **6**, 255–263.
119 C. Dillard, S.-H. Chung, A. Singh, A. Manthiram and V. Kalra, *Mater. Today Energy*, 2018, **9**, 336–344.
120 S. H. Chung, K. Y. Lai and A. Manthiram, *Adv. Mater.*, 2018, **30**, 1805571–1805577.
121 Y. Hwa, J. Zhao and E. J. Cairns, *Nano Lett.*, 2015, **15**, 3479–3486.
122 F. Wu, H. Kim, A. Magasinski, J. T. Lee, H.-T. Lin and G. Yushin, *Adv. Energy Mater.*, 2014, **4**, 1400196–1400202.
123 C. Nan, Z. Lin, H. Liao, M. K. Song, Y. Li and E. J. Cairns, *J. Am. Chem. Soc.*, 2014, **136**, 4659–4663.
124 K. Cai, M. K. Song, E. J. Cairns and Y. Zhang, *Nano Lett.*, 2012, **12**, 6474–6479.
125 M. Yu, Z. Wang, Y. Wang, Y. Dong and J. Qiu, *Adv. Energy Mater.*, 2017, **7**, 1700018–1700027.
126 F. Ye, Y. Hou, M. Liu, W. Li, X. Yang, Y. Qiu, L. Zhou, H. Li, Y. Xu and Y. Zhang, *Nanoscale*, 2015, **7**, 9472–9476.
127 D. H. Lim, M. Agostini, F. Nitze, J. Manuel, J. H. Ahn and A. Matic, *Sci. Rep.*, 2017, **7**, 6327–6335.
128 X. Yu and A. Manthiram, *Phys. Chem. Chem. Phys.*, 2015, **17**, 2127–2136.
129 S. Han, X. Pu, X. Li, M. Liu, M. Li, N. Feng, S. Dou and W. Hu, *Electrochim. Acta*, 2017, **241**, 406–413.
130 W. Ren, W. Ma, S. Zhang and B. Tang, *Chem. Eng. J.*, 2018, **341**, 441–449.
131 Y. Liang, N. Deng, J. Ju, X. Zhou, J. Yan, C. Zhong, W. Kang and B. Cheng, *Electrochim. Acta*, 2018, **281**, 257–265.
132 X. Li, N. Fu, J. Zou, X. Zeng, Y. Chen, L. Zhou and H. Huang, *Mater. Lett.*, 2017, **209**, 505–508.
133 W. Zhou, C. Wang, Q. Zhang, H. D. Abruña, Y. He, J. Wang, S. X. Mao and X. Xiao, *Adv. Energy Mater.*, 2015, **5**, 1401752–1401759.
134 L. Zhou, X. Lin, T. Huang and A. Yu, *Electrochim. Acta*, 2014, **116**, 210–216.
135 J. Yang, J. Xie, X. Zhou, Y. Zou, J. Tang, S. Wang, F. Chen and L. Wang, *J. Phys. Chem. C*, 2014, **118**, 1800–1807.
136 F. Sun, J. Wang, H. Chen, W. Li, W. Qiao, D. Long and L. Ling, *ACS Appl. Mater. Interfaces*, 2013, **5**, 5630–5638.
137 C. P. Yang, Y. X. Yin, H. Ye, K. C. Jiang, J. Zhang and Y. G. Guo, *ACS Appl. Mater. Interfaces*, 2014, **6**, 8789–8795.
138 X. Li and X. Sun, *Front. Energy Res.*, 2014, **2**, 1–9.
139 J. Song, M. L. Gordin, T. Xu, S. Chen, Z. Yu, H. Sohn, J. Lu, Y. Ren, Y. Duan and D. Wang, *Angew. Chem., Int. Ed.*, 2015, **54**, 4325–4329.
140 T. Z. Hou, X. Chen, H. J. Peng, J. Q. Huang, B. Q. Li, Q. Zhang and B. Li, *Small*, 2016, **12**, 3283–3291.
141 X.-B. Cheng, J.-Q. Huang, H.-J. Peng, J.-Q. Nie, X.-Y. Liu, Q. Zhang and F. Wei, *J. Power Sources*, 2014, **253**, 263–268.
142 S. S. Zhang, *Inorg. Chem. Front.*, 2015, **2**, 1059–1069.
143 G. Zhou, E. Paek, G. S. Hwang and A. Manthiram, *Nat. Commun.*, 2015, **6**, 7760–7770.
144 B. P. Vinayan, T. Diemant, X.-M. Lin, M. A. Cambaz, U. Golla-Schindler, U. Kaiser, R. Jürgen Behm and M. Fichtner, *Adv. Mater. Interfaces*, 2016, **3**, 1600372–1600381.
145 Y. Qiu, W. Li, W. Zhao, G. Li, Y. Hou, M. Liu, L. Zhou, F. Ye, H. Li, Z. Wei, S. Yang, W. Duan, Y. Ye, J. Guo and Y. Zhang, *Nano Lett.*, 2014, **14**, 4821–4827.
146 H. Wu, Y. Huang, S. Xu, W. Zhang, K. Wang and M. Zong, *Chem. Eng. J.*, 2017, **327**, 855–867.
147 T. Gao, Z. Yu, Z.-H. Huang and Y. Yang, *ACS Appl. Energy Mater.*, 2018, **2**, 777–787.
148 S. Yao, S. Xue, S. Peng, M. Jing, X. Shen, T. Li and Z. YiLiu, *Int. J. Energy Res.*, 2019, 1–11.
149 Y. S. Su and A. Manthiram, *Nat. Commun.*, 2012, **3**, 1166–1171.
150 B. P. Williams and Y. L. Joo, *J. Electrochem. Soc.*, 2016, **163**, A2745–A2756.
151 J. Wang, Y. Yang and F. Kang, *Electrochim. Acta*, 2015, **168**, 271–276.
152 R. Singhal, S.-H. Chung, A. Manthiram and V. Kalra, *J. Mater. Chem. A*, 2015, **3**, 4530–4538.
153 Y. Cui, X. Wu, J. Wu, J. Zeng, A. P. Baker, F. Lu, X. Liang, J. Ouyang, J. Huang, X. Liu, Z. Li and X. Zhang, *Energy Storage Materials*, 2017, **9**, 1–10.
154 Y. Yang, W. Sun, J. Zhang, X. Yue, Z. Wang and K. Sun, *Electrochim. Acta*, 2016, **209**, 691–699.
155 D. K. Lee, C. W. Ahn and H.-J. Jeon, *J. Power Sources*, 2017, **360**, 559–568.
156 K. Wu, Y. Hu, Z. Shen, R. Chen, X. He, Z. Cheng and P. Pan, *J. Mater. Chem. A*, 2018, **6**, 2693–2699.
157 P. M. Shanthi, P. J. Hanumantha, T. Albuquerque, B. Gattu and P. N. Kumta, *ACS Appl. Energy Mater.*, 2018, **1**, 483–494.
158 S. Zeng, L. Li, D. Zhao, J. Liu, W. Niu, N. Wang and S. Chen, *J. Phys. Chem. C*, 2017, **121**, 2495–2503.
159 A. Freitag, M. Stamm and L. Ionov, *J. Power Sources*, 2017, **363**, 384–391.
160 P. T. Dirlam, R. S. Glass, K. Char and J. Pyun, *J. Polym. Sci., Part A: Polym. Chem.*, 2017, **55**, 1635–1668.
161 W. J. Chung, J. J. Griebel, E. T. Kim, H. Yoon, A. G. Simmonds, H. J. Ji, P. T. Dirlam, R. S. Glass, J. J. Wie, N. A. Nguyen, B. W. Guralnick, J. Park, A. Somogyi, P. Theato, M. E. Mackay, Y. E. Sung, K. Char and J. Pyun, *Nat. Chem.*, 2013, **5**, 518–524.
162 Y. Zhang, K. Li, H. Li, Y. Peng, Y. Wang, J. Wang and J. Zhao, *J. Mater. Chem. A*, 2017, **5**, 97–101.
163 K. Park, J. H. Cho, J.-H. Jang, B.-C. Yu, A. T. De La Hoz, K. M. Miller, C. J. Ellison and J. B. Goodenough, *Energy Environ. Sci.*, 2015, **8**, 2389–2395.
164 S. Matsuda, Y. Kubo, K. Uosaki and S. Nakanishi, *ACS Energy Lett.*, 2017, **2**, 924–929.
165 P. Zhu, J. Zhu, C. Yan, M. Dirican, J. Zang, H. Jia, Y. Li, Y. Kiyak, H. Tan and X. Zhang, *Adv. Mater. Interfaces*, 2018, **5**, 1701598–1701607.
166 Y. Liu, A. K. Haridas, Y. Lee, K.-K. Cho and J.-H. Ahn, *Appl. Surf. Sci.*, 2019, **471**, 135–142.
167 S. K. Simotwo and V. Kalra, *Curr. Opin. Chem. Eng.*, 2016, **13**, 150–160.

168 L. Wang, X. He, J. Li, M. Chen, J. Gao and C. Jiang, *Electrochim. Acta*, 2012, **72**, 114–119.
169 D.-H. Lim, M. Agostini, J.-H. Ahn and A. Matic, *Energy Technol.*, 2018, **6**, 1214–1219.
170 W. Zhou, Y. Yu, H. Chen, F. J. DiSalvo and H. D. Abruna, *J. Am. Chem. Soc.*, 2013, **135**, 16736–16743.
171 Q. Li, M. Liu, X. Qin, J. Wu, W. Han, G. Liang, D. Zhou, Y.-B. He, B. Li and F. Kang, *J. Mater. Chem. A*, 2016, **4**, 12973–12980.
172 X. Song, S. Wang, Y. Bao, G. Liu, W. Sun, L.-X. Ding, H. Liu and H. Wang, *J. Mater. Chem. A*, 2017, **5**, 6832–6839.
173 P. Zhu, J. Zhu, J. Zang, C. Chen, Y. Lu, M. Jiang, C. Yan, M. Dirican, R. Kalai Selvan and X. Zhang, *J. Mater. Chem. A*, 2017, **5**, 15096–15104.
174 Z. Zhou, T. Zhao, X. Lu, H. Cao, X. Zha and Z. Zhou, *J. Power Sources*, 2018, **396**, 542–550.
175 S. Huang, R. Guan, S. Wang, M. Xiao, D. Han, L. Sun and Y. Meng, *Prog. Polym. Sci.*, 2019, **89**, 19–60.
176 L. Xiao, Y. Cao, J. Xiao, B. Schwenzer, M. H. Engelhard, L. V. Saraf, Z. Nie, G. J. Exarhos and J. Liu, *Adv. Mater.*, 2012, **24**, 1176–1181.
177 M. Liu, Y. Ren, D. Zhou, H. Jiang, F. Kang and T. Zhao, *ACS Appl. Mater. Interfaces*, 2017, **9**, 2526–2534.
178 S. S. Zhang and D. T. Tran, *Electrochim. Acta*, 2013, **114**, 296–302.
179 S. Choi, J. Song, C. Wang, S. Park and G. Wang, *Chem.–Asian J.*, 2017, **12**, 1470–1474.
180 H. Li, M. Li, S. H. Siyal, M. Zhu, J.-L. Lan, G. Sui, Y. Yu, W. Zhong and X. Yang, *J. Membr. Sci.*, 2018, **555**, 169–176.
181 S. Warneke, A. Hintennach and M. R. Buchmeiser, *J. Electrochem. Soc.*, 2018, **165**, A2093–A2095.
182 Q. Li, J. Chen, L. Fan, X. Kong and Y. Lu, *Green Energy Environ.*, 2016, **1**, 18–42.
183 R. Kumar, J. Liu, J.-Y. Hwang and Y.-K. Sun, *J. Mater. Chem. A*, 2018, **6**, 11582–11605.
184 S. Zhang, K. Ueno, K. Dokko and M. Watanabe, *Adv. Energy Mater.*, 2015, **5**, 1500117–1500144.
185 C. Qu, Y. Chen, X. Yang, H. Zhang, X. Li and H. Zhang, *Nano Energy*, 2017, **39**, 262–272.
186 P. M. Shanthi, P. J. Hanumantha, B. Gattu, M. Sweeney, M. K. Datta and P. N. Kumta, *Electrochim. Acta*, 2017, **229**, 208–218.
187 T. Yim, M.-S. Park, J.-S. Yu, K. J. Kim, K. Y. Im, J.-H. Kim, G. Jeong, Y. N. Jo, S.-G. Woo, K. S. Kang, I. Lee and Y.-J. Kim, *Electrochim. Acta*, 2013, **107**, 454–460.
188 L. Hu, Y. Lu, T. Zhang, T. Huang, Y. Zhu and Y. Qian, *ACS Appl. Mater. Interfaces*, 2017, **9**, 13813–13818.
189 Y. Z. Zhang, Z. Z. Wu, G. L. Pan, S. Liu and X. P. Gao, *ACS Appl. Mater. Interfaces*, 2017, **9**, 12436–12444.
190 G. Liang, J. Wu, X. Qin, M. Liu, Q. Li, Y. B. He, J. K. Kim, B. Li and F. Kang, *ACS Appl. Mater. Interfaces*, 2016, **8**, 23105–23113.
191 X. Chen, H.-J. Peng, R. Zhang, T.-Z. Hou, J.-Q. Huang, B. Li and Q. Zhang, *ACS Energy Lett.*, 2017, **2**, 795–801.
192 Z. Li, J. Zhang and X. W. Lou, *Angew. Chem., Int. Ed.*, 2015, **54**, 12886–12890.
193 C. Shang, L. Cao, M. Yang, Z. Wang, M. Li, G. Zhou, X. Wang and Z. Lu, *Energy Storage Materials*, 2019, **18**, 375–381.
194 J. Balach, J. Linnemann, T. Jaumann and L. Giebeler, *J. Mater. Chem. A*, 2018, **6**, 23127–23168.
195 X. Liu, J. Q. Huang, Q. Zhang and L. Mai, *Adv. Mater.*, 2017, **29**, 1601759–1601783.
196 C. Li, Z. Xi, D. Guo, X. Chen and L. Yin, *Small*, 2018, **14**, 1701986–1702006.
197 Y. Zhong, K. R. Yang, W. Liu, P. He, V. Batista and H. Wang, *J. Phys. Chem. C*, 2017, **121**, 14222–14227.
198 X. Liang, C. Y. Kwok, F. Lodi-Marzano, Q. Pang, M. Cuisinier, H. Huang, C. J. Hart, D. Houtarde, K. Kaup, H. Sommer, T. Brezesinski, J. Janek and L. F. Nazar, *Adv. Energy Mater.*, 2016, **6**, 1501636–1501645.
199 M. Liu, Q. Li, X. Qin, G. Liang, W. Han, D. Zhou, Y. B. He, B. Li and F. Kang, *Small*, 2017, **13**, 1602539–1602545.
200 J. Zhu, R. Pitcheri, T. Kang, Y. Guo, J. Li and Y. Qiu, *Ceram. Int.*, 2018, **44**, 16837–16843.
201 Z. Liu, B. Liu, P. Guo, X. Shang, M. Lv, D. Liu and D. He, *Electrochim. Acta*, 2018, **269**, 180–187.
202 C. Guo, H. Yang, A. Naveed, Y. Nuli, J. Yang, Y. Cao, H. Yang and J. Wang, *Chem. Commun.*, 2018, **54**, 8347–8350.
203 C.-L. Lee, C. Kim and I.-D. Kim, *RSC Adv.*, 2017, **7**, 44804–44808.
204 X. Song, T. Gao, S. Wang, Y. Bao, G. Chen, L.-X. Ding and H. Wang, *J. Power Sources*, 2017, **356**, 172–180.
205 Q. Zhang, Y. Wang, Z. W. Seh, Z. Fu, R. Zhang and Y. Cui, *Nano Lett.*, 2015, **15**, 3780–3786.
206 Y. Zhang, S. Yao, R. Zhuang, K. Luan, X. Qian, J. Xiang, X. Shen, T. Li, K. Xiao and S. Qin, *J. Alloys Compd.*, 2017, **729**, 1136–1144.
207 H. Wei, E. F. Rodriguez, A. S. Best, A. F. Hollenkamp, D. Chen and R. A. Caruso, *Adv. Energy Mater.*, 2016, 1601616–1601625.
208 S. Mei, C. J. Jafta, I. Lauermann, Q. Ran, M. Kärgell, M. Ballauff and Y. Lu, *Adv. Funct. Mater.*, 2017, **27**, 1701176–1701185.
209 Z. Yang, Z. Zhu, J. Ma, D. Xiao, X. Kui, Y. Yao, R. Yu, X. Wei, L. Gu, Y.-S. Hu, H. Li and X. Zhang, *Adv. Energy Mater.*, 2016, **6**, 1600806.
210 X. Tao, J. Wang, Z. Ying, Q. Cai, G. Zheng, Y. Gan, H. Huang, Y. Xia, C. Liang, W. Zhang and Y. Cui, *Nano Lett.*, 2014, **14**, 5288–5294.
211 B. Xu, H. Y. Sohn, Y. Mohassab and Y. Lan, *RSC Adv.*, 2016, **6**, 79706–79722.
212 H. Tang, S. Yao, S. Xue, M. Liu, L. Chen, M. Jing, X. Shen, T. Li, K. Xiao and S. Qin, *Electrochim. Acta*, 2018, **263**, 158–167.
213 T.-T.-N. Nguyen and J.-L. He, *Adv. Powder Technol.*, 2016, **27**, 1868–1873.
214 D. Liu, C. Zhang, G. Zhou, W. Lv, G. Ling, L. Zhi and Q. H. Yang, *Adv. Sci.*, 2018, **5**, 1700270–1700281.
215 C. Dillard, S.-H. Chung, A. Singh, A. Manthiram and V. Kalra, *Mater. Today Energy*, 2018, **9**, 336–344.

216 G. Zhou, H. Tian, Y. Jin, X. Tao, B. Liu, R. Zhang, Z. W. Seh, D. Zhuo, Y. Liu, J. Sun, J. Zhao, C. Zu, D. S. Wu, Q. Zhang and Y. Cui, *Proc. Natl. Acad. Sci. U. S. A.*, 2017, **114**, 840–845.
217 Y. Yao, W. Feng, M. Chen, X. Zhong, X. Wu, H. Zhang and Y. Yu, *Small*, 2018, **14**, 1802516–1802524.
218 Z. Hao, L. Yuan, C. Chen, J. Xiang, Y. Li, Z. Huang, P. Hu and Y. Huang, *J. Mater. Chem. A*, 2016, **4**, 17711–17717.
219 J. Deng, J. Guo, J. Li, M. Zeng and D. Gong, *Ceram. Int.*, 2018, **44**, 17340–17344.
220 B. Cao, Y. Chen, D. Li, L. Yin and Y. Mo, *ChemSusChem*, 2016, **9**, 3338–3344.
221 L. Ma, H. Yuan, W. Zhang, G. Zhu, Y. Wang, Y. Hu, P. Zhao, R. Chen, T. Chen, J. Liu, Z. Hu and Z. Jin, *Nano Lett.*, 2017, **17**, 7839–7846.
222 Z. Yuan, H. J. Peng, T. Z. Hou, J. Q. Huang, C. M. Chen, D. W. Wang, X. B. Cheng, F. Wei and Q. Zhang, *Nano Lett.*, 2016, **16**, 519–527.
223 N. Deng, W. Kang, Y. Liu, J. Ju, D. Wu, L. Li, B. S. Hassan and B. Cheng, *J. Power Sources*, 2016, **331**, 132–155.
224 Y. Xiang, J. Li, J. Lei, D. Liu, Z. Xie, D. Qu, K. Li, T. Deng and H. Tang, *ChemSusChem*, 2016, **9**, 3023–3039.
225 G. Chen, X. Song, S. Wang, Y. Wang, T. Gao, L.-X. Ding and H. Wang, *J. Membr. Sci.*, 2018, **548**, 247–253.
226 M. S. Kim, L. Ma, S. Choudhury and L. A. Archer, *Adv. Mater. Interfaces*, 2016, **3**, 1600450–1600457.
227 D. Kumar, S. K. Rajouria, S. B. Kuhar and D. K. Kanchan, *Solid State Ionics*, 2017, **312**, 8–16.
228 K. B. Hueso, V. Palomares, M. Armand and T. Rojo, *Nano Res.*, 2017, **10**, 4082–4114.
229 S. Wenzel, H. Metelmann, C. Raiß, A. K. Dürr, J. Janek and P. Adelhelm, *J. Power Sources*, 2013, **243**, 758–765.
230 S. Xin, Y. X. Yin, Y. G. Guo and L. J. Wan, *Adv. Mater.*, 2014, **26**, 1261–1265.
231 A. Manthiram and X. Yu, *Small*, 2015, **11**, 2108–2114.
232 D. Kumar, S. B. Kuhar and D. K. Kanchan, *J. Energy Storage*, 2018, **18**, 133–148.
233 S. Wei, S. Xu, A. Agrawral, S. Choudhury, Y. Lu, Z. Tu, L. Ma and L. A. Archer, *Nat. Commun.*, 2016, **7**, 11722–11731.
234 J. Wang, J. Yang, Y. Nuli and R. Holze, *Electrochem. Commun.*, 2007, **9**, 31–34.
235 T. H. Hwang, D. S. Jung, J. S. Kim, B. G. Kim and J. W. Choi, *Nano Lett.*, 2013, **13**, 4532–4538.
236 H. Ryu, T. Kim, K. Kim, J.-H. Ahn, T. Nam, G. Wang and H.-J. Ahn, *J. Power Sources*, 2011, **196**, 5186–5190.
237 X. Yu and A. Manthiram, *J. Phys. Chem. Lett.*, 2014, **5**, 1943–1947.
238 I. Bauer, M. Kohl, H. Althues and S. Kaskel, *Chem. Commun.*, 2014, **50**, 3208–3210.
239 X. Yu and A. Manthiram, *Chem.–Eur. J*, 2015, **21**, 4233–4237.
240 Y. Hao, X. Li, X. Sun and C. Wang, *ChemistrySelect*, 2017, **2**, 9425–9432.
241 W. Du, Q. Xu, R. Zhan, Y. Zhang, Y. Luo and M. Xu, *Mater. Lett.*, 2018, **221**, 66–69.
242 H. Wang, C. Wang, E. Matios and W. Li, *Angew. Chem., Int. Ed. Engl.*, 2018, **57**, 7734–7737.
243 X. Yu and A. Manthiram, *Adv. Energy Mater.*, 2015, **5**, 1500350–1500355.
244 I. Kim, C. H. Kim, S. h. Choi, J.-P. Ahn, J.-H. Ahn, K.-W. Kim, E. J. Cairns and H.-J. Ahn, *J. Power Sources*, 2016, **307**, 31–37.
245 X. Yu and A. Manthiram, *Chem. Mater.*, 2016, **28**, 896–905.
246 Q. Lu, X. Wang, J. Cao, C. Chen, K. Chen, Z. Zhao, Z. Niu and J. Chen, *Energy Storage Materials*, 2017, **8**, 77–84.
247 D. Ma, Y. Li, J. Yang, H. Mi, S. Luo, L. Deng, C. Yan, M. Rauf, P. Zhang, X. Sun, X. Ren, J. Li and H. Zhang, *Adv. Funct. Mater.*, 2018, **28**, 1705537–1705545.
248 K. Xie, Y. You, K. Yuan, W. Lu, K. Zhang, F. Xu, M. Ye, S. Ke, C. Shen, X. Zeng, X. Fan and B. Wei, *Adv. Mater.*, 2016, **29**, 1604724–1604729.
249 Y. Wei, Y. Tao, Z. Kong, L. Liu, J. Wang, W. Qiao, L. Ling and D. Long, *Energy Storage Materials*, 2016, **5**, 171–179.
250 Z. Li, J. Zhang, H. B. Wu and X. W. D. Lou, *Adv. Energy Mater.*, 2017, **7**, 1700281–1700287.
251 X. Li, J. Liang, K. Zhang, Z. Hou, W. Zhang, Y. Zhu and Y. Qian, *Energy Environ. Sci.*, 2015, **8**, 3181–3186.
252 Y. Yao, L. Zeng, S. Hu, Y. Jiang, B. Yuan and Y. Yu, *Small*, 2017, **13**, 1603513–1603520.
253 B. Kalimuthu and K. Nallathamby, *ACS Appl. Mater. Interfaces*, 2017, **9**, 26756–26770.
254 X. Zhao, L. Yin, T. Zhang, M. Zhang, Z. Fang, C. Wang, Y. Wei, G. Chen, D. Zhang, Z. Sun and F. Li, *Nano Energy*, 2018, **49**, 137–146.
255 J. Zhou, J. Yang, Z. Xu, T. Zhang, Z. Chen and J. Wang, *J. Mater. Chem. A*, 2017, **5**, 9350–9357.
256 Y. J. Hong, K. C. Roh and Y. Chan Kang, *J. Mater. Chem. A*, 2018, **6**, 4152–4160.
257 K. Balakumar and N. Kalaiselvi, *Carbon*, 2017, **112**, 79–90.
258 J. Ding, H. Zhou, H. Zhang, L. Tong and D. Mitlin, *Adv. Energy Mater.*, 2018, **8**, 1701918–1701927.
259 R. Mukkabla, S. Deshagani, P. Meduri, M. Deepa and P. Ghosal, *ACS Energy Lett.*, 2017, **2**, 1288–1295.
260 J. He, W. Lv, Y. Chen, J. Xiong, K. Wen, C. Xu, W. Zhang, Y. Li, W. Qin and W. He, *J. Power Sources*, 2017, **363**, 103–109.
261 M. Jia, S. Lu, Y. Chen, T. Liu, J. Han, B. Shen, X. Wu, S.-J. Bao, J. Jiang and M. Xu, *J. Power Sources*, 2017, **367**, 17–23.
262 L. Zeng, X. Wei, J. Wang, Y. Jiang, W. Li and Y. Yu, *J. Power Sources*, 2015, **281**, 461–469.
263 L. Zeng, X. Chen, R. Liu, L. Lin, C. Zheng, L. Xu, F. Luo, Q. Qian, Q. Chen and M. Wei, *J. Mater. Chem. A*, 2017, **5**, 22997–23005.
264 S.-K. Park, J.-S. Park and Y. C. Kang, *J. Mater. Chem. A*, 2018, **6**, 1028–1036.
265 L. Zeng, Y. Yao, J. Shi, Y. Jiang, W. Li, L. Gu and Y. Yu, *Energy Storage Materials*, 2016, **5**, 50–57.

